Viscous and Diffusive Effects in Magnetoplasmadynamic Flows

by

Scott Alan Miller

S.B. Aeronautics and Astronautics, Massachusetts Institute of Technology, 1988

SUBMITTED IN PARTIAL FULFILLMENT OF THE
REQUIREMENTS FOR THE DEGREE OF

Master of Science
in
Aeronautics and Astronautics
at the
Massachusetts Institute of Technology

June 1990

Signature of Author _____
Department of Aeronautics and Astronautics
June 1990

Certified by _____
Professor Manuel Martinez-Sanchez, Thesis Supervisor
Department of Aeronautics and Astronautics

Accepted by _____
Professor Harold Y. Wachman, Chairman
Department Graduate Committee

Viscous and Diffusive Effects in Magnetoplasmadynamic Flows

by

Scott Alan Miller

Submitted to the Department of
Aeronautics and Astronautics
in partial fulfillment of the
requirements for the degree of
Master of Science in Aeronautics and Astronautics

Recent work has shown that viscous and diffusive processes have a significant effect on MPD thruster performance for some geometries. In particular, viscosity has been shown to drastically reduce the flow exit velocity through shear forces and the establishment of a strong adverse pressure gradient by excessive heating of the heavy species. This research has developed a two-dimensional, two fluid model which offers a consistent treatment of the effects of viscosity and diffusion through a modified Navier-Stokes formulation of the governing equations. Also included in the model are the effects of ambipolar diffusion, ionizational nonequilibrium, and collisional energy transfer between electrons and heavy species. The system of equations is solved numerically by Time-Split MacCormack's Method, which is an explicit, two step predictor-corrector algorithm accurate to second order in both time and space. In order to obtain an initial understanding of the physical processes involved, solutions are achieved with a frozen magnetic field based on results from previous quasi one-dimensional studies, a condition which will later be relaxed. Results for the baseline case indicated that the flow was rapidly accelerated to supersonic velocities through a thin region at the inlet, where the fluid density in particular decreased dramatically. The development of velocity, thermal, and diffusive boundary layers was examined throughout the channel, and it was found that the flow became fully developed by half the channel length. Viscosity and collisional energy transfer caused the heavy species temperature to increase to the order of the electron temperature by the end of the channel, a phenomenon which has been observed in experiments. In addition to examining the flow variables, the magnitudes of the terms in the governing equations were compared to identify the dominant effects in different regions of the channel. An estimate of the total power loss to the electrodes due to heat conduction and ambipolar diffusion was produced, and the flow results were compared to those obtained from previous one-dimensional work.

Thesis Supervisor: Manuel Martinez-Sanchez

Title: Associate Professor of Aeronautics and Astronautics

Acknowledgements

I would first like to thank my advisor, Professor Martinez-Sanchez, for his direction and guidance over the course of this project. Eli Niewood deserves the largest proportion of my appreciation, for his help drawn from experience in numerical simulations, word processing, and the physics of MPD flows. I would also like to thank Eric Sheppard, Jean-Marc Chanty, and Jeff Preble, the other members of our research group, for their input and advice. This thesis is dedicated to my parents, in appreciation for their continued support over the past eighteen years of my education. The material herein is based upon work supported under a National Science Foundation Graduate Fellowship. Any opinions, findings, conclusions, or recommendations expressed in this publication are those of the author and do not necessarily reflect the views of the National Science Foundation.

Contents

List of Figures

List of Tables

List of Symbols

a	Speed of sound
A	Channel area
α	Ionization fraction
B	Magnetic field strength
B_o	Inlet magnetic field strength
β	Hall parameter
$\bar{c}_s$	Average thermal velocity of species s
c_p	Specific heat at constant pressure
c_v	Specific heat at constant volume
D	Channel width
D_a	Ambipolar diffusion coefficient
$\triangle t$	Time step
$\triangle x$	Spatial step in axial direction
$\triangle y$	Spatial step in transverse direction
e	Electric charge of a proton
e_s	Internal energy of species s
e	Subscript denoting electron species
E	Electric field strength
E_s	Total energy of species s
E_i	Ionization energy
E_l	Elastic collisional energy transfer between electrons and heavy species
ϵ_o	Permittivity of vacuum
f_s	Distribution function of species s
$\vec{F}_s$	External force p.u. volume applied on species s
g	Subscript denoting heavy species
γ	Ratio of specific heats
h	Planck's constant

H Channel height

H_s Enthalpy of species s

i Subscript denoting ion species

I Total electric current

Isp Specific impulse

j Electric current density

j_s Electric current density due to species s

k_s Thermal conductivity of species s

k Boltzmann's constant

L Channel length

λ_s Mean free path for a single component gas of species s

Λ Spitzer logarithm operand

M Mach number

m_a Argon atomic mass

m_e Electron mass

m_{rs} Reduced mass of species r and s

μ Fluid viscosity

μ_s Viscosity of species s

μ_o Permeability of vacuum

n Subscript denoting neutral species

n_s Number density of species s

$\dot{n}_e^{HH}$ Hinnov-Hirschberg ionization-recombination rate

ν_{rs} Collision frequency of species r with species s

p Scalar fluid pressure

p_s Scalar pressure due to species s

p^T Sum of fluid and magnetic pressures

$\overline{\overline{p}}_s$ Kinetic pressure dyad for species s

Pr Prandtl number

Φ Viscous dissipation function

R_s Gas constant of species s

ρ Fluid density

ρ_s Mass density of species s

Q_{rs} Collision cross section of species r with species s

S_σ	Sonine coefficient for electrical conductivity
S_k	Sonine coefficient for thermal conductivity
σ	Scalar electrical conductivity
t	Time
T_s	Temperature of species s
$\vec{u}_s$	Vector mean velocity of species s
u_s	Axial velocity of species s
u	Axial average fluid velocity
$\vec{v}$	Velocity vector
v_s	Transverse velocity of species s
v	Transverse average fluid velocity
v_B	Ion Bohm velocity
$\vec{V}_i$	Ion slip velocity
$\vec{x}$	Position vector
x	Subscript denoting the axial component of a vector
y	Subscript denoting the transverse component of a vector
$<>$	Average value of a quantity

Chapter 1
Introduction

1.1 Electric Propulsion

Nearly all space propulsion needs are currently filled by chemical propulsion systems, which are limited in performance by the energy stored within the propellants used. One way to overcome this limitation is to increase the propellant exit velocity through additional energy supplied from an external source. Basic electric propulsion devices, such as the electrothermal resistojet and low power arcjet, use electric power from an outside source to impart additional thermal energy to the flow, thereby increasing the exit velocity through gasdynamic forces. More advanced methods of electric propulsion heat the propellant to an ionized state, and then accelerate it through applied or induced electromagnetic forces. High efficiencies and specific impulses of more than 1000 seconds can be achieved in this manner, at the cost of the added weight of power generating and conditioning systems. The low thrust generated by these devices, however, restricts their employment to space applications only, such as satellite stationkeeping, orbital maneuvering, and interplanetary missions. At present, resistojets, arcjets, and ion engines have been manufactured and utilized in space, while more exotic methods such as electromagnetic and laser propulsion are still primarily in the research and development phase.

1.2 Magnetoplasmadynamic Thrusters

The magnetoplasmadynamic, or MPD thruster, is one type of electromagnetic accelerator which is currently being researched for space applications. These thrusters have been operated in both a steady and pulsed mode, with applied or self-induced magnetic fields. In the steady, self-induced configuration modeled in this research, an electric current is applied between two electrodes across the thruster channel which ionizes the injected

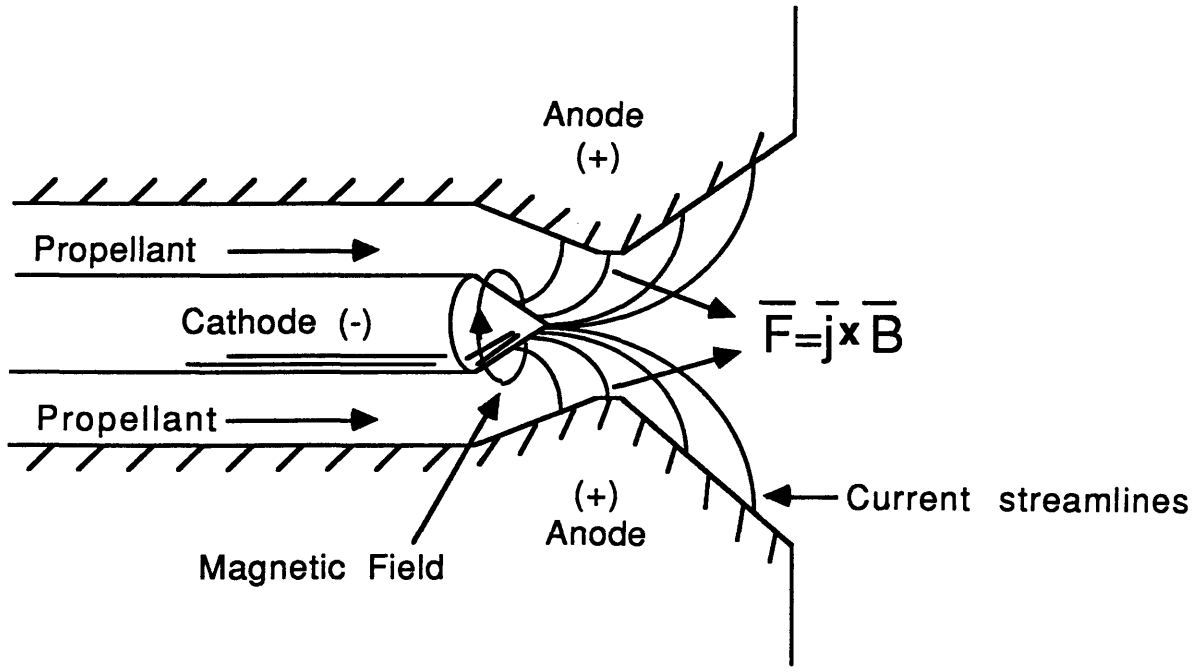

Figure 1.1: Simplified MPD Thruster Diagram

propellant through Joule (or Ohmic) heating. This current also induces a perpendicular magnetic field component through Maxwell's magnetic field curl relation, which in turn accelerates the ionized gas by the Lorentz force $\vec{F} = \vec{j} \times \vec{B}$. Figure 1.1 shows a basic axisymmetric MPD thruster with a central cathode and surrounding anode. The total Lorentz force on the propellant is seen to be a combination of an axial, or "blowing", force and a radial "pumping" force. The "blowing" force is produced by the interaction of the radial current flowing between the electrodes and the magnetic field, and contributes to the thrust of the device. The "pumping" force arises from the interaction between the magnetic field and the axial current generated by $\vec{E} \times \vec{B}$ drift of the charged species, otherwise known as the Hall Effect. This radial force works to concentrate the plasma along the centerline of the thruster and contributes no thrust, thereby reducing efficiency and in extreme cases creating an anode which is severely depleted of charge carriers.

The net thrust of the device is produced by a combination of gasdynamic pressure forces resulting from the thermal energy imparted to the propellant and electromagnetic forces due to the Lorentz effect. At high efficiencies the electromagnetic contribution dominates, generating 85-90% of the total thrust. A typical coaxially configured self-field MPD thruster is shown in Figure 1.2. This diagram illustrates the current path in greater detail, and in particular highlights the dominance of the Hall Effect, which causes the

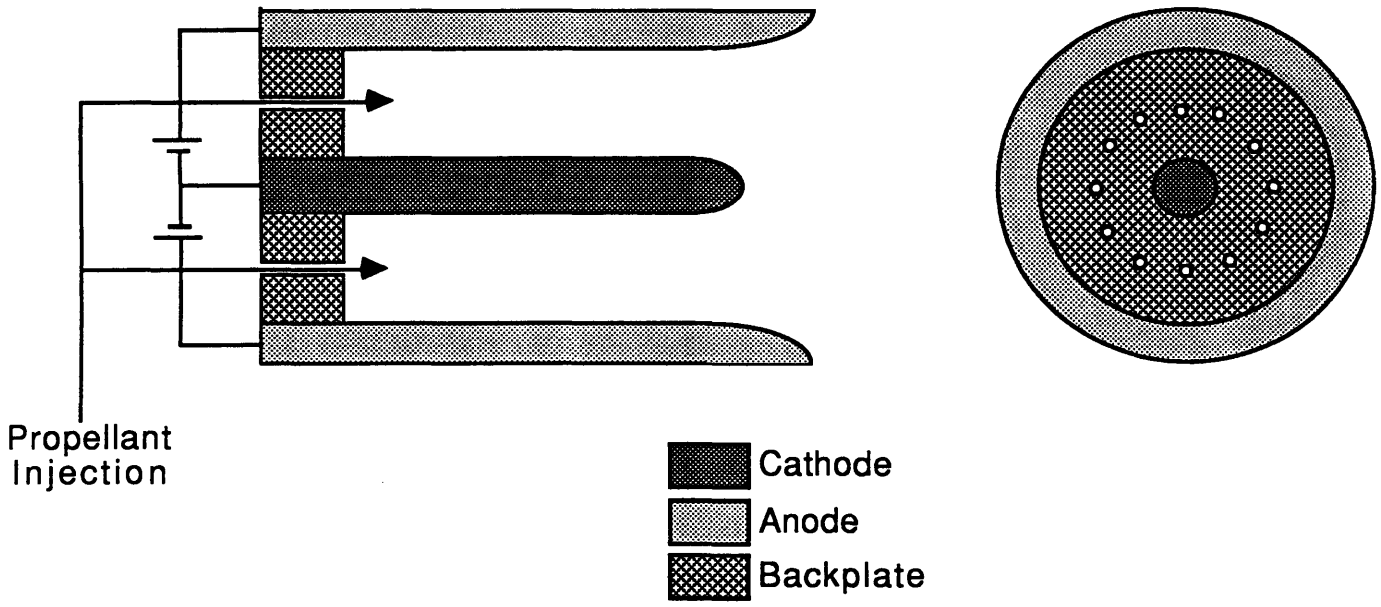

Figure 1.2: Typical Self-Field Coaxial MPD Thruster Design

$SpecificImpulse = 1000 - 5000sec$	$InputPower = 0.1 - 10MW$
$Efficiency = 30 - 50\%$	$ElectricCurrent = 10 - 100kA$
$Thrust = 20 - 200N$	$MagneticField = 0.05 - 0.3T$
$MassFlowRate = 1 - 10g/s$	

Table 1.1: Typical Self-Field MPD Thruster Parameters

current to be concentrated at the root of the cathode and at the tip of the anode.

MPD thruster electrodes are generally constructed of high temperature metals, while insulators such as boron nitride are used for the backplate. A wide range of propellants may be utilized in the device, including Hydrogen, Oxygen, Nitrogen, Ammonia, or any of the Noble gases, although Argon is the current propellant of choice. Steady-state MPD thrusters have several advantages over other methods of propulsion, including simple design, low system specific mass, high specific impulse, and high thrust density (compared to other high Isp electric propulsion devices). Disadvantages of MPD propulsion systems include high power requirements, lifetime limitations due to electrode erosion, and the existence of an "onset" phenomenon at the high current levels necessary for high efficiency operation. Thruster operation beyond this onset condition has been observed to result in severe instabilities and dramatic increases in electrode erosion rates. Table 1.1 lists the ranges of several notable parameters for a typical self-field MPD accelerator.

1.3 Status of MPD Thruster Research

Much experimental work has been done on MPD thrusters since the 1960's, most recently at Princeton by Kelly and Jahn[7,26], at the Jet Propulsion Laboratory by King[15], and at the Institute of Space and Astronautical Science in Tokyo by Kunii, Kuriki, and Toki[16,17,37,40]. A great deal has been learned from these experiments with respect to thruster design and scaling, performance enhancement, electrode erosion rates, and the physical state of the accelerating plasma. The high power and high diffusion pumping rates required and the difficulty in obtaining diagnostic measurements, however, has led to increased theoretical and numerical modeling of MPD thrusters not only as a method of research, but also as a diagnostic tool. Unfortunately, the complex nature of the plasma environment as well as the collisional and electromagnetic effects which occur in the MPD thruster, make it extremely difficult to analyze.

Thus far numerical work has been limited to simplified cases. One-dimensional, one fluid, fully ionized magnetoplasmadynamic flow has been examined extensively by Martinez-Sanchez[24]. Two-dimensional codes with similarly simplified physics have been developed by Martinez-Sanchez and Heimerdinger[23], Chanty[5], Park[29], and Auweter-Kurtz[2]. These models neglect diffusive and viscous effects, collisional transfer processes, and thermal and ionizational nonequilibrium effects. Subramanian and Lawless[36] have examined the effects of nonequilibrium ionization in one dimension, especially in relation to the phenomena of onset. Heimerdinger[8] has constructed a model which includes the effects of heat conduction, ionization, and radiation in an approximate sense in a quasi-2D numerical model with various physical and geometrical simplifications.

The first comprehensive quasi one-dimensional model of an MPD thruster which accounts for all of the above physical processes and employs a two-fluid formulation, was developed recently by Niewood[27]. This model compares favorably with earlier one fluid, one-dimensional work, and can demonstrate the effects of varying the total applied current and the thruster channel area. It was found that thermal and ionizational equilibrium are not good modeling assumptions in the MPD regime, and that viscous and diffusive processes have a significant effect on MPD thruster performance for some geometries. In particular, with respect to the long narrow channel studied by Niewood, it was found that viscosity drastically reduced the flow exit velocity through excessive heating of the propellant gas and the establishment of a strong adverse pressure gradient. For long

channels this resulted in a thermally choked condition at the exit which constrained the Mach number to unity.

Although the viscous and diffusive effects in the model of Niewood were formulated assuming parabolic distributions and fully-developed flow throughout the thruster channel, one result was particularly interesting and potentially very important. This was the fact that viscous heating of the heavy species caused the gas temperature to increase to a level equal to or greater than the electron temperature at the exit. Excessive heavy species temperatures have been observed in experiments, but as yet no definitive argument has been presented to explain the underlying physical processes of this phenomenon. To illustrate the magnitude of this effect, the results of three MPD experiments are briefly described here. In all three cases, Doppler line broadening techniques were used to determine heavy species temperatures. DiCapua and Jahn in 1971 examined energy deposition in parallel plate plasma accelerators, and found ion temperatures between 2.5 and 8.5 eV[6]. In 1985 Kunii and Kuriki measured ion temperatures of 6.2 eV at the exit plane of a quadrupole MPD arcjet[16]. Finally, in 1988 Kilfoyle et.al. [13] performed a spectroscopic analysis of the exit plane of a flared coaxial MPD thruster, and found heavy species temperatures of 1-7 eV for Argon and 2.6-3.4 eV for hydrogen, compared to an electron temperature of approximately 1.1 eV. Possible mechanisms for gas heating include the already-mentioned viscous effects, electron-heavy species collisional energy transfer, ion-neutral velocity slip, shocks, ion-acoustic waves, and plasma instabilities. Niewood studied viscous, collisional, and velocity slip effects and found that viscous dissipation was the primary contributor in raising the gas temperature to 1.5 eV and above, depending on the channel geometry and total applied current. This result warranted further work on the effects of viscous and diffusive processes in MPD flows, and as such was one of the primary reasons for undertaking the research presented in this thesis.

There were two goals of this research. The first was to develop a two-dimensional MPD flow model with detailed modeling of physical processes, including viscous and diffusive effects, in an effort to extend the numerical work completed thus far. The second was to use the model to examine the effects of viscosity and diffusion on thruster performance, to include verifying and quantifying the viscous heating phenomenon described above, studying the development of viscous and diffusive boundary layers in the channel, and calculating an estimate of energy losses due to gradients at the electrode walls.

1.4 Overview of This Research

This research provides the next step toward achieving an accurate numerical model of MPD thrusters. Careful treatment of viscous, diffusive, and other physical processes in two dimensions for a simple geometry is undertaken in order to better understand these truly multidimensional effects. The model developed in this research treats electrons and heavy species separately. Only first ionization is considered, and the resulting plasma is assumed to be macroscopically neutral with strong coupling between ions and neutral atoms. Terms representing a Navier-Stokes formulation of gas viscosity, heat conduction, and ambipolar diffusion are retained in the governing equations. Source terms which model ionization and recombination rates, Lorentz forces, Joule heating, and collisional energy transfer between electrons and heavy species are also incorporated. The resulting system of equations essentially represents an expanded and modified Navier-Stokes formulation of the problem. At this time the magnetic field is taken from a quasi one-dimensional calculation by Niewood[27], in order to simplify the numerical solution process and also to gain an initial understanding of the viscous and diffusive terms without introducing asymmetries due to the Hall Effect. As a result, the magnetic field is constrained to vary in the axial direction only and can be thought of as externally applied. This simplification is currently being relaxed in order to obtain fully two-dimensional, self-consistent results. Time-Split MacCormack's Method has been utilized on a non-uniform computational grid to numerically solve the governing equations for a constant area channel. The implementation and results of this effort are described within the remainder of this document.

The formulation of the analytical model is discussed in Chapter 2 of this thesis, followed by a description of the numerical method in Chapter 3. Chapter 4 discusses in detail the results of the simulation, while Chapters 5 and 6 contain conclusions and recommendations for further work. Unless otherwise stated, all quantities are reported in MKS units.

Chapter 2
Governing Equations

2.1 Basic Equations

The equations governing magnetoplasmadynamic flow in a channel are Maxwell's Equations, the electron, ion, and neutral species conservation equations, and the equation of state.

2.1.1 Maxwell's Equations

Maxwell's equations can be written in vector form as

$$\nabla \times \vec{E} = -\frac{\partial \vec{B}}{\partial t} \tag{2.1}$$

$$\nabla \times \vec{B} = \mu_0 \left(\vec{j} + \epsilon_0 \frac{\partial \vec{E}}{\partial t} \right) \tag{2.2}$$

$$\nabla \cdot \vec{E} = \frac{e(n_i - n_e)}{\epsilon_0} \tag{2.3}$$

$$\nabla \cdot \vec{B} = 0 \tag{2.4}$$

2.1.2 Species Conservation Equations

The species conservation equations can be derived from Boltzmann's Equation, which describes the rate of change of the distribution function of a species s with respect to time and position in six-dimensional phase space ($d^3r d^3v$). Boltzmann's Equation can be

written in vector form as in Bittencourt[4]:

$$\frac{\partial f_s}{\partial t} + \vec{v} \cdot \nabla f_s + \frac{\vec{F}_s}{m_s} \cdot \nabla_v f_s = \left(\frac{\partial f_s}{\partial t}\right)_{coll} \tag{2.5}$$

where $\vec{F}_s$ is an externally applied force vector and the term on the right-hand side indicates the net time rate of change of the distribution function of species s due to collisions.

The first step in deriving the species conservation equations is to multiply Equation 2.5 by some function $\phi(\vec{x}, \vec{v}, t)$, which may vary with respect to position, velocity, and time. Integrating over all phase space, we obtain the general transport equation

$$\frac{\partial}{\partial t}\left(n_s < \phi >_s\right) - n_s < \frac{\partial \phi}{\partial t} >_s + \nabla \cdot \left(n_s < \phi \vec{v} >_s\right) - n_s < \vec{v} \cdot \nabla \phi >_s$$

$$- n_s < \frac{F_s}{m_s} \cdot \nabla_v \phi >_s = \int \phi \left(\frac{\partial f_s}{\partial t}\right)_{coll} d^3v \tag{2.6}$$

where the definition of the average value of a quantity ($<\ >$) has been utilized. By now substituting appropriate values for the function ϕ, we can arrive at the three species conservation equations, which are closed by Maxwell's equations and the equation of state:

$$p = \sum_s n_s k T_s = \sum_s \rho_s R_s T_s \tag{2.7}$$

Taking $\phi = m_s$ in Equation 2.6 results in the species continuity equation, which is a statement of the conservation of mass of species s.

$$\frac{\partial \rho_s}{\partial t} + \nabla \cdot (\rho_s \vec{u}_s) = S_s = m_s \int \left(\frac{\partial f_s}{\partial t}\right)_{coll} d^3v \tag{2.8}$$

Here the source term on the right-hand side of the equation, S_s, represents the rate per unit volume that particles of species s are created or destroyed as a result of collisional events, such as ionization or recombination.

Using $\phi = m_s \vec{v}$, we obtain the species momentum equation

$$\rho_s \left[\frac{\partial \vec{u}_s}{\partial t} + (\vec{u}_s \cdot \nabla)\vec{u}_s\right] + \nabla \cdot \overline{\overline{p}}_s - n_s < \vec{F} >_s = \vec{A}_s - \vec{u}_s S_s \tag{2.9}$$

The quantity $\overline{\overline{p}}_s$ is the kinetic pressure dyad, representing the scalar pressure and tangential shear forces. The source term $\vec{A}_s$ denotes the collisional rate of change of mean momentum for species s, while the term S_s is the same as that employed in Equation 2.8.

Since we are concerned with the effect of the Lorentz force in this research, we may substitute

$$< \vec{F} >_s = q_s \left(\vec{E} + \vec{u}_s \times \vec{B} \right) \tag{2.10}$$

In addition, the collisional momentum term may be written as

$$\vec{A}_s = \rho_s \sum_s \nu_{sr} \left(\vec{u}_s - \vec{u}_r \right) \qquad (s \neq r) \tag{2.11}$$

This leads to the statement of species momentum conservation in the following form:

$$\rho_s \left[\frac{\partial \vec{u}_s}{\partial t} + (\vec{u}_s \cdot \nabla)\vec{u}_s \right] + \nabla \cdot \overline{\overline{p}}_s = n_s q_s \left(\vec{E} + \vec{u}_s \times \vec{B} \right) + \rho_s \sum_s \nu_{sr} \left(\vec{u}_s - \vec{u}_r \right) - \vec{u}_s S_s \tag{2.12}$$

Finally, the species energy equation may be obtained by substituting $\phi = \frac{1}{2} m_s v^2$ in the general transport equation. Again after some manipulation we arrive at the following form:

$$\frac{D_s}{D_s t} \left(\frac{3}{2} p_s \right) + \left(\frac{3}{2} p_s \right) \nabla \cdot \vec{u}_s + \frac{\partial}{\partial t} \left(\frac{1}{2} \rho_s u_s^2 \right) + \nabla \cdot \left(\frac{1}{2} \rho_s u_s^2 \vec{u}_s \right) + \nabla \cdot \left(\overline{\overline{p}}_s \cdot \vec{u}_s \right)$$

$$+ \nabla \cdot \vec{q}_s - n_s < \vec{F} \cdot \vec{v} >_s = M_s \tag{2.13}$$

where $\frac{D_s}{D_s t}$ is the substantial derivative for species s, $\vec{q}_s = -k_s \nabla T_s$ is the heat flux vector, and M_s represents the rate of change of energy per unit volume due to collisions, given by

$$M_s = \frac{1}{2} m_s \int v^2 \left(\frac{\partial f_s}{\partial t} \right)_{coll} d^3 v \tag{2.14}$$

Substituting for the electromagnetic forces and heat flux vector and rearranging, we obtain

$$\frac{D_s}{D_s t} \left(\frac{3}{2} p_s \right) + \left(\frac{3}{2} p_s \right) \nabla \cdot \vec{u}_s + \frac{\partial}{\partial t} \left(\frac{1}{2} \rho_s u_s^2 \right) + \nabla \cdot \left(\frac{1}{2} \rho_s u_s^2 \vec{u}_s \right) + \nabla \cdot \left(\overline{\overline{p}}_s \cdot \vec{u}_s \right)$$

$$- \nabla \cdot (k_s \nabla T_s) = \vec{j}_s \cdot \vec{E} + M_s \tag{2.15}$$

2.2 Two-Dimensional MPD Channel Flow Model

Using the equations in Section 2.1 for the case of two-dimensional flow of a three-component (electron, ion, neutral) plasma, a model of magnetoplasmadynamic channel

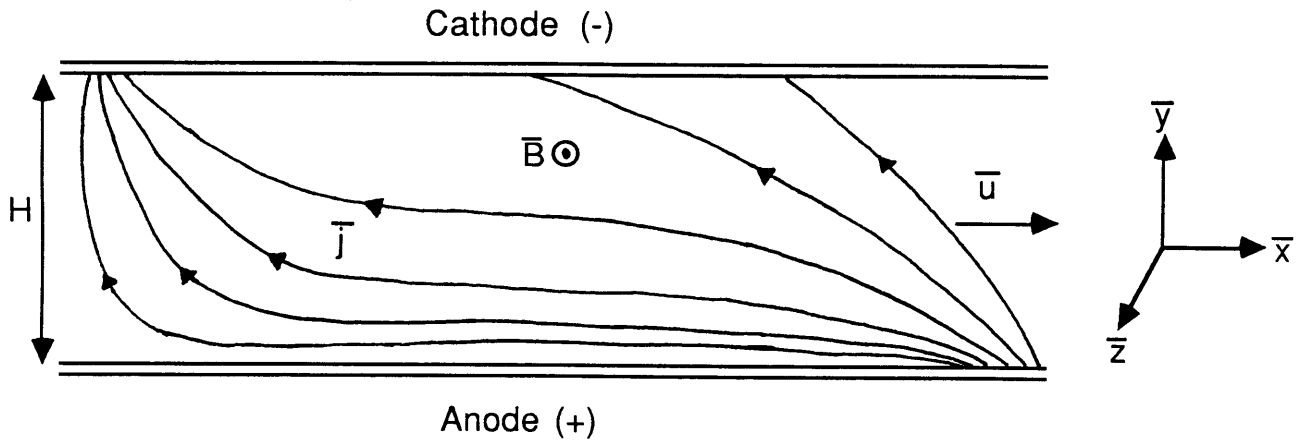

Figure 2.1: Diagram of 2D Magnetoplasmadynamic Channel Flow

flow can be developed. Figure 2.1 shows a diagram of this flow, and is essentially an approximation to the lower portion of the MPD thruster of Figure 1.1. For simplicity, a constant area channel such as that shown in Figure 2.1 is modeled. Only first ionization is considered, and the plasma is assumed to be macroscopically neutral ($n_e = n_i$). Strong coupling is assumed between the ions and neutrals, designated together as the heavy species. This implies that $\vec{u}_i \cong \vec{u}_n \cong \vec{u}$ (except for ambipolar diffusion), and $T_i \cong T_n \cong T_g$. Thus this is a two fluid model which separately tracks electron and heavy species quantities, although transport properties can be calculated for the ions and neutrals separately and their individual velocities may be extracted in an approximate sense. Variations in flow quantities in the z-direction are neglected by the two dimensional model, an assumption which is reasonable because of the axial symmetry in the coaxial class of MPD thrusters currently being tested. The model could easily be modified to an axially symmetric formulation, in order to obtain results which more accurately reflect the geometry of these thrusters. Since this investigation is concerned primarily with the development and effect of viscous and diffusive regions, however, a two-dimensional model is retained initially in order to preserve the symmetry of these regions. The magnetic field is assumed to have a component in the z-direction only, although it may vary in magnitude over the xy-plane. The individual species are assumed to obey the ideal gas law. Radiative processes are neglected in this model, as their effects on MPD flows in the regime of this research has been shown to be minimal (less than 1%) by Sheppard[34]. The working fluid of this model is Argon, which has an atomic mass of $6.634 \times 10^{-26} kg$, a gas constant of $208.13 m^{-1} s^{-2} K^{-1}$, and a first ionization potential of 15.79V.

2.2.1 Magnetic Field Equation

The magnetic field equation is derived from the electron momentum equation and Maxwell's Equations. Using the definitions of current density, $\vec{j} = en_e(\vec{u}_i - \vec{u}_e)$, and electrical conductivity (cf. Section 2.2.5), the well known generalized Ohm's Law may be obtained:

$$\sigma(\vec{E} + \vec{u} \times \vec{B}) = \vec{j} + \vec{j} \times \vec{\beta} - \frac{e}{m_e \sum_r \nu_{er}} \nabla p_e \tag{2.16}$$

where β is the Hall parameter, given by

$$\beta = \frac{eB}{m_e \sum_r \nu_{er}} \tag{2.17}$$

The current density is eliminated from Ohm's Law by using Ampere's Law (Eqn. 2.2) with $\epsilon_0 \frac{\partial \vec{E}}{\partial t}$ neglected. This time-varying electric field term can be disregarded because since ϵ_0 is small, the only significant variations occur on time scales much smaller than encountered in this application. Also, the electric field can be eliminated by taking the curl of the resulting equation and substituting Equation 2.1, $\nabla \times \vec{E} = -\frac{\partial \vec{B}}{\partial t}$. We are left with the expression

$$\begin{aligned} -\frac{\partial \vec{B}}{\partial t} + \nabla \times (\vec{u} \times \vec{B}) &= -\frac{1}{\mu_0 \sigma} \nabla^2 \vec{B} + \frac{1}{\mu_0} \nabla \left(\frac{1}{\sigma}\right) \times (\nabla \times \vec{B}) \\ &+ \frac{1}{\mu_0} \nabla \left(\frac{1}{en_e}\right) \times \left[(\nabla \times \vec{B}) \times \vec{B}\right] - \nabla \left(\frac{1}{en_e}\right) \times \nabla p_e \end{aligned} \tag{2.18}$$

Assuming that $\vec{B} = B\hat{z}$ and simplifying, we arrive at the 2D magnetic field equation:

$$\begin{aligned} &\frac{\partial B}{\partial t} + \frac{\partial uB}{\partial x} + \frac{\partial vB}{\partial y} - \frac{1}{\mu_0 \sigma} \left(\frac{\partial^2 B}{\partial x^2} + \frac{\partial^2 B}{\partial y^2}\right) - \left(\frac{1}{\mu_0 \sigma^2} \frac{\partial \sigma}{\partial x} + \frac{m_e B}{e \rho_e^2 \mu_0} \frac{\partial \rho_e}{\partial y}\right) \frac{\partial B}{\partial x} \\ &- \left(\frac{1}{\mu_0 \sigma^2} \frac{\partial \sigma}{\partial y} - \frac{m_e B}{e \rho_e^2 \mu_0} \frac{\partial \rho_e}{\partial x}\right) \frac{\partial B}{\partial y} = \frac{m_e}{e \rho_e^2} \left(\frac{\partial \rho_e}{\partial x} \frac{\partial p_e}{\partial y} - \frac{\partial \rho_e}{\partial y} \frac{\partial p_e}{\partial x}\right) \end{aligned} \tag{2.19}$$

2.2.2 Mass Conservation Equations

From Equation 2.8, the three species continuity equations which which govern 2-D magnetoplasmadynamic flow can be written as

$$\frac{\partial \rho_e}{\partial t} + \frac{\partial \rho_e u_e}{\partial x} + \frac{\partial \rho_e v_e}{\partial y} = m_e \dot{n}_e \tag{2.20}$$

$$\frac{\partial \rho_i}{\partial t} + \frac{\partial \rho_i u_i}{\partial x} + \frac{\partial \rho_i v_i}{\partial y} = m_a \dot{n}_e \tag{2.21}$$

$$\frac{\partial \rho_n}{\partial t} + \frac{\partial \rho_n u_n}{\partial x} + \frac{\partial \rho_n v_n}{\partial y} = -m_a \dot{n}_e \tag{2.22}$$

where $\dot{n}_e$ represents the net gain of electrons per unit volume through collisional processes. Summing the above three equations results in the overall statement of mass conservation:

$$\frac{\partial \rho}{\partial t} + \frac{\partial \rho u}{\partial x} + \frac{\partial \rho v}{\partial y} = 0 \tag{2.23}$$

where $\rho \cong \rho_n + \rho_i$ The ion equation (Eqn. 2.21) is the only other continuity equation required. We can modify this equation by introducing the ion slip velocity, $\vec{V_i}$, such that

$$\vec{u_i} = \vec{u} + \vec{V_i} \tag{2.24}$$

where $\vec{u}$ is the mean flow velocity. Together with the assumption of plasma neutrality, this results in the following form of the ion continuity equation:

$$\frac{\partial \rho_e}{\partial t} + \nabla \cdot (\rho_e \vec{u}) = m_e \dot{n}_e - \nabla \cdot \left(\rho_e \vec{V_i}\right) \tag{2.25}$$

Assuming that the ion slip is driven primarily by transverse concentration gradients and ignoring differential inertia forces, this implies that

$$\rho_e \vec{V_i} \cong -D_a \frac{\partial \rho_e}{\partial y} \tag{2.26}$$

Substituting this into Equation 2.25 produces the final form of the second 2-D continuity equation:

$$\frac{\partial \rho_e}{\partial t} + \frac{\partial \rho_e u}{\partial x} + \frac{\partial \rho_e v}{\partial y} = m_e \dot{n}_e + \frac{\partial}{\partial y}\left(D_a \frac{\partial \rho_e}{\partial y}\right) \tag{2.27}$$

We need only define $\dot{n}_e$ and the ambipolar diffusion term to complete the derivation of the mass conservation governing equations.

The net electron production rate in Equation 2.27 is given by the Hinnov-Hirshberg model of ionization and three-body recombination[3,11,25]:

$$\dot{n}_e = \dot{n}_e^{HH} = R n_e \left(S n_n - n_e^2\right) \tag{2.28}$$

where

$$R = \frac{1.09 \times 10^{-20}}{T_e^{\frac{9}{2}}} \tag{2.29}$$

$$S = 12\left(\frac{2\pi m_e kT_e}{h^2}\right)^{\frac{3}{2}} e^{-\frac{E_i}{kT_e}} \tag{2.30}$$

The ambipolar diffusion term can be derived from the electron and ion transverse momentum equations, with the assumption that there is no heavy particle flux through the walls. This term arises from the combined action of the electron and ion pressure gradients and electrostatic coupling between the two species. The net effect is that the electrons are slowed and the ions are accelerated with respect to their corresponding free diffusion rates, so that the two species diffuse together at a rate which is somewhere in between. The ambipolar diffusion coefficient is given by

$$D_a = \sqrt{\frac{\pi k T_g}{4 m_a}} \frac{\left(1 + \frac{T_e}{T_g}\right)}{Q_{in}(n_e + n_n)} \tag{2.31}$$

2.2.3 Momentum Conservation Equations

Summing the three species momentum equations defined by Equation 2.12 results in an overall momentum equation. In this process the collisional momentum terms and the electric field terms cancel, so that by also neglecting electron viscous terms we arrive at the following two-dimensional form:

$$\frac{\partial \rho u}{\partial t} + \frac{\partial(\rho u^2 + p - \tau_{xx})}{\partial x} + \frac{\partial(\rho uv - \tau_{xy})}{\partial y} = e n_e (u_e - u_i) B \tag{2.32}$$

$$\frac{\partial \rho v}{\partial t} + \frac{\partial(\rho uv - \tau_{xy})}{\partial x} + \frac{\partial(\rho v^2 + p - \tau_{yy})}{\partial y} = e n_e (v_e - v_i) B \tag{2.33}$$

where the shear stress components are

$$\tau_{xx} = \frac{4}{3}\mu\frac{\partial u}{\partial x} - \frac{2}{3}\mu\frac{\partial v}{\partial y} \tag{2.34}$$

$$\tau_{yy} = \frac{4}{3}\mu\frac{\partial v}{\partial y} - \frac{2}{3}\mu\frac{\partial u}{\partial x} \tag{2.35}$$

$$\tau_{xy} = \mu\frac{\partial u}{\partial y} + \mu\frac{\partial v}{\partial x} \tag{2.36}$$

Using the definition of current density and Ampere's Law (Eqn. 2.2) excluding the time-varying component, the following conservative form of the overall momentum equations can be achieved:

$$\frac{\partial \rho u}{\partial t} + \frac{\partial(\rho u^2 + p + \frac{B^2}{2\mu_0} - \tau_{xx})}{\partial x} + \frac{\partial(\rho uv - \tau_{xy})}{\partial y} = 0 \tag{2.37}$$

$$\frac{\partial \rho v}{\partial t} + \frac{\partial(\rho uv - \tau_{xy})}{\partial x} + \frac{\partial(\rho v^2 + p + \frac{B^2}{2\mu_0} - \tau_{yy})}{\partial y} = 0 \tag{2.38}$$

2.2.4 Energy Conservation Equations

Heavy Species

Since the ions and neutrals are assumed to be strongly coupled, we may combine the energy conservation equations for each species (Eqn. 2.15) to obtain a heavy species energy equation. The collisional terms between the ions and neutrals cancel, so that by writing out the viscous terms, and using the definition of specific heat and the equation of state for the heavy species, we are left with the following expression in two dimensions:

$$\frac{\partial}{\partial t}\left(\frac{p_g}{(\gamma-1)}\right) + \frac{\partial}{\partial t}\left(\frac{1}{2}\rho(u^2+v^2)\right) + \frac{\partial u(\frac{\gamma}{\gamma-1}p_g + \frac{1}{2}\rho(u^2+v^2))}{\partial x} + \frac{\partial v(\frac{\gamma}{\gamma-1}p_g + \frac{1}{2}\rho(u^2+v^2))}{\partial y}$$

$$- \frac{\partial(u\tau_{xx} + v\tau_{xy})}{\partial x} - \frac{\partial(u\tau_{xy} + v\tau_{yy})}{\partial y} + \frac{\partial q_{gx}}{\partial x} + \frac{\partial q_{gy}}{\partial y} = E_l \tag{2.39}$$

Here it has also been assumed that the current is carried primarily by the electrons. The terms of the shear stress tensor are given as before, and the remaining collisional term on the right-hand side represents elastic collisional energy transfer between heavy species and electrons:

$$E_l = 3\frac{\rho_e}{m_a}(\nu_{ei} + \nu_{en})k(T_e - T_g) \tag{2.40}$$

The heat flux terms have been defined to reflect their dependence on heavy species quantities as

$$q_{gx} = -k_g\left(\frac{\partial T_g}{\partial x}\right) \qquad q_{gy} = -k_g\left(\frac{\partial T_g}{\partial y}\right) \tag{2.41}$$

Equation 2.39 can be simplified by introducing the heavy species total energy and enthalpy per unit mass:

$$E_g = \frac{p_g}{(\gamma-1)\rho} + \frac{1}{2}\left(u^2+v^2\right) \tag{2.42}$$

$$H_g = E_g + \frac{p_g}{\rho} \tag{2.43}$$

This results in the following form of the heavy species energy equation:

$$\frac{\partial \rho E_g}{\partial t} + \frac{\partial(\rho u H_g - u\tau_{xx} - v\tau_{xy} + q_{gx})}{\partial x} + \frac{\partial(\rho v H_g - u\tau_{xy} - v\tau_{yy} + q_{gy})}{\partial y} = E_l \tag{2.44}$$

For computational purposes it is often useful to rewrite the heavy species energy equation in terms of the internal energy of the gas, e_g, defined by

$$E_g = e_g + \frac{1}{2}\left(u^2 + v^2\right) \tag{2.45}$$

Taking the dot product of the overall momemtum equation with the fluid velocity and substituting into the heavy species energy equation (Eqn. 2.44) results in the following alternative form of the energy equation:

$$\rho\frac{\partial e_g}{\partial t} + \rho u\frac{\partial e_g}{\partial x} + \rho v\frac{\partial e_g}{\partial y} + p\frac{\partial u}{\partial x} + p\frac{\partial v}{\partial y} - \frac{\partial}{\partial x}\left(k_g\frac{\partial T_g}{\partial x}\right) - \frac{\partial}{\partial y}\left(k_g\frac{\partial T_g}{\partial y}\right) = \Phi + E_l \tag{2.46}$$

where Φ is the viscous dissipation function, given by

$$\Phi = \mu\left[2\left(\frac{\partial u}{\partial x}\right)^2 + 2\left(\frac{\partial v}{\partial y}\right)^2 + \left(\frac{\partial v}{\partial x} + \frac{\partial u}{\partial y}\right)^2 - \frac{2}{3}\left(\frac{\partial u}{\partial x} + \frac{\partial v}{\partial y}\right)^2\right] \tag{2.47}$$

This alternative form is especially useful in MPD calculations, because the kinetic energy of the flow attains such a high value through electromagnetic acceleration that it dwarfs the internal energy component of the unsteady term in the heavy species energy conservation equation, potentially leading to a loss of information or non-physical results depending on the values of the energy flux terms. Although this internal energy formulation is not conservative, it is accurate so long as the problem is free of shocks or other discontinuities.

Electrons

The electron energy equation is given directly by Equation 2.15. Neglecting electron shear terms, and again using the definition of specific heat and the electron equation of state, we obtain

$$\frac{\partial}{\partial t}\left(\frac{p_e}{(\gamma-1)}\right) + \frac{\partial}{\partial t}\left(\frac{1}{2}\rho_e(u_e^2+v_e^2)\right) + \frac{\partial u_e\left(\frac{\gamma}{\gamma-1}p_e + \frac{1}{2}\rho_e(u_e^2+v_e^2)\right)}{\partial x}$$

$$+ \frac{\partial v_e\left(\frac{\gamma}{\gamma-1}p_e + \frac{1}{2}\rho_e(u_e^2+v_e^2)\right)}{\partial y} + \frac{\partial q_{ex}}{\partial x} + \frac{\partial q_{ey}}{\partial y} = \frac{j^2}{\sigma} - E_l - \dot{n}_e E_i \tag{2.48}$$

where the heat flux terms and the collisional term E_l are defined as in the heavy species energy equation, and $\frac{j^2}{\sigma}$ is the Joule heating or Ohmic dissipation term. Defining total

energy and enthalpy per unit mass as with the heavy species, we arrive at the following expression:

$$\frac{\partial \rho_e E_e}{\partial t} + \frac{\partial (\rho_e u_e H_e + q_{ex})}{\partial x} + \frac{\partial (\rho_e v_e H_e + q_{ey})}{\partial y} = \frac{j^2}{\sigma} - E_l \tag{2.49}$$

where

$$E_e = \frac{p_e}{(\gamma - 1)\rho_e} + \frac{1}{2}\left(u_e^2 + v_e^2\right) + \frac{E_i}{m_e} \tag{2.50}$$

$$H_e = E_e + \frac{p_e}{\rho_e} \tag{2.51}$$

Note that in this formulation, the ionization energy of the gas is defined as a component of the total energy of the electron species. In order to increase efficiency in numerical computations with the model, it is desirable to eliminate the electron velocities in the flux terms of Equation 2.49. This is accomplished by neglecting the inertial terms, recalling that $\vec{u}_i \cong \vec{u}_n \cong \vec{u}$, and using the definition of current density and the electron equation of state. Consequently the final form of the electron energy equation is

$$\frac{\partial \rho_e E_e}{\partial t} + \frac{\partial \left(-j_x \left(\frac{E_i}{e} + \frac{\gamma k T_e}{(\gamma-1)e}\right) + q_{ex}\right)}{\partial x} + \frac{\partial \left(-j_y \left(\frac{E_i}{e} + \frac{\gamma k T_e}{(\gamma-1)e}\right) + q_{ey}\right)}{\partial y} = \frac{j^2}{\sigma} - E_l \tag{2.52}$$

2.2.5 Additional Equations

Additional equations required in the model are Ampere's Law in two dimensions (neglecting the time-varying electric field), the definition of current density, and the overall equation of state.

$$j_x = \frac{1}{\mu_0}\frac{\partial B}{\partial y} \qquad j_y = -\frac{1}{\mu_0}\frac{\partial B}{\partial x} \tag{2.53}$$

$$j_x = en_e(u - u_e) \qquad j_y = en_e(v - v_e) \tag{2.54}$$

$$p = \rho R_g T_g + \rho_e R_e T_e \tag{2.55}$$

2.2.6 Transport Properties

In general, for a plasma in the presence of magnetic and electric fields, the transport properties are functions of the direction of transport with respect to these fields. The transport equations thus become tensor equations. For example, the generalized Ohm's

Law of Equation 2.16, neglecting ion currents, pressure gradients, and the Hall term, can be written in tensor notation as $\vec{j}_e = \overline{\overline{\sigma}} \cdot \vec{E}'$. Here $\overline{\overline{\sigma}}$ is the electrical conductivity tensor, or dyad. For the case of a magnetic field in the $\hat{z}$ direction only, the equivalent expression in terms of matrices is

$$\begin{bmatrix} j_{ex} \\ j_{ey} \\ j_{ez} \end{bmatrix} = \begin{bmatrix} \sigma_\perp & -\sigma_H & 0 \\ \sigma_H & \sigma_\perp & 0 \\ 0 & 0 & \sigma_\parallel \end{bmatrix} \begin{bmatrix} E'_x \\ E'_y \\ E'_z \end{bmatrix} \tag{2.56}$$

where

$$\sigma_\parallel \sim \frac{e^2 n_e}{m_e \sum_r \nu_{er}} \qquad \sigma_\perp = \frac{\sigma_\parallel}{1+\beta^2} \qquad \sigma_H = \frac{\beta \sigma_\parallel}{1+\beta^2} \tag{2.57}$$

and β is the Hall Parameter. The quantity $\sigma_\parallel$ is called the longitudinal conductivity, as it governs the flow of current in the direction parallel to the magnetic field. The quantity $\sigma_\perp$ is the perpendicular or transverse conductivity, which controls electrical current in the direction perpendicular to the magnetic field and parallel to the electric field component. Finally, σ_H, denoted as the Hall conductivity, governs current flow in the direction perpendicular to both the magnetic field and the electric field component. In this two-dimensional model there is no $\hat{z}$-component of the current density or electric field, and for simplicity the plasma is assumed to be isotropic, so that $\sigma_\perp = \sigma_\parallel$ and $\sigma_H = 0$. The electron and heavy species thermal conductivities are similarly formulated in tensor notation, and also considered to be isotropic functions. Thermal diffusion is not included in this model.

Electrical Conductivity

The scalar electrical conductivity for a plasma is given approximately by

$$\sigma = \frac{e^2 n_e}{m_e \sum_r \nu_{er}} \tag{2.58}$$

Spitzer and Härm[35] used numerical integration techniques to solve for the electron transport properties of a plasma in the limit of full ionization, yielding coefficient corrections to the simplified analytic expressions. The value of the electrical conductivity coefficient was found to be 1.975. Although closed-form expressions for the transport properties of a plasma at an arbitrary level of ionization are not obtainable, approximate forms can be obtained by expanding the transport equations in terms of Sonine polynomials. This leads to the following approximate equation for electrical conductivity, valid

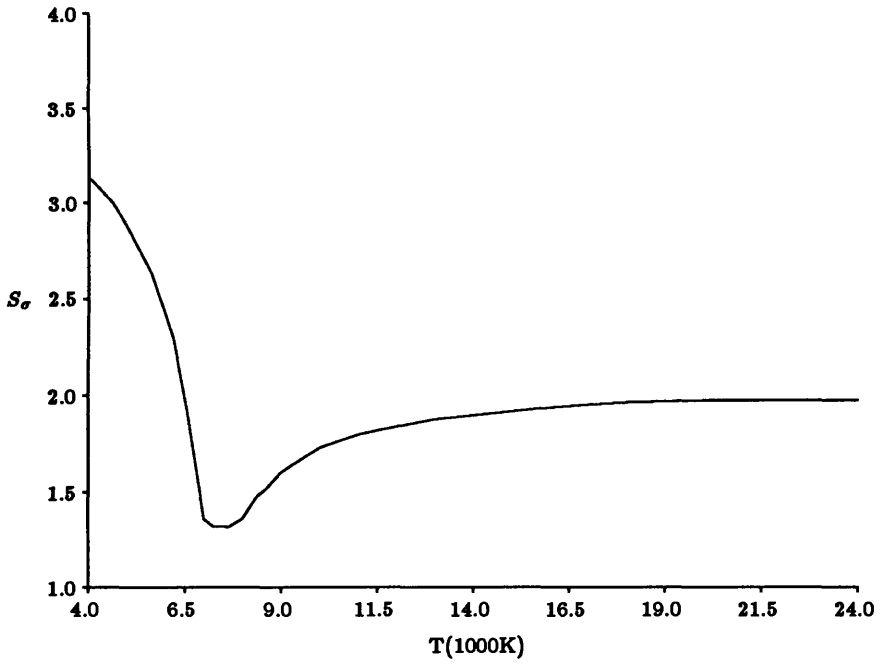

Figure 2.2: Correction Coefficient by 12th Order Sonine Polynomial Approximation for Argon Electrical Conductivity

for any level of ionization, where now the correction coefficient has become a function of electron temperature:

$$\sigma = S_\sigma(T_e)\frac{e^2 n_e}{m_e \bar{c}_e \left(n_e Q_{ei} + n_n Q_{en}\right)} \tag{2.59}$$

The coefficient S_σ is interpolated from a 12th order Sonine polynomial approximation by Mitchner and Kruger[25], and is plotted for a pressure of one atmosphere in Figure 2.2. Figure 2.3 shows electrical conductivity versus temperature calculated from this model, for Argon in ionizational equilibrium.

Thermal Conductivity

The coefficients of thermal conductivity for the electrons and heavy species are defined in a manner similar to that used for the electrical conductivity:

$$k_e = S_k \frac{n_e k^2 T_e}{m_e \sum_r \nu_{er}} = S_k \frac{n_e k^2 T_e}{m_e \bar{c}_e \left(n_e Q_{ei} + n_n Q_{en}\right)} \tag{2.60}$$

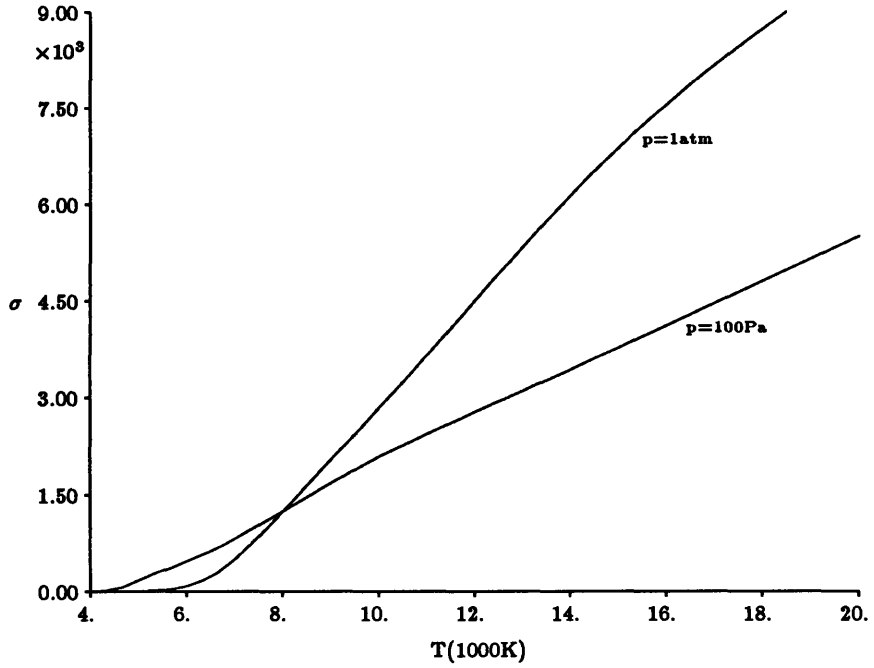

Figure 2.3: Equilibrium Argon Electrical Conductivity

$$k_g = S_k \frac{k^2 T_g}{m_a \bar{c}_g} \left[\frac{n_n}{n_n Q_{nn} + n_e Q_{in}} + \frac{n_e}{n_e Q_{ii} + n_n Q_{in}} \right] \tag{2.61}$$

In each case the simplified analytic expression for the transport coefficient is multiplied by a correction coefficient based on a 12th order Sonine polynomial approximation. Note, however, that the heavy species thermal conductivity coefficient is based on a mixture rule which incorporates contributions from both neutral and singly ionized atoms. The correction coefficient S_k is plotted in Figure 2.4 as a function of temperature, while k_e and k_g are plotted in Figures 2.5 and 2.6, respectively, for Argon in ionizational equilibrium. The graph of k_e versus temperature appears similar to the previous plot of electrical conductivity, with k_e increasing monotonically at a rate dependent on the pressure of the gas. The plot of k_g versus temperature in Figure 2.6, however, shows two minima. The first is due to the minimum of the correction coefficient S_k at approximately $7000°K$, while the second arises from the fact that k_g is actually a combination of ion and neutral thermal conductivities. At low temperature the much larger neutral thermal conductivity dominates, while at higher temperatures the gas eventually becomes fully ionized, at which point the lower ion thermal conductivity is the only contributor to k_g. Both the ion and neutral thermal conductivity coefficients increase with increasing temperature. As seen in Figure 2.6, the location of the transition region between neutral-dominated

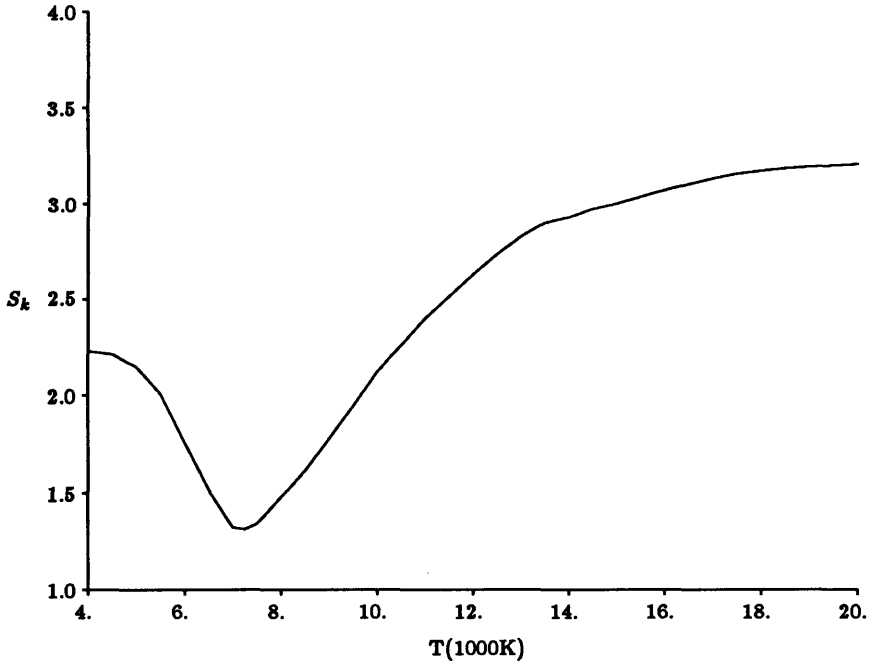

Figure 2.4: Correction Coefficient by 12th Order Sonine Polynomial Approximation for Argon Thermal Conductivity

and ion-dominated heavy species thermal conductivity depends on pressure, for a gas in ionizational equilibrium.

Viscosity

The coefficient of viscosity for the fluid can be expressed as a mixture rule derived by Mitchner and Kruger[25]:

$$\mu = \sum_s \left(\frac{n_s}{\sum_r n_r M_{sr}} \right) \mu_s \tag{2.62}$$

where

$$M_{sr} = \sqrt{\frac{2m_{sr}}{m_s}} \frac{Q_{sr}}{Q_{ss}} \tag{2.63}$$

and the individual species viscosity coefficients are given by

$$\mu_s = \frac{1}{2} m_s n_s \bar{c}_s \lambda_s = \frac{\frac{1}{2} m_s \bar{c}_s}{\sqrt{2} Q_{ss}} \tag{2.64}$$

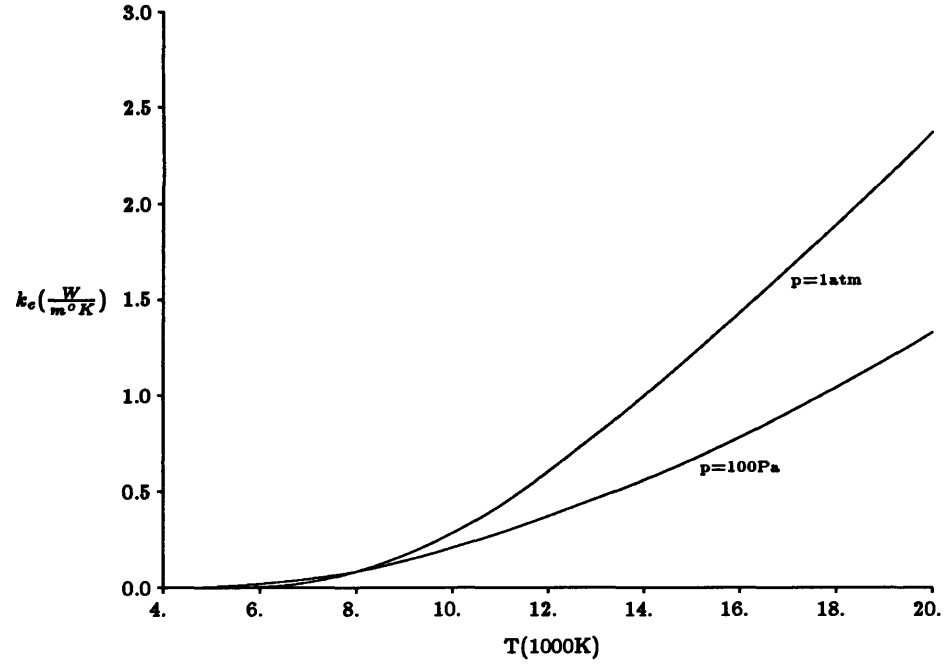

Figure 2.5: Equilibrium Electron Coefficient of Thermal Conductivity

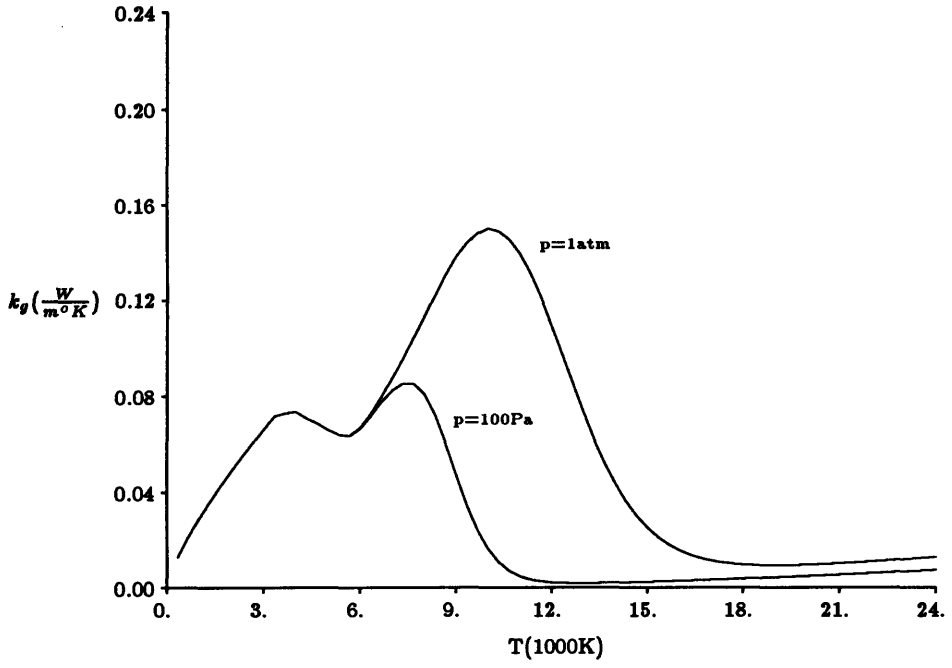

Figure 2.6: Equilibrium Argon Heavy Species Coefficient of Thermal Conductivity

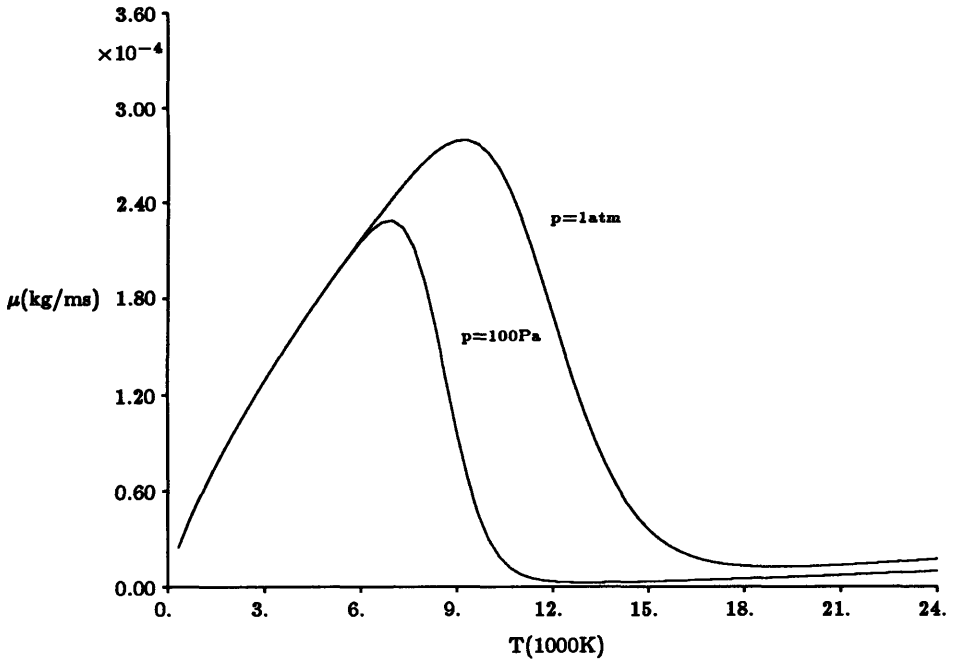

Figure 2.7: Equilibrium Coefficient of Viscosity for Argon

The summations on s and r are performed over the neutral and ion species; the contribution of electrons to the viscosity coefficient is ignored. Both neutral and ion viscosity coefficients increase with increasing temperature, but the neutral species component is more than an order of magitude greater than the ion species component. Combining Eqns. 2.62 - 2.64 results in the following analytic formula:

$$\mu = \frac{\frac{1}{2} m_a \bar{c}_g}{\sqrt{2}} \left[\frac{n_n}{n_n Q_{nn} + n_e Q_{in}} + \frac{n_e}{n_n Q_{in} + n_e Q_{ii}} \right] \tag{2.65}$$

The coefficient of viscosity is plotted in Figure 2.7 versus temperature for Argon gas in ionizational equilibrium. Initially as the temperature is increased μ increases, because the gas is mostly neutral and so the higher neutral species viscosity dominates. As the gas becomes more strongly ionized, however, the ion species viscosity begins to dominate, causing the gas viscosity coefficient to decrease rapidly. Once the ion viscosity is predominant, the overall viscosity again increases with temperature, although at a slower rate. As seen with the heavy species thermal conductivity, which is also defined by a mixture rule, the location of the transition region is dependent upon the pressure of the gas, assuming ionizational equilibrium.

Collision Cross-Sections

Collision cross-sections involving neutral species are taken from empirical formulas developed for Argon, the propellant considered in this research (Jaffrin[12], Lieberman and Velikovich[19]):

$$Q_{in} = 1.4 \times 10^{-18} \qquad [m^2] \tag{2.66}$$

$$Q_{nn} = 1.7 \times 10^{-18} T_g^{\frac{1}{4}} \qquad [m^2] \tag{2.67}$$

$$\begin{aligned} Q_{en} &= \left(.713 - 4.5 \times 10^{-4} T_e + 1.5 \times 10^{-7} T_e^2\right) \times 10^{-20} \quad [m^2] \quad (T_e \leq 3000^o K) \\ &= \left(-.488 + 3.96 \times 10^{-4} T_e\right) \times 10^{-20} \quad [m^2] \qquad\qquad (T_e > 3000^o K) \end{aligned} \tag{2.68}$$

Collisions between charged particles are treated analytically as summarized in Mitchner and Kruger[25], resulting in the following expressions:

$$Q_{ei} = Q_{ee} = \frac{e^4 \ln \Lambda}{24\pi \left(\epsilon_0 k T_e\right)^2} \tag{2.69}$$

$$Q_{ii} = \frac{e^4 \ln \Lambda}{24\pi \left(\epsilon_0 k T_g\right)^2} \tag{2.70}$$

where $\ln \Lambda$ is the Spitzer logarithm, given by

$$\Lambda = \frac{12\pi (\epsilon_0 k T_e)^{\frac{3}{2}}}{e^3 n_e^{\frac{1}{2}}} = 1.239 \times 10^7 \left(\frac{T_e^3}{n_e}\right)^{\frac{1}{2}} \tag{2.71}$$

The empirical, non-coulombic cross-sections are plotted versus temperature in Figure 2.8, while the coulombic cross section, Q_c, is shown in Figure 2.9.

2.3 Simplified Quasi-2D Model

Equations 2.19, 2.27, 2.23, 2.37, 2.38, 2.44,and 2.52-2.55 comprise the two-dimensional model of MPD channel flow. In order to gain an initial understanding of the viscous and diffusive effects involved and to reduce the complexity of the numerical solution and the computer run time, it was decided to discard the magnetic field equation and instead assume that the magnetic field distribution is given by the quasi one-dimensional solution of an analogous problem by the method of Niewood[27]. The difficulty is that the time scale for magnetic diffusion is more than 100 times smaller than the time scale

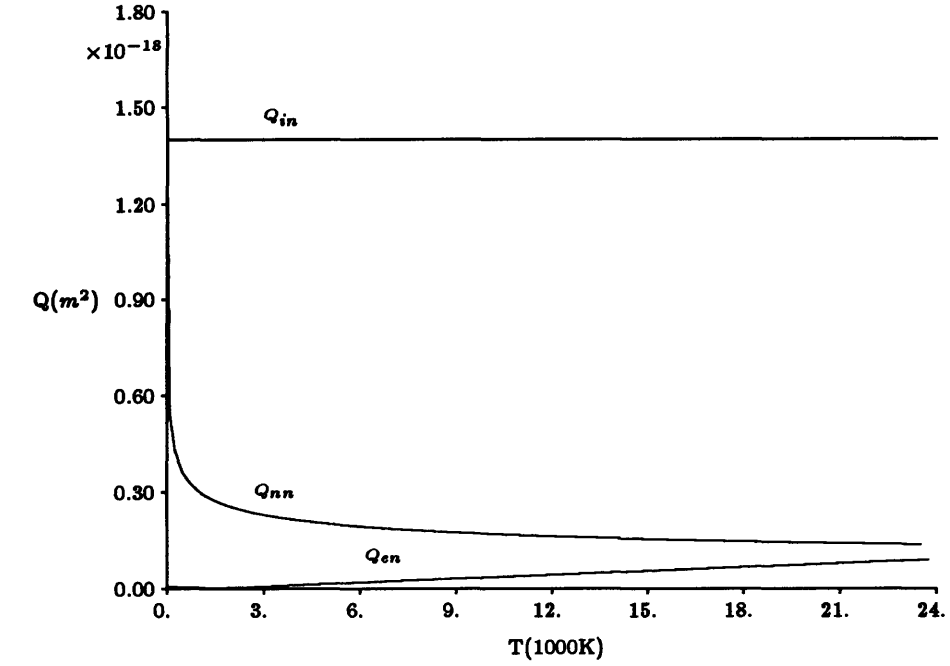

Figure 2.8: Argon Non-Coulombic Collision Cross-Sections

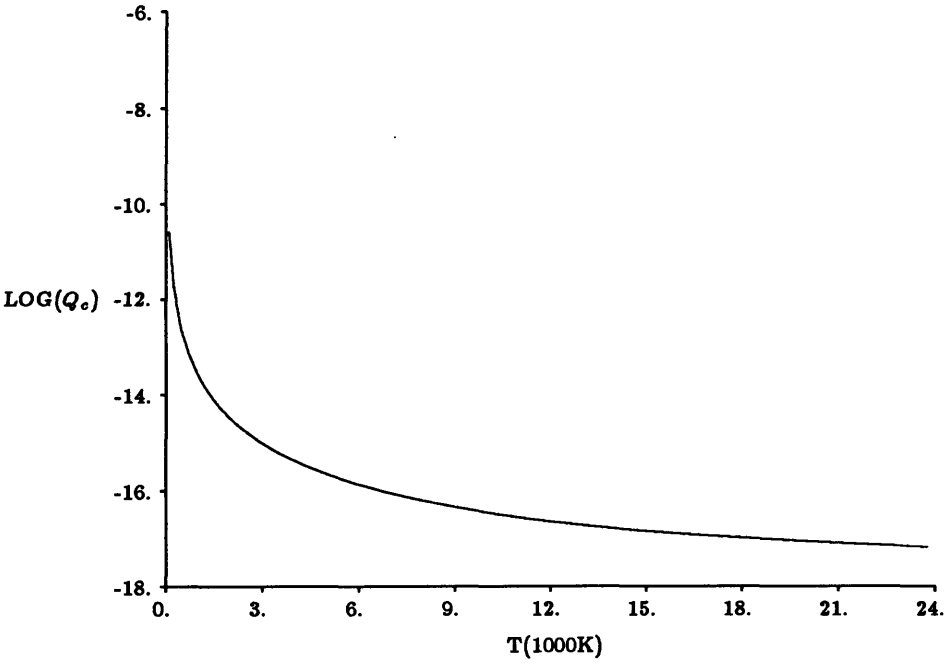

Figure 2.9: Argon Coulombic Collision Cross-Section

for fluid diffusion, so that much more computation time would be added to an already time-intensive modified Navier-Stokes code in order to obtain a solution. In addition, the fully two-dimensional time-varying magnetic field would create large unsymmetries in the solution, which would detract from the initial aim to examine boundary layer evolution and diffusive effects in the flow. This simplification will be relaxed in later work on this model in order to achieve a more self-consistent, fully two-dimensional flow solution, which incorporates phenomena such as the Hall effect and the resulting concentration of the current near the cathode root and the anode tip. With this assumption, the simplified model of two-dimensional MPD channel flow can be restated as the following set of equations:

$$\frac{\partial \rho}{\partial t} + \frac{\partial \rho u}{\partial x} + \frac{\partial \rho v}{\partial y} = 0 \tag{2.72}$$

$$\frac{\partial \rho_e}{\partial t} + \frac{\partial \rho_e u}{\partial x} + \frac{\partial \rho_e v}{\partial y} = m_e \dot{n}_e^{HH} + \frac{\partial}{\partial y}\left(D_a \frac{\partial \rho_e}{\partial y}\right) \tag{2.73}$$

$$\frac{\partial \rho u}{\partial t} + \frac{\partial (\rho u^2 + p + \frac{B^2}{2\mu_0} - \tau_{xx})}{\partial x} + \frac{\partial (\rho uv - \tau_{xy})}{\partial y} = 0 \tag{2.74}$$

$$\frac{\partial \rho v}{\partial t} + \frac{\partial (\rho uv - \tau_{xy})}{\partial x} + \frac{\partial (\rho v^2 + p + \frac{B^2}{2\mu_0} - \tau_{yy})}{\partial y} = 0 \tag{2.75}$$

$$\frac{\partial \rho E_g}{\partial t} + \frac{\partial (\rho u H_g - u\tau_{xx} - v\tau_{xy} + q_{gx})}{\partial x} + \frac{\partial (\rho v H_g - u\tau_{xy} - v\tau_{yy} + q_{gy})}{\partial y} = E_l \tag{2.76}$$

$$\frac{\partial \rho_e E_e}{\partial t} + \frac{\left(-j_x \left(\frac{E_i}{e} + \frac{\gamma k T_e}{(\gamma-1)e}\right) + q_{ex}\right)}{\partial x} + \frac{\left(-j_y \left(\frac{E_i}{e} + \frac{\gamma k T_e}{(\gamma-1)e}\right) + q_{ey}\right)}{\partial y} = \frac{j^2}{\sigma} - E_l \tag{2.77}$$

$$p = \rho R_g T_g + \rho_e R_e T_e \tag{2.78}$$

$$j_x = \frac{1}{\mu_0}\frac{\partial B}{\partial y} \qquad j_y = -\frac{1}{\mu_0}\frac{\partial B}{\partial x} \tag{2.79}$$

$$j_x = en_e(u - u_e) \qquad j_y = en_e(v - v_e) \tag{2.80}$$

Chapter 3
Numerical Method

The set of equations governing magnetoplasmadynamic channel flow is essentially a modified form of the compressible Navier-Stokes equations. In two dimensions and Cartesian coordinates, the Navier-Stokes equations can be expressed in the following simplified conservative form, neglecting body forces and external source terms:

$$\frac{\partial \mathbf{U}}{\partial t} + \frac{\partial \mathbf{F}}{\partial x} + \frac{\partial \mathbf{G}}{\partial y} = 0 \tag{3.1}$$

U is a state vector and **F** and **G** are flux vectors given by

$$\mathbf{U} = \begin{bmatrix} \rho \\ \rho u \\ \rho v \\ \rho E \end{bmatrix}$$

$$\mathbf{F} = \begin{bmatrix} \rho u \\ \rho u^2 + p - \tau_{xx} \\ \rho uv - \tau_{xy} \\ \rho uH - u\tau_{xx} - v\tau_{xy} + q_x \end{bmatrix} \tag{3.2}$$

$$\mathbf{G} = \begin{bmatrix} \rho v \\ \rho uv - \tau_{xy} \\ \rho v^2 + p - \tau_{yy} \\ \rho vH - u\tau_{xy} - v\tau_{yy} + q_y \end{bmatrix}$$

with the shear and heat flux terms given by

$$\tau_{xx} = \frac{2}{3}\mu \left(2\frac{\partial u}{\partial x} - \frac{\partial v}{\partial y} \right) \tag{3.3}$$

$$\tau_{yy} = \frac{2}{3}\mu \left(2\frac{\partial v}{\partial y} - \frac{\partial u}{\partial x} \right) \tag{3.4}$$

$$\tau_{xy} = \mu\left(\frac{\partial u}{\partial y} + \frac{\partial v}{\partial x}\right) \tag{3.5}$$

$$q_x = -k\frac{\partial T}{\partial x} \qquad q_y = -k\frac{\partial T}{\partial y} \tag{3.6}$$

It was decided to utilize an explicit, second-order accurate numerical algorithm in solving the MPD channel flow equations. Because of the complexity of the equations, which include additional magnetic fluxes and source terms not present in the compressible Navier-Stokes equations, and due to the complex nature of the boundary conditions, particularly at the electrode walls, the simpler application of an explicit scheme is more desirable than that of an implicit method. In addition, since instability analysis is an important component of MPD thruster research, it is advantageous to retain a capability for performing time-dependent calculations with the computer code so that instability studies may be performed. In order to calculate an accurate time evolution of the flow, however, a numerical method should be at least second-order accurate in time; consequently a requirement of overall second-order accuracy was made. Because it satisfies the conditions above and has been proved an excellent means of solving the compressible Navier-Stokes equations for a variety of conditions, Time-Split MacCormack's Method was chosen as the numerical scheme for this research.

3.1 Time-Split MacCormack's Method

MacCormack's Method, developed in 1969 by MacCormack[20], is a two step predictor-corrector scheme based on the Lax-Wendroff Method. The scheme has since been modified to include time-splitting[21], which allows the solution to be advanced in each coordinate direction at the maximum possible time step. The basic algorithm applied to the conservative vector form of the Navier-Stokes equations (Eqn. 3.1) yields:

Axial differencing

Predictor:

$$\mathbf{U}_{ij}^{**P} = \mathbf{U}_{ij}^{*} - \frac{\triangle t_x}{\triangle x}\left(\mathbf{F}_{i+1,j}^{*} - \mathbf{F}_{ij}^{*}\right) \tag{3.7}$$

Corrector:

$$\mathbf{U}_{ij}^{**} = \frac{1}{2}\left[\mathbf{U}_{ij}^{*} + \mathbf{U}_{ij}^{**P} - \frac{\triangle t_x}{\triangle x}\left(\mathbf{F}_{ij}^{**P} - \mathbf{F}_{i-1,j}^{**P}\right)\right] \tag{3.8}$$

Transverse differencing

Predictor:

$$\mathbf{U}_{ij}^{**P} = \mathbf{U}_{ij}^{*} - \frac{\triangle t_y}{\triangle y}\left(\mathbf{G}_{i,j+1}^{*} - \mathbf{G}_{ij}^{*}\right) \tag{3.9}$$

Corrector:

$$\mathbf{U}_{ij}^{**} = \frac{1}{2}\left[\mathbf{U}_{ij}^{*} + \mathbf{U}_{ij}^{**P} - \frac{\triangle t_y}{\triangle y}\left(\mathbf{G}_{ij}^{**P} - \mathbf{G}_{i,j-1}^{**P}\right)\right] \tag{3.10}$$

The asterisks represent dummy time indices, and the superscript P denotes the predicted value of the state vector and associated fluxes at the (i,j)th discrete point.

In order to maintain time accuracy, the solution must be advanced in each coordinate direction for the same interval of time during each integration step. Since in general the maximum allowable time step for stability in each direction is different, this requires that the MacCormack scheme be applied multiple times in the direction with the most time-restrictive stability criteria during each integration step. To quantify this, one-dimensional difference operators are defined as follows:

$$\mathbf{U}_{ij}^{**} = L_x(\triangle t_x)\mathbf{U}_{ij}^{*} \tag{3.11}$$

$$\mathbf{U}_{ij}^{**} = L_y(\triangle t_y)\mathbf{U}_{ij}^{*} \tag{3.12}$$

The integration step may then be divided into some sequence of applications of the one-dimensional operators. The time integration remains second-order accurate provided that the sequence is symmetric, and is consistent if the sums of the time steps of each of the operators are equal. Stability is guaranteed so long as the time step of each operator does not exceed the maximum allowable time step for that operator. The sequence employed in this research is:

$$\mathbf{U}_{ij}^{n+1} = \left[L_y(\frac{\triangle t}{2m})\right]^m L_x(\triangle t)\left[L_y(\frac{\triangle t}{2m})\right]^m \mathbf{U}_{ij}^{n} \tag{3.13}$$

where m is an integer calculated before each time integration to maintain consistency, and $\triangle t$ is the calculated time step in the axial direction, which in this application is generally the largest.

3.2 Stability

Because of the complex nature of the compressible Navier-Stokes equations, an analytic stability expression for Time-Split MacCormack's Method is unattainable. Approx-

imate stability criteria, however, have been estimated by MacCormack and Baldwin[22] based on stability analyses of the convective, diffusive, and viscous terms of the full equations. This results in the following time step limits:

$$\Delta t_x \leq \frac{\sigma \Delta x}{|u| + a + \frac{1}{\rho}\left[\frac{2\gamma\mu}{Pr\Delta x} + \frac{(-\lambda\mu)^{\frac{1}{2}}}{\Delta y}\right]} \tag{3.14}$$

$$\Delta t_y \leq \frac{\sigma \Delta y}{|v| + a + \frac{1}{\rho}\left[\frac{(-\lambda\mu)^{\frac{1}{2}}}{\Delta x} + \frac{2\gamma\mu}{Pr\Delta y}\right]} \tag{3.15}$$

where

$$a = \sqrt{\frac{\gamma p}{\rho}} \tag{3.16}$$

$$Pr = \frac{\mu c_p}{k} \tag{3.17}$$

$$\lambda = -\frac{2}{3}\mu \tag{3.18}$$

The coefficient σ represents a safety factor to account for the nonlinearity of the equations. Because these stability criteria were developed for a single component gas assuming constant transport coefficients and neglecting the prescence of source terms, however, the value of σ used in this research is somewhat smaller than that used for typical compressible flow applications. In practice, the stability criteria are applied at each grid point at the beginning of each integration step, and the smallest time steps calculated are then used at every grid point in advancing the solution. This maintains the time accuracy of the integration procedure.

3.3 Numerical Smoothing

Although the MacCormack scheme contains some inherent smoothing, it is necessary to provide additional dissipative terms to damp numerical oscillations which may arise in regions of steep gradients where the mesh is insufficiently refined. MacCormack and Baldwin[22] have developed a fourth-order product type of smoothing based on a pressure switch, which becomes significant in magnitude only where numerical truncation error is producing pressure oscillations in the solution. The smoothing terms are applied as additional flux terms in the numerical scheme, and are of the following form:

$$\mathbf{SX}_{ij} = \epsilon \Delta x^4 \frac{\partial}{\partial x}\left[\frac{|u| + a}{4p}\left|\frac{\partial^2 p}{\partial x^2}\right|\frac{\partial \mathbf{U}}{\partial x}\right] \tag{3.19}$$

$$\mathbf{SY}_{ij} = \epsilon \triangle y^4 \frac{\partial}{\partial y}\left[\frac{|v|+a}{4p}\left|\frac{\partial^2 p}{\partial y^2}\right|\frac{\partial \mathbf{U}}{\partial y}\right] \tag{3.20}$$

where $0 \leq \epsilon \leq 0.5$ for stability.

3.4 Application to MPD Channel Flow

Time-Split MacCormack's Method is applied to the model problem of this research in a straightforward manner. When the simplified MPD channel equations (Eqn. 2.72 to Eqn. 2.77) are written in the conservative vector form of Eqn. 3.1 with a source term vector, the following representation results:

$$\frac{\partial \mathbf{U}}{\partial t} + \frac{\partial \mathbf{F}}{\partial x} + \frac{\partial \mathbf{G}}{\partial y} = \mathbf{S} \tag{3.21}$$

$$\mathbf{U} = \begin{bmatrix} \rho \\ \rho_e \\ \rho u \\ \rho v \\ \rho E_g \\ \rho_e E_e \end{bmatrix}$$

$$\mathbf{F} = \begin{bmatrix} \rho u \\ \rho_e u \\ \rho u^2 + p + \frac{B^2}{2\mu o} - \tau_{xx} \\ \rho uv - \tau_{xy} \\ \rho u H_g - u\tau_{xx} - v\tau_{xy} + q_{gx} \\ -j_x\left(\frac{E_i}{e} + \frac{\gamma k T_e}{(\gamma-1)e}\right) + q_{ex} \end{bmatrix}$$

$$\mathbf{G} = \begin{bmatrix} \rho v \\ \rho_e v - D_a \frac{\partial \rho_e}{\partial y} \\ \rho uv - \tau_{xy} \\ \rho v^2 + p + \frac{B^2}{2\mu o} - \tau_{yy} \\ \rho v H_g - u\tau_{xy} - v\tau_{yy} + q_{gy} \\ -j_y\left(\frac{E_i}{e} + \frac{\gamma k T_e}{(\gamma-1)e}\right) + q_{ey} \end{bmatrix} \tag{3.22}$$

$$\mathbf{S} = \begin{bmatrix} 0 \\ m_e \dot{n}_e^{HH} \\ 0 \\ 0 \\ E_l \\ \frac{j^2}{\sigma} - E_l \end{bmatrix}$$

Stability criteria are evaluated based on the overall mass and momentum equations, and the heavy species energy equation. Smoothing is applied to all state vector components, based either on a heavy species pressure switch for the overall and heavy species equations, or on an electron pressure switch for the electron equations.

3.4.1 Mesh

The simple geometry of the model problem necessitates nothing more complicated than a Cartesian mesh. In order to resolve steep gradients near the electrode walls due to viscous and boundary effects, however, the grid is exponentially refined in these regions. Also, since one-dimensional analyses have shown that large gradients exist at the inlet of the channel[24,27], exponential grid refinement is utilized in this region as well. A mesh with 75 axial points and 40 transverse points has proven sufficient to accurately resolve the solution to the model problem. Figure 3.1 is an illustration of this mesh.

3.4.2 Boundary Conditions

Inlet

The conditions at the entrance of the channel are postulated to be essentially those of a flow which has just been injected through the MPD thruster backplate by a large number of evenly spaced jets. The flow is therefore assumed to be subsonic and parallel to the electrode walls ($v = 0$). Additionally, the axial velocity, density, and enthalpy are assumed to be constant over the channel cross-section, implying that no boundary layers have yet developed. In application, the inlet mass flow rate, total enthalpy, and ionization fraction are each specified. The total mass flow rate per unit area at the inlet

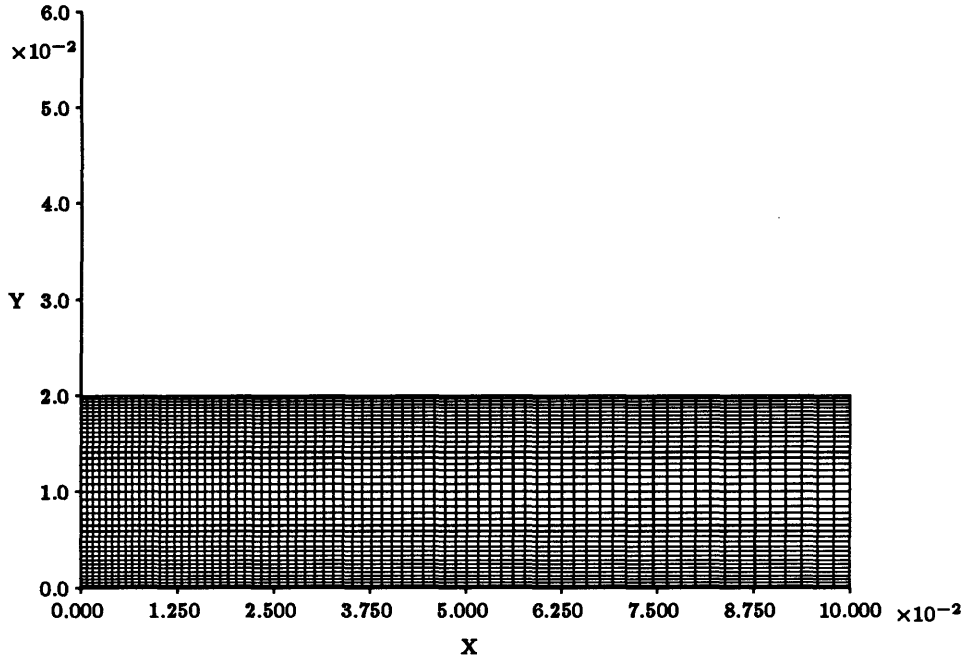

Figure 3.1: Computational Grid for Flow Calculations

is fixed at 0.7 $\frac{kg}{m^2 s}$, based on an initially constant transverse density distribution and axial velocity profile. For a channel height of 2 cm and a width of 40 cm, the corresponding mass flow rate is 5.6 g/s, which is comparable to the flow rates studied experimentally by Heimerdinger et. al.[10] and numerically by Niewood[27]. The total enthalpy at the inlet is set equal to

$$H_{t0} = \frac{\gamma p}{(\gamma - 1)\rho} + \frac{1}{2}u^2 + \alpha \frac{E_i}{m_a} \tag{3.23}$$

and the ionization fraction is fixed at some small value at each of the inlet points, typically 1×10^{-3}. This model cannot accomodate a zero ionization fraction, which would normally be expected as an inlet condition of the flow, so some small nonzero α must be specified. Previous one-dimensional numerical research, however, has shown that as long as the specified inlet ionization fraction is small, the effect on the overall solution is minimal[27].

Given the above parameters and information from the next inside grid point, all conditions at the inlet may be calculated. The inlet electron temperature is set equal to that of the next inside point. The density is obtained from a quasi one-dimensional downwind finite difference approximation to the overall continuity equation, and the axial velocity and gas temperature are then found from the specified mass flow rate and enthalpy, respectively. The inlet electron density and the species pressures are subsequently known,

and the electron velocities are calculated from the current density relations (Eqn. 2.80). These equations are actually used to calculate the electron velocities at every grid point as a post-processing task; u_e and v_e are not needed in the simplified channel model. The inlet magnetic field is assumed constant and equal to a value consistent with the total applied current of the accelerator:

$$B_0 = \frac{\mu_0 I}{D} \tag{3.24}$$

Outlet

The boundary conditions at the outlet of the channel depend on whether the exit flow is subsonic or supersonic. In both cases the electron temperature is set equal to that of the next inside point and the magnetic field is fixed at zero. In reality, the magnetic field at the exit plane is zero only at the electrodes, and extends beyond the outlet in the interior of the flow. This results in additional Joule heating and fluid acceleration beyond the accelerator structure. Although the computer code has the capability to model this phenomenon, because the applied magnetic field taken from the solution of the analogous one-dimensional problem is not specified beyond the exit, it is not explicitly modeled at this stage in the research. It is assumed that since the total energy input is nevertheless taken into account in the current state of the model, the overall error in the calculated exit flow solution will not be serious, and the effect on the solution far from the outlet will be minimal. If the magnetic field equation were integrated along with the other governing equations of MPD channel flow to produce a fully two-dimensional solution, then it would be much more desirable to more accurately model this exit phenomenon.

If the flow is supersonic at a point on the exit plane, then the remaining quantities are set equal to their values at the next inside grid point, with the exception of the pressure and the heavy species temperature. The pressure is given by

$$p_I = p^T_{I-1} = p_{I-1} + \frac{B^2_{I-1}}{2\mu_0} \tag{3.25}$$

after Niewood[27], and the heavy species temperature is then determined by the other known quantities. If the flow is subsonic, then the exit pressure is set equal to some small value (typically less than 100 Pa), and the density and axial velocity are given by the Riemann invariants

$$\rho_I = \left(\frac{p^T_I}{p^T_{I-1}}\right)^{\frac{1}{\gamma}} \rho_{I-1} \tag{3.26}$$

$$u_I = u_{I-1} + \frac{2}{\gamma - 1}(a_{I-1} - a_I) \tag{3.27}$$

In general, the prescence of the magnetic field through Lorentz acceleration of the ionized gas renders simple invariant theory inapplicable, and it is not in fact utilized at the inlet. At the outlet, however, the value of the magnetic field is nearly zero, so that the use of Riemann invariants at the exit boundary introduces minimal additional error to the solution. The remaining quantities at a subsonic outlet are then calculated as in the supersonic case.

Electrode Walls

At the electrode walls viscous no-slip conditions are imposed on the axial and transverse fluid velocities ($u = 0$, $v = 0$). The electron temperature is set equal to that of the next inside grid point, and the heavy species temperature is held constant at 500°K. It is assumed that the gas temperature at the walls is substantially lower than the melting point of the electrode material, and constant along the length of the channel due to good conduction within the metallic electrodes. A higher wall temperature of 1000°K was considered, which is compatible with electrodes composed of high-temperature metals such as Tungsten or lower-temperature metals such as Copper alloyed with Nickel, Titanium, Molybdenum, or similar materials. Since the gas temperature is significantly higher in the interior region of the channel, this higher wall value would lessen the steep temperature gradients near the electrodes, and consequently reduce the flux of energy lost to the walls through conduction and alleviate potential computational problems in this region. It was determined, however, that the value of the wall gas temperature has a minimal effect on the flow, especially far from the wall boundaries. In addition, for simplicity the inlet gas temperature is set equal to that of the electrode walls, and a lower temperature at the inlet is more desirable in order to more realistically model the state of the incoming gas and to more closely match boundary conditions to those used in previous comparable numerical simulations.

A fully two-dimensional calculation would require complex electrode boundary conditions on the magnetic field, but since this research assumes a static, applied magnetic field, no such conditions are necessary. In addition, the transverse overall momentum equation at the walls reduces to the familiar condition $\frac{dP}{dy}|_{wall} = 0$, with the modification

that here P is the sum of the fluid and magnetic pressures, so that

$$\frac{d\left(p+\frac{B^2}{2\mu_0}\right)}{dy}|_{wall}=0 \tag{3.28}$$

For the boundary condition on electron density at each electrode, a balance is postulated between the flux of ions arriving at the wall by ambipolar diffusion, and the flux of ions arriving by virtue of their thermal energy at the Bohm velocity (v_B):

$$D_a\frac{dn_e}{dy}=n_e v_B \tag{3.29}$$

where

$$v_B=\sqrt{\frac{k\left(T_e+T_g\right)}{m_a}} \tag{3.30}$$

The Bohm velocity is derived by assuming that at the edge of the plasma sheath located on each electrode, the ion velocity is limited by an electrostatically choked flow condition beyond which the ions free-fall collisionlessly through the sheath to the wall[8]. This boundary condition neglects the internal effects of plasma sheaths and the voltage drops which are present there, typically on the order of 10V. Also omitted is any treatment of the thermionic emission of electrons which occurs at the "hot" regions of the cathode. Introducing additional modeling to account for these phenomena would add another iterative level to the already complex and time-consuming set of governing equations for this model. Therefore it is assumed that the simpler treatment is at least sufficient to provide reasonable solutions to the flow away from the electrode walls. Given the above conditions, the remaining flow quantities can be determined at each electrode.

3.4.3 Initial Conditions

The initial conditions are chosen as a first approximation to the steady-state solution of the problem. Distributions of the current density and electron velocity are given by the specified magnetic field distribution. The electron temperature is set at a constant value over the mesh, while the transverse velocity is everywhere set equal to zero. The axial velocity, gas temperature, and ionization fraction are defined as linearly increasing functions in the axial direction with parabolic transverse distributions. Density is calculated by assuming no variation in the transverse direction, and enforcing the correct mass flow rate at each axial location in the channel.

3.4.4 Procedure

Once the initial conditions of the flow have been specified, the solution is calculated numerically as follows. First, the time steps are calculated at all grid points in each direction from stability criteria. The most restrictive axial time step is chosen as the time interval for the current integration step. Next, the fast terms in the electron density and energy equations are integrated based on their individual stability restrictions. These terms, including the flux terms in the energy equation and the ambipolar diffusion term in the density equation, are manipulated separately because their stability-restricted time steps are significantly smaller than those of the other terms in the governing equations. Removing these terms and performing the integration separately while holding the other variables constant allows the overall time restriction on the governing equations to be relaxed, thus saving computational time. The next step is to integrate the governing equations using Time-Split MacCormack's Method. During each predictor and corrector step the fluxes, damping terms, and source terms are calculated, and the boundary conditions are updated. Once the time step integration has been completed, the time counter is updated and the error is estimated by calculating the root mean square changes in heavy species pressure, electron pressure, and total pressure over the mesh. The system of equations is repeatedly integrated until either a specified number of iterations has been reached or the solution is considered converged. Computations were performed on both a VAX 3200 computer under the VMS V5.2 operating system, and a CRAY Y-MP/832 supercomputer under UNICOS V5.0.

Chapter 4
Results

4.1 Flow Results: Baseline Case

Parameters of the baseline case are listed in Table 4.1. A useful non-dimensional parameter in magnetogasdynamics is the magnetic Reynolds number, R_B. This parameter is analogous to the familiar fluid Reynolds number, and represents the ratio of magnetic convection to magnetic diffusion. When $R_B \approx 1$, these two processes are of comparable order, while for $R_B \gg 1$ magnetic convection dominates. The magnetic Reynolds number is given by

$$R_B = \mu_0 \sigma u_{ref} L \tag{4.1}$$

where

$$u_{ref} = \frac{B_0^2 A^*}{2\mu_0 \dot{m}} \tag{4.2}$$

$Channel Length(L) = 0.1m$	$Total Current(I) = 31.83kA$
$Channel Height(H) = 0.02m$	$B_0 = 0.1Tesla$
$Channel Depth(D) = 0.4m$	$\dot{m} = 5.6g/s$
$Inlet Gas Temp. = 500^oK$	$Wall Gas Temp. = 500^oK$
$Working Fluid = Argon$	$R_B \approx 2.5$

Table 4.1: Parameters for Baseline Case

Using the parameters of the baseline case, this implies that $R_B = 0.001\sigma$. Results to be discussed show that for the baseline case, the electrical conductivity varies between $2000 mho/m$ and $3000 mho/m$, so the magnetic Reynolds number is approximately 2.5. Four types of plots are utilized in this section to display results. The first is an axial line plot with three lines - one near or at the upper wall boundary, one at the centerline,

and one near or at the lower wall boundary. This is to quantitatively display the axial variation of the plotted quantity at representative points in the channel. The second is a transverse line plot, employed to quantitatively display the transverse variation of the plotted quantity at a given axial point. The third is a two-dimensional contour plot. This is used to show with some precision the relative variation of the plotted quantity over the computational domain. The fourth is a three-dimensional perspective plot, which graphs the plotted quantity as a function of both x and y. This is the most qualitative of the three types of plots, but is important in that it shows the value of the plotted quantity at every point on the computational grid. Axial line plots will be presented for every flow variable, while transverse, contour, and perspective plots will be reserved for those cases in which they will be most elucidating. Since the magnetic field has been constrained to vary in the axial direction only and the transport properties are assumed to be isotropic, the solution is symmetric about the channel centerline.

4.1.1 Flow Variables

Figures 4.1 and 4.2 show the magnetic field distribution used for the baseline case. The magnetic field is seen to vary only in the axial direction, by construction, and is roughly linear except for concentrations in the regions of the inlet and outlet. As the magnetic Reynolds number increases these concentrations become more marked, causing nearly all of the energy deposition and fluid acceleration to occur within thin layers at the entrance and exit of the channel. The following pair of figures illustrate the current density distribution over the channel. Through Maxwell's magnetic field curl relation, since the magnetic field varies only in the axial direction, the current density does so as well. Because the magnitude of $\frac{\partial B}{\partial x}$ is greater at the inlet and outlet than in the interior of the channel, the value of the current density is higher in these regions.

A line plot of the fluid pressure is shown in Figure 4.5. After an initial large decrease in a very thin layer at the inlet, the pressure is seen to slowly increase in the mid-channel region as the gas is heated and ionization occurs. At the outlet a steep adverse pressure gradient is formed due to the large energy deposition by Ohmic heating there, as a result of the local current density maximum. Small standing pressure waves are evident in the line plot as well as the perspective plot of Figure 4.6. In the perspective plot the channel entrance is to the lower left of the figure, while the exit is located at the upper right.

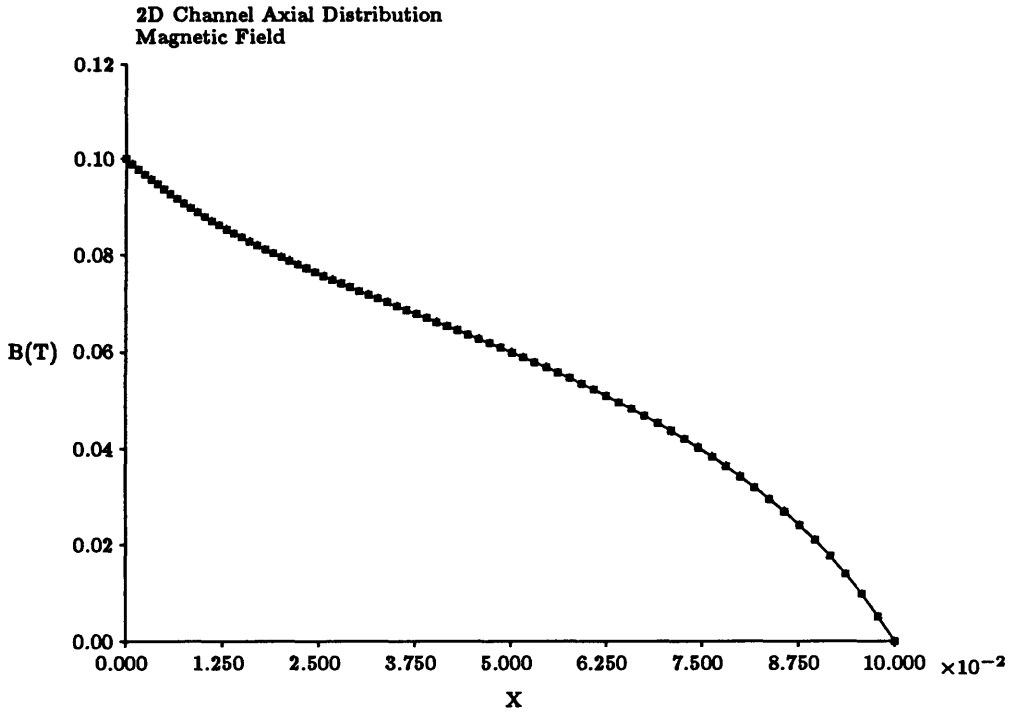

Figure 4.1: Magnetic Field: Baseline Case

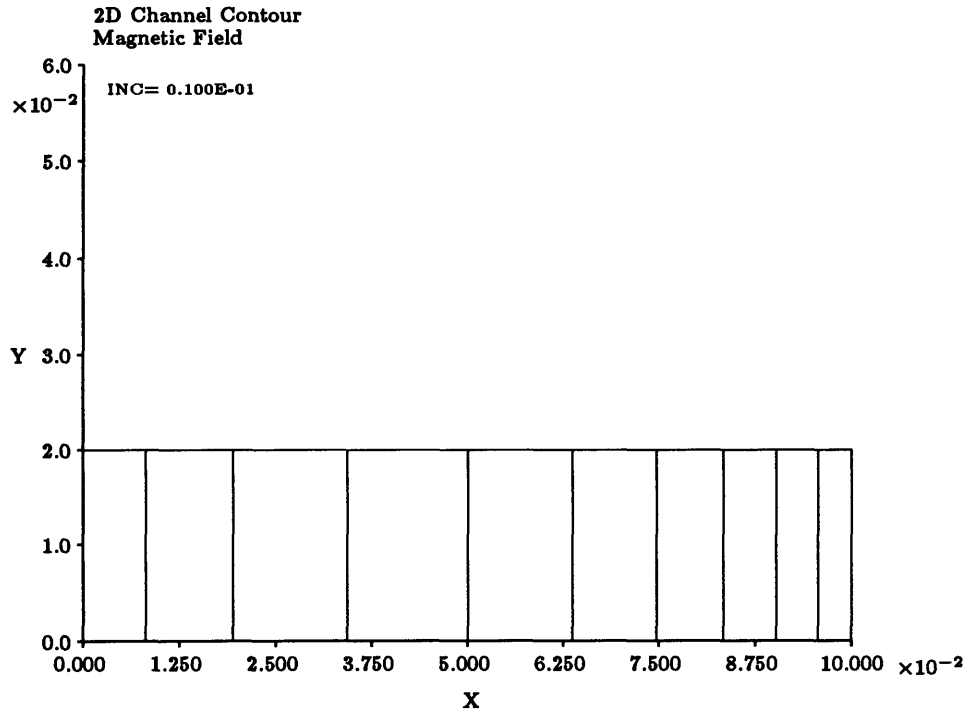

Figure 4.2: Magnetic Field Channel Contours

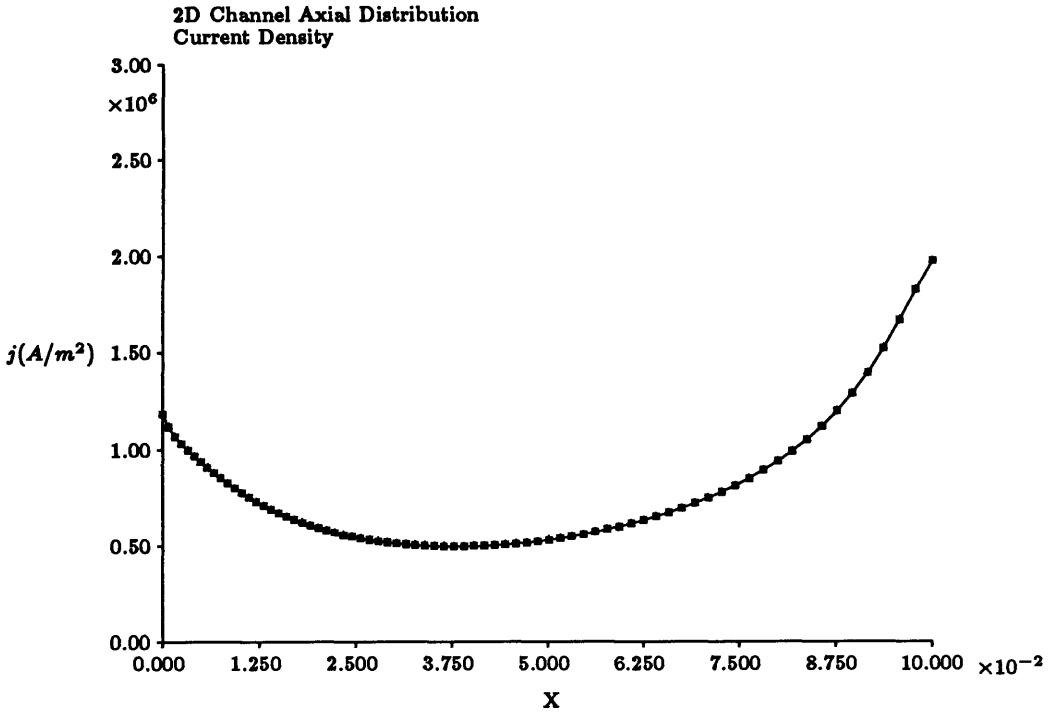

Figure 4.3: Current Density: Baseline Case

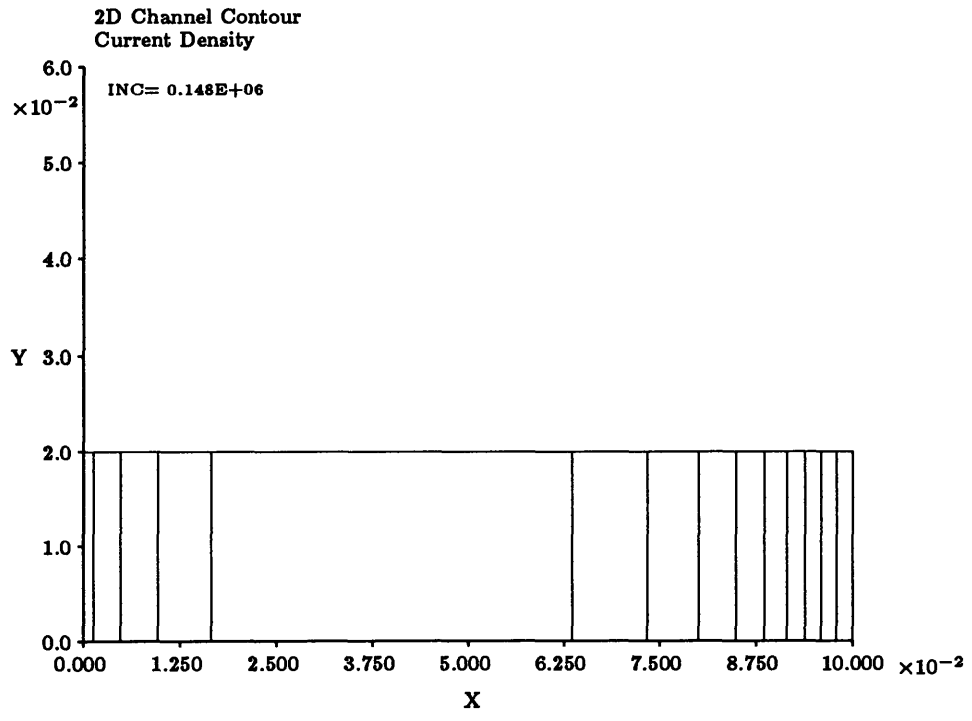

Figure 4.4: Current Density Channel Contours

These waves originate near the electrode walls at the channel entrance, and propagate down the length of the channel with periodic reflections from the downstream boundaries. The source of these waves is twofold.

First, the quasi one-dimensional mass flow boundary condition at the inlet is an over-simplification of the physical situation; it was necessary at this point in order to obtain a solution, because much further work would be required to accurately formulate the inlet conditions. One might, for example, derive the Riemann invariant conditions including the effects of the magnetic field, and use a modified backward traveling characteristic wave to obtain information from the next inside point. The inlet boundary condition may also be nonphysical because the density and gas temperature may have deviated from constant injection profiles by the inlet point, perhaps through some very thin region just beyond the injection point of the propellant. The current formulation of the inlet boundary conditions, however, does guarantee constant pressure over the channel cross-section for the inlet point, a condition which was not observed with other boundary condition methods. Since the magnitude of the transverse velocity is small and there is no transverse variation in the magnetic field, constant pressure across the channel would be expected.

The second source of pressure waves at the channel entrance is that in reality a discontinuity in the electron pressure is present at the first point beyond the inlet, as a consequence of the local current density maximum there. A large amount of energy is imparted to the flow at the first point, which rapidly raises the electron temperature and ionizes the gas. Because the inlet ionization fraction is set to a very small value, however, a large jump in the electron number density occurs in the first grid cell. This is followed by either a much slower rate of increase or a decrease in n_e due to the decreasing level of Ohmic heating as the current density minimum at the half-channel length is approached. Unfortunately, because the numerical smoothing is applied separately to the overall and electron equations based on the electron and heavy species pressures respectively, this large discontinuity in the electron pressure tends to be numerically damped as a function of transverse location. Thus the true physical situation at the inlet is not fully captured. Removing the numerical smoothing entirely from the inlet region does not solve the problem, because the large gradients still create computational difficulties. Therefore a future challenge will be to develop a smoothing procedure which is based on an overall pressure (heavy species pressure plus electron pressure) switch

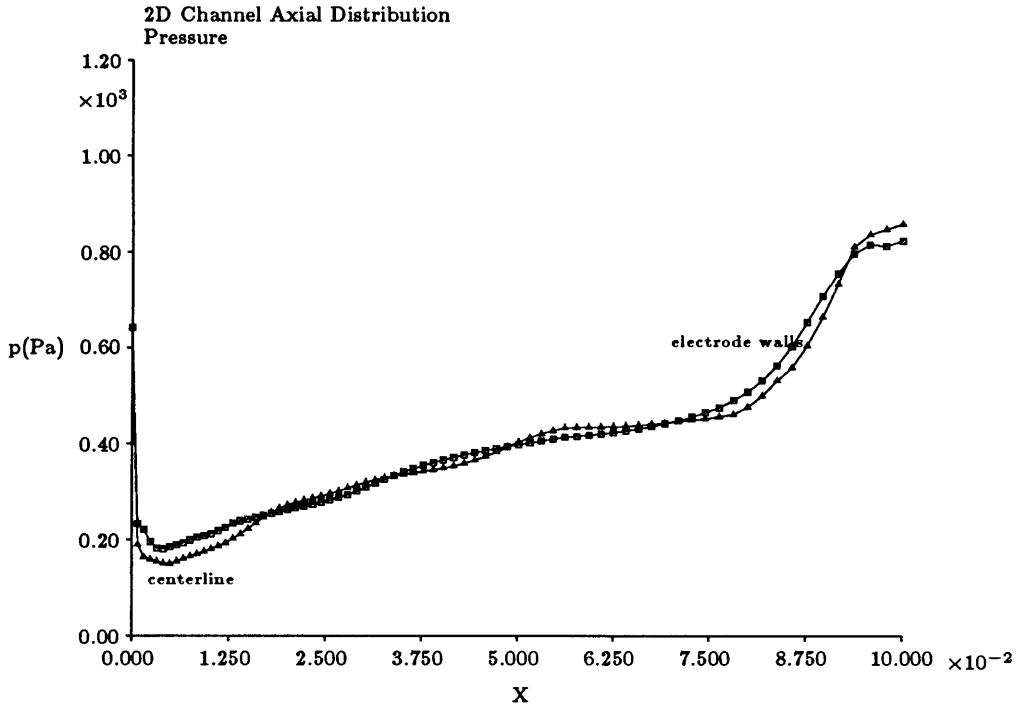

Figure 4.5: Fluid Pressure: Baseline Case

rather than separate switches for each species. The main obstacle in such a formulation is deciding which of the state variables to change in order to maintain a smooth overall pressure profile. Based on the quasi one-dimensional results of Niewood[27], the most likely scenario is that the gas temperature also increases rapidly at the inlet and has a discontinuity at the first grid point. Physically this implies that the quantity of energy deposited in the first cell is too large for the electrons to absorb through heating and ionization within the residence time of that cell, so that the excess energy is collisionally transferred to the heavy species.

A marked drop in the fluid density also occurs within the first grid point, as shown in the line plot of Figure 4.7. The density near the electrode walls is observed to be substantially higher than that in the central region of the channel, as a consequence of the gas temperature gradient and the effect of ambipolar diffusion. Electrons diffusing toward the walls as a result of a strongly decreasing electron density gradient, carry ions with them due to charge coupling. Since the ions, unlike the electrons, cannot pass through the walls, they instead accumulate there. The value of the wall density is dependent upon the combined boundary conditions on the electron and ion densities (Eqns. 3.28, 3.29). Figures 4.8 and 4.9 show transverse fluid and electron density profiles at representative

points in the channel. These graphs illustrate not only the prescence of large gradients near the walls, but also the evolution of these gradients down the channel. The initial shapes of the fluid and electron density profiles produce a local maximum of the quantity $n_e n_n$ a short distance from each electrode wall, thereby creating a local maximum in ionization based on the Hinnov-Hirschberg model (Eqn. 2.28). Consequently, as the flow moves downstream, the electron number density itself develops local maxima near the walls. Ambipolar diffusion to the walls therefore increases, producing a corresponding increase in the wall fluid density gradient.

Figures 4.10 and 4.11 show the fluid velocity for the baseline case. After an initial thin acceleration region through which the flow becomes supersonic, further acceleration primarily by the Lorentz force increases the velocity to approximately 5000 m/s at the exit plane. The rapid development of the velocity boundary layer is evidenced in the contour plot of Figure 4.11; viscous effects reach the centerline by half the channel length. The evolution of the velocity profile is traced in Figure 4.12, which contains normalized graphs between x=0.00 and x=0.07 at intervals of 0.01m. Note that the second profile (x=0.01) is deformed in the center due to lower pressure in the center of the flow near the channel entrance, a result of the aforementioned inlet boundary condition difficulties. Interestingly, the velocity profile evolves to something which is not quite parabolic. Thus, previous quasi one-dimensional work which has assumed parabolic velocity profiles appears to be inaccurate in the early part of the channel because of the boundary layer development region, and in the latter part of the channel because of the non-parabolic character of the developed flow. The Mach number plots in Figures 4.13 and 4.14 show that the flow in fact becomes supersonic by the first grid point. The central core rapidly attains a Mach number of 2, and maintains that value nearly to the exit plane. In this region the acceleration of the gas roughly balances the rate of increase in internal energy due to viscous and collisional heating.

The heavy species temperature is plotted in Figures 4.15, 4.16, and 4.17. As in the previous perspective plot for fluid pressure, the channel inlet is to the lower right of Figure 4.17, while the outlet is to the upper right. Near the inlet, collisional heating from electrons is the dominant process, while viscous dissipation becomes an important heating mechanism near the walls as the flow develops. The effect of viscous heating is the production of temperature maxima located a short distance inside each wall boundary. The location of these maxima is determined by the variation of the viscosity coefficient

and the velocity gradient over the cross-section, and is approximately at the point where the flow velocity is one half of the centerline maximum value. At the exit gas temperatures approach $15,000^{o}K$, and in fact the heavy species begin to transfer energy collisionally to the electrons. This is evident in the contour plot of the electron temperature in Figure 4.19, where T_e is seen to increase near the walls toward the channel outlet. Throughout the channel the electron temperature varies between 0.9 and 1.1 electron volts.

The steepest gradients in the ionization fraction of the gas occur near the inlet and outlet where the Ohmic dissipation is the highest, as shown in the line plot of Figure 4.20. By the end of the channel the ionization fraction reaches a value of 0.55 at the centerline. At the exit the combination of strong dissipation, and high gas temperature and electron density near the walls, creates a high level of ionization over the entire channel cross-section.

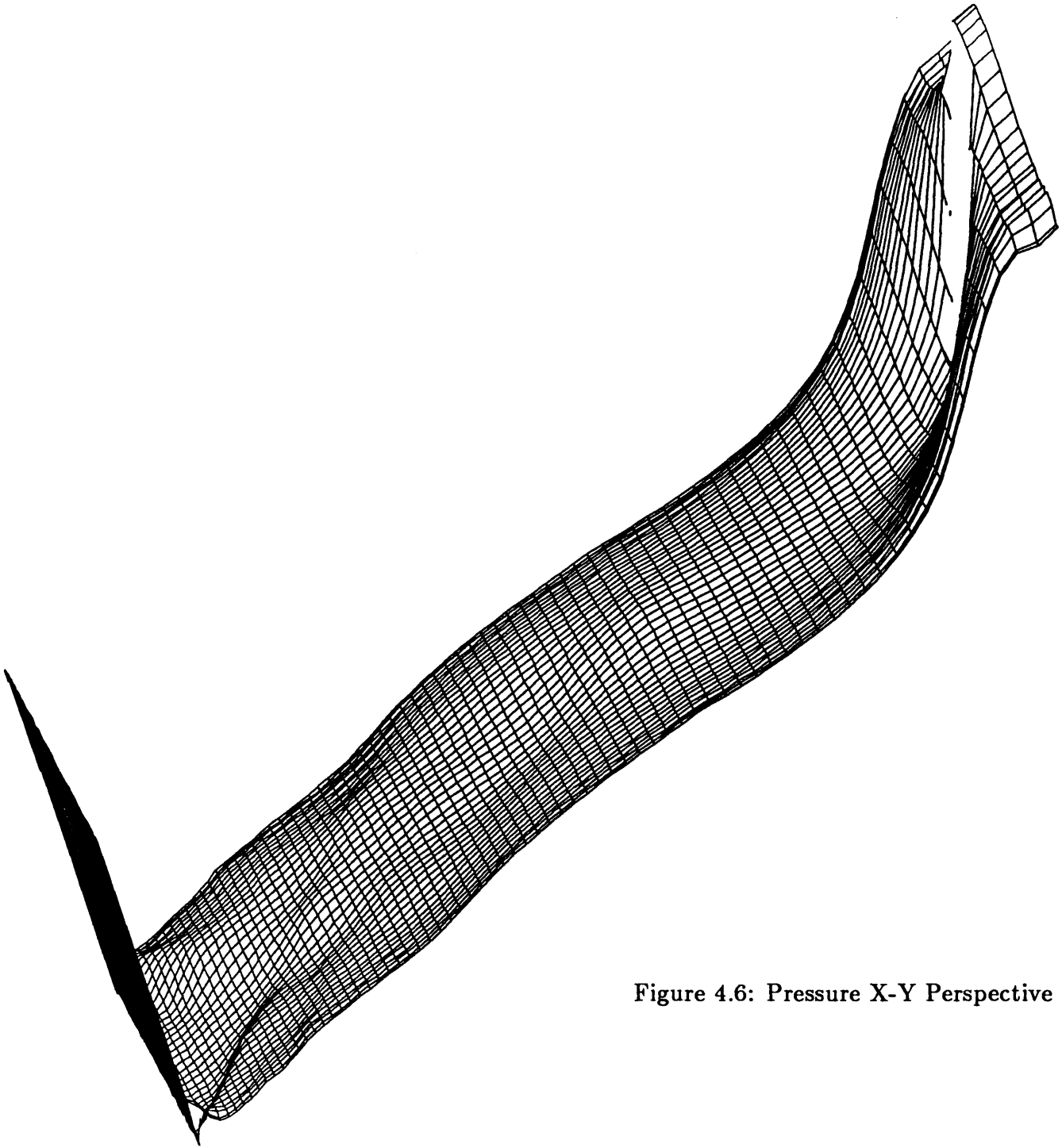

Figure 4.6: Pressure X-Y Perspective Plot

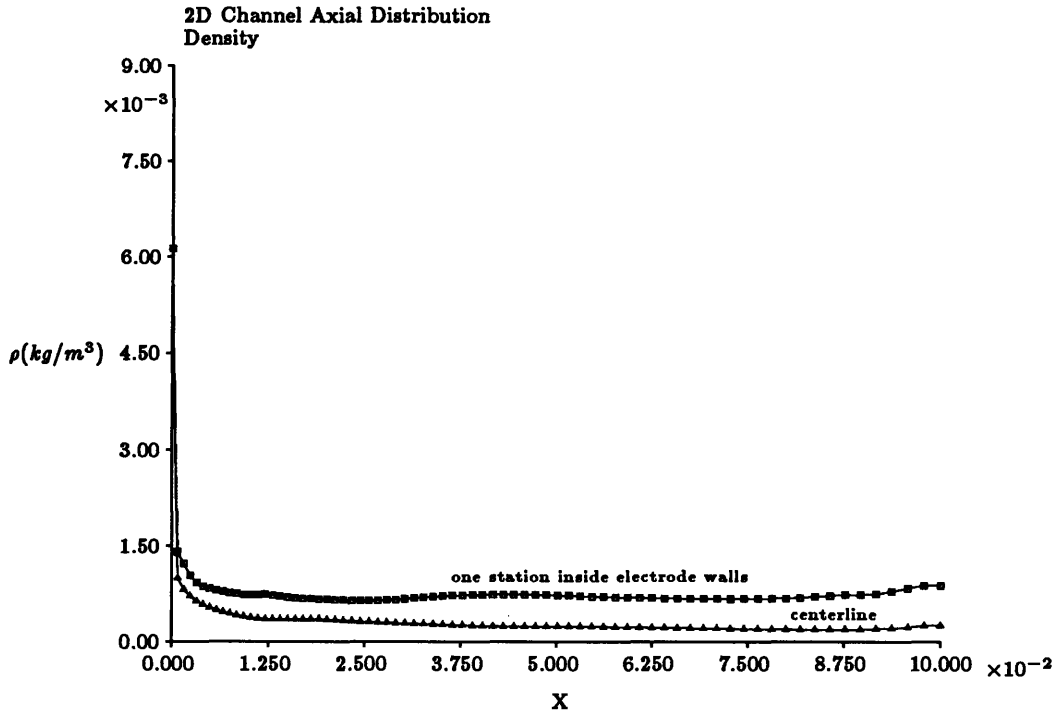

Figure 4.7: Fluid Density: Baseline Case

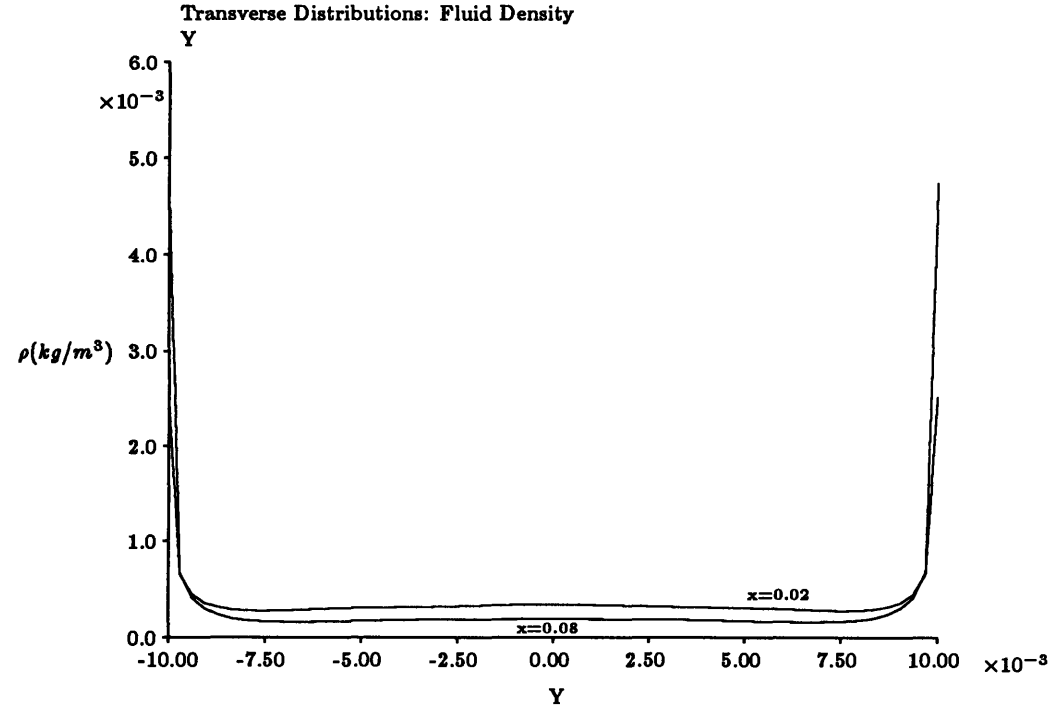

Figure 4.8: Fluid Density Transverse Distributions: x=0.04,0.08

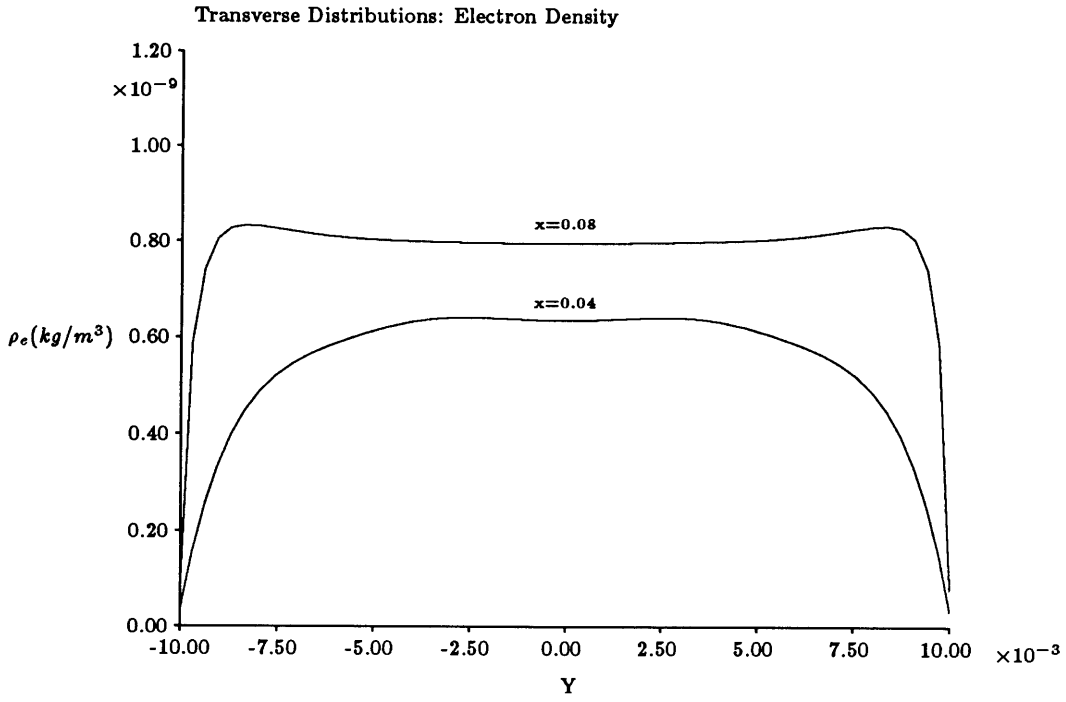

Figure 4.9: Electron Density Transverse Distributions: x=0.04,0.08

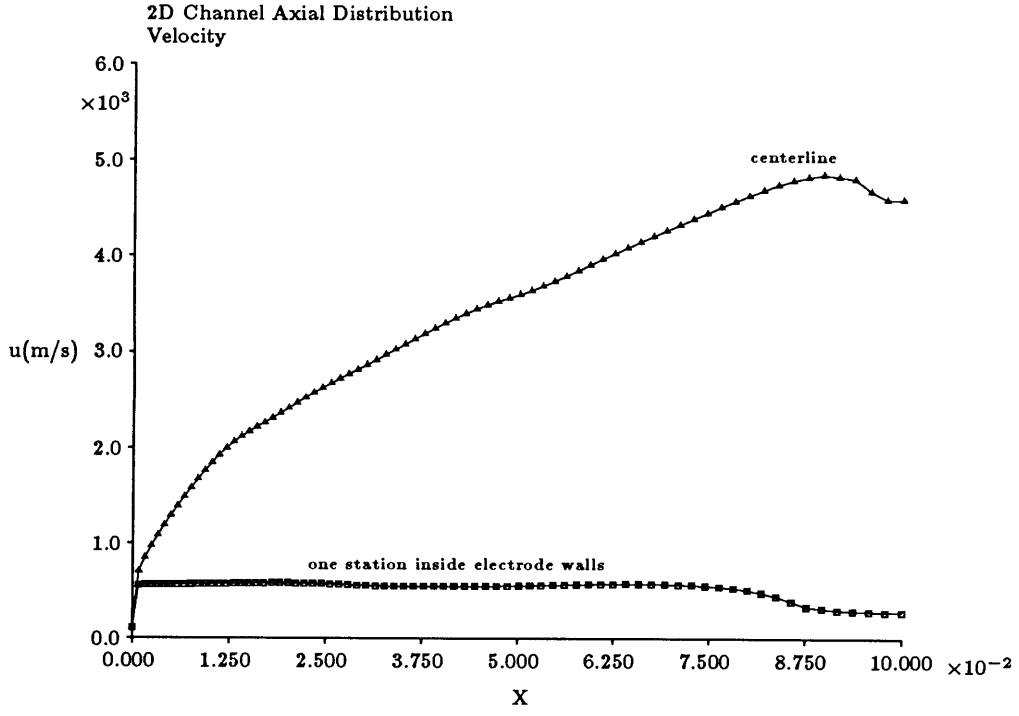

Figure 4.10: Flow Velocity: Baseline Case

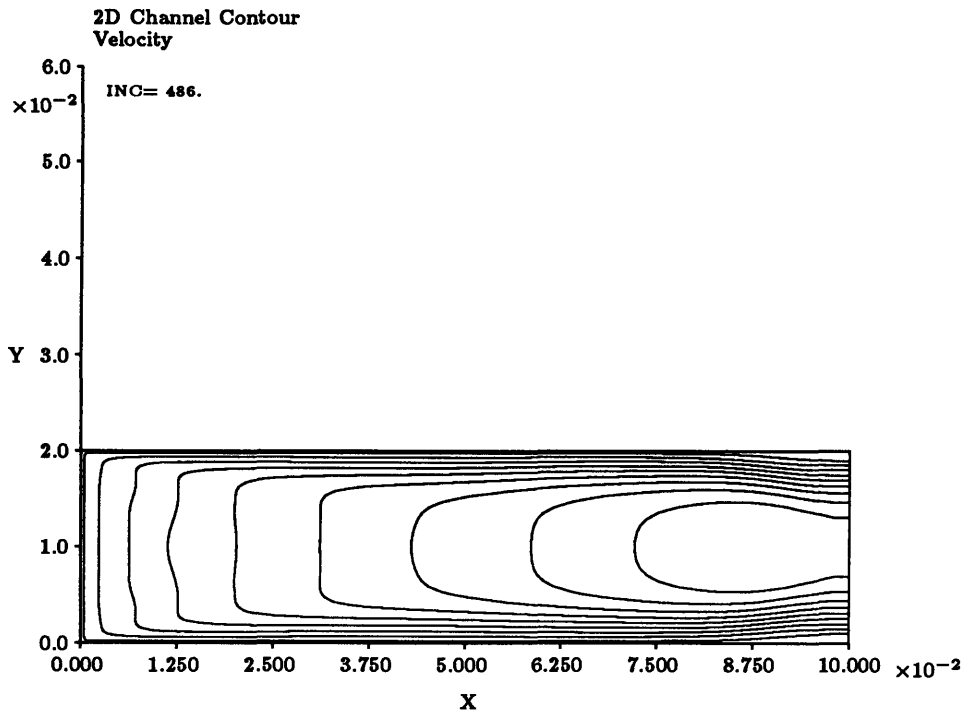

Figure 4.11: Flow Velocity Channel Contours

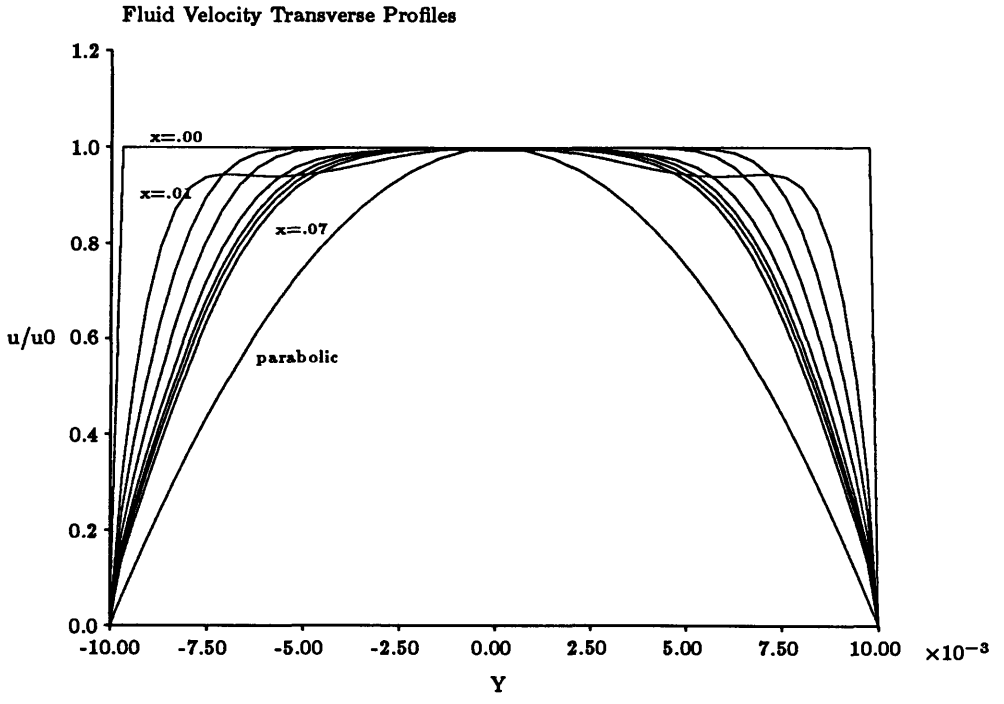

Figure 4.12: Flow Velocity Profile Development

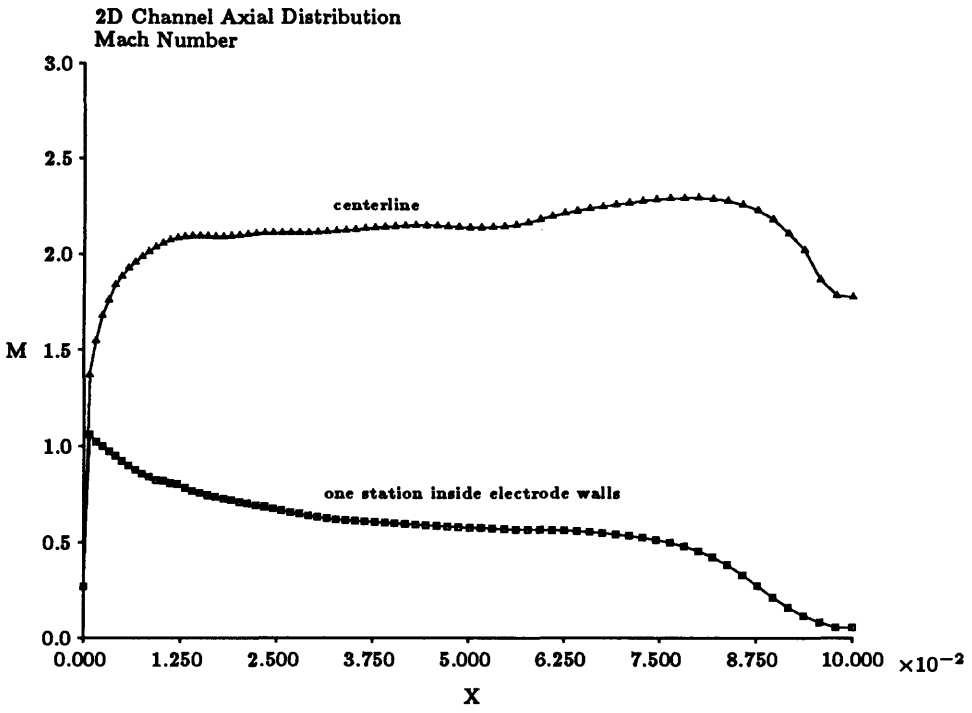

Figure 4.13: Mach Number: Baseline Case

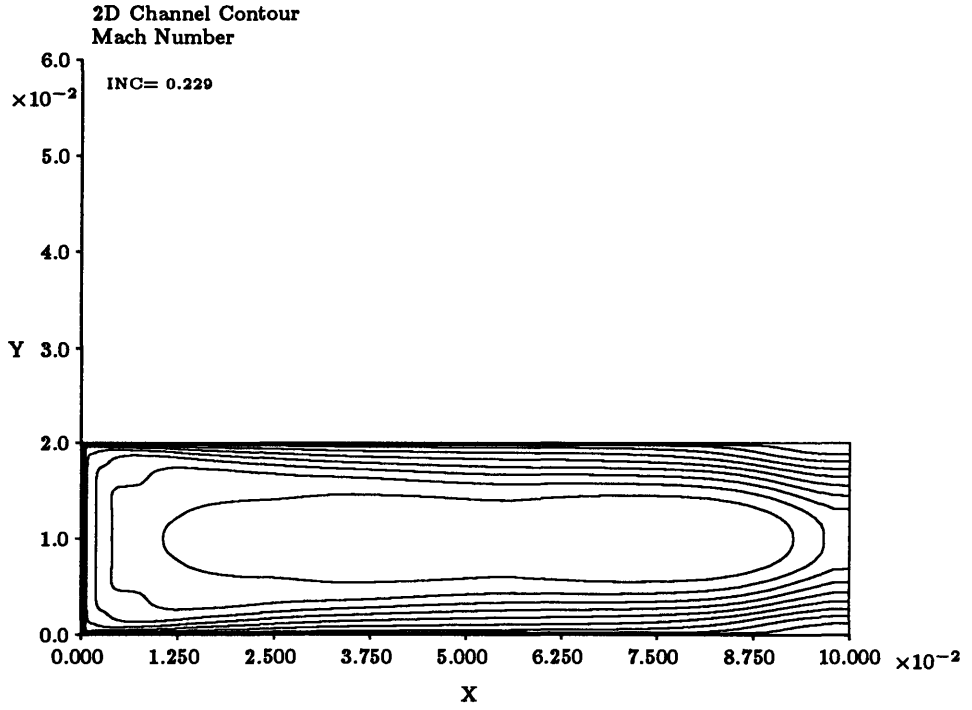

Figure 4.14: Mach Number Channel Contours

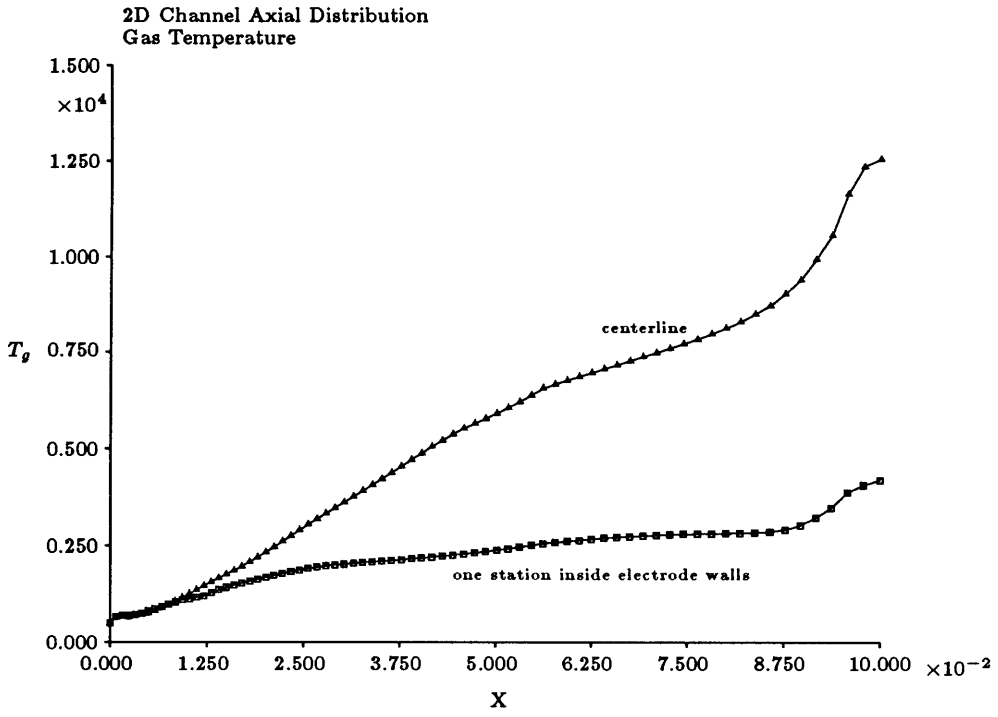

Figure 4.15: Gas Temperature: Baseline Case

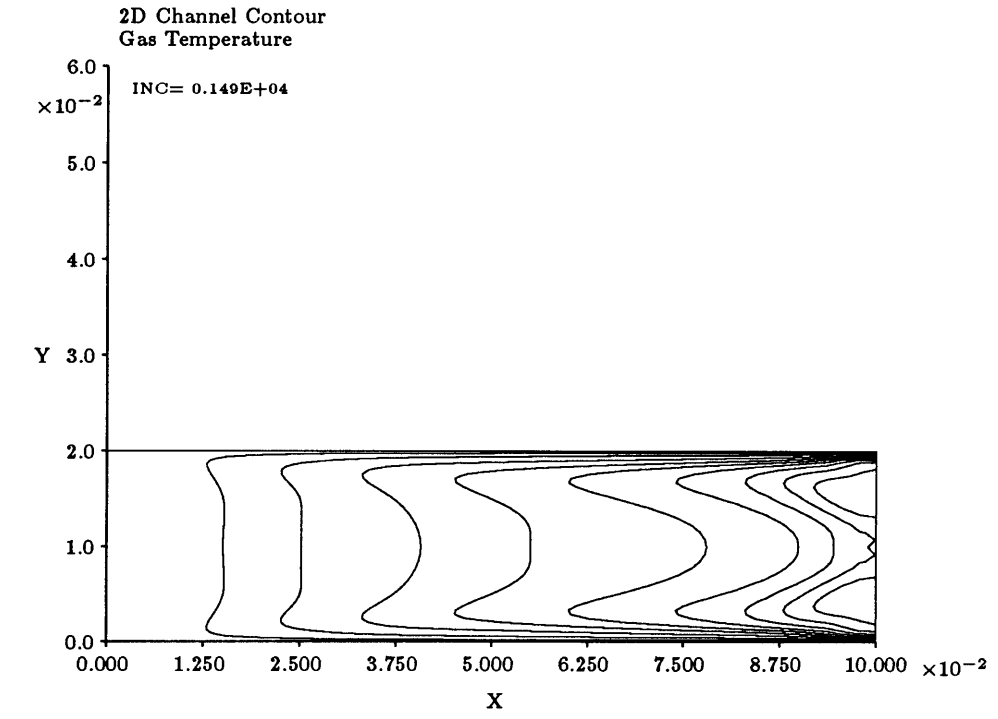

Figure 4.16: Gas Temperature Channel Contours

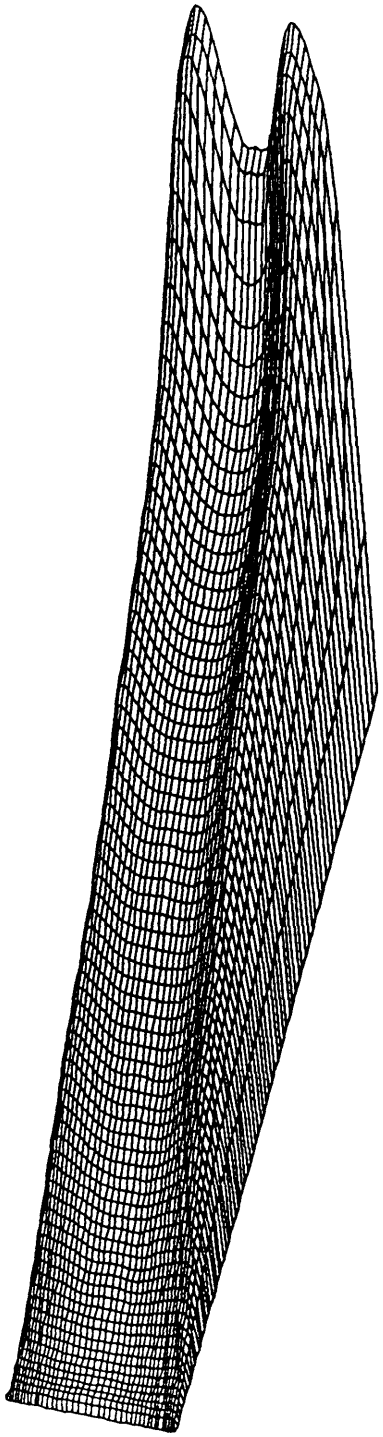

Figure 4.17: Gas Temperature X-Y Perspective Plot

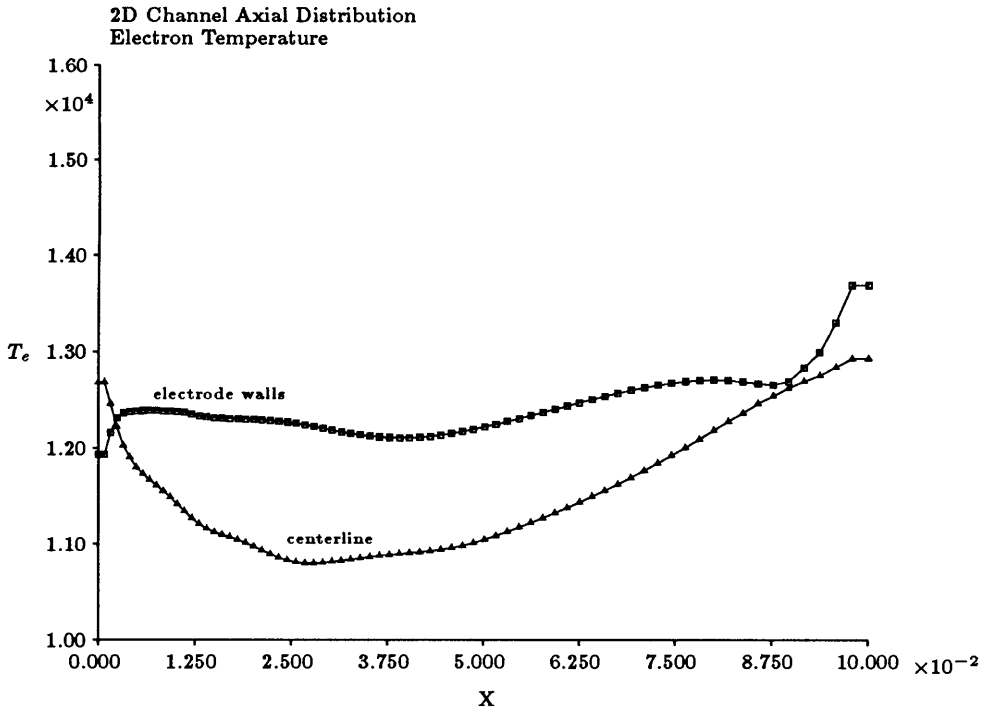

Figure 4.18: Electron Temperature: Baseline Case

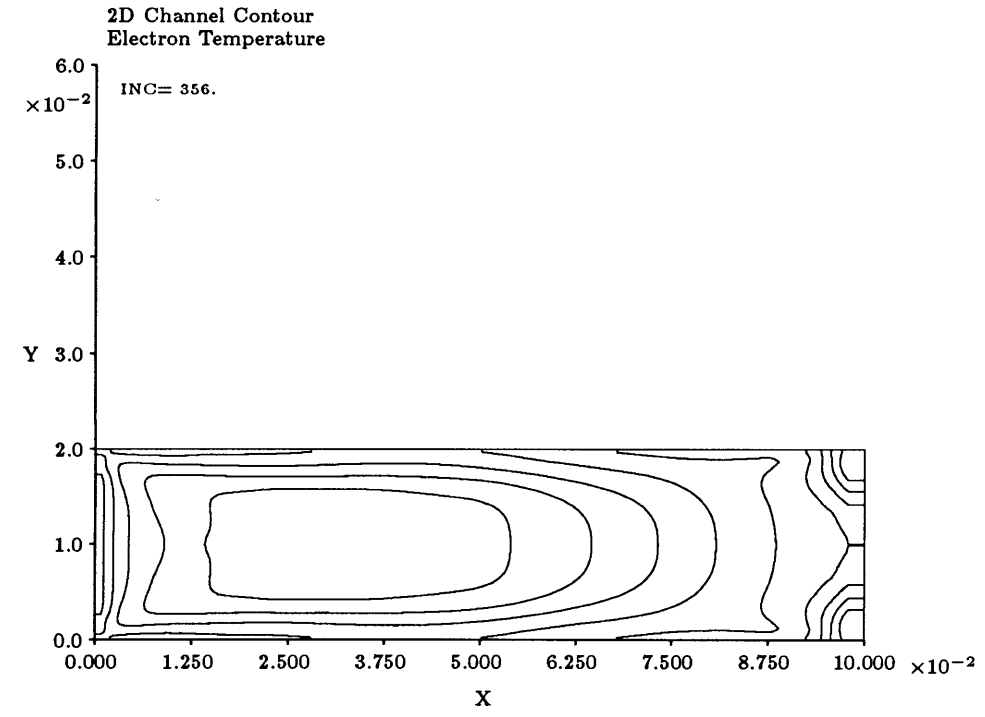

Figure 4.19: Electron Temperature Channel Contours

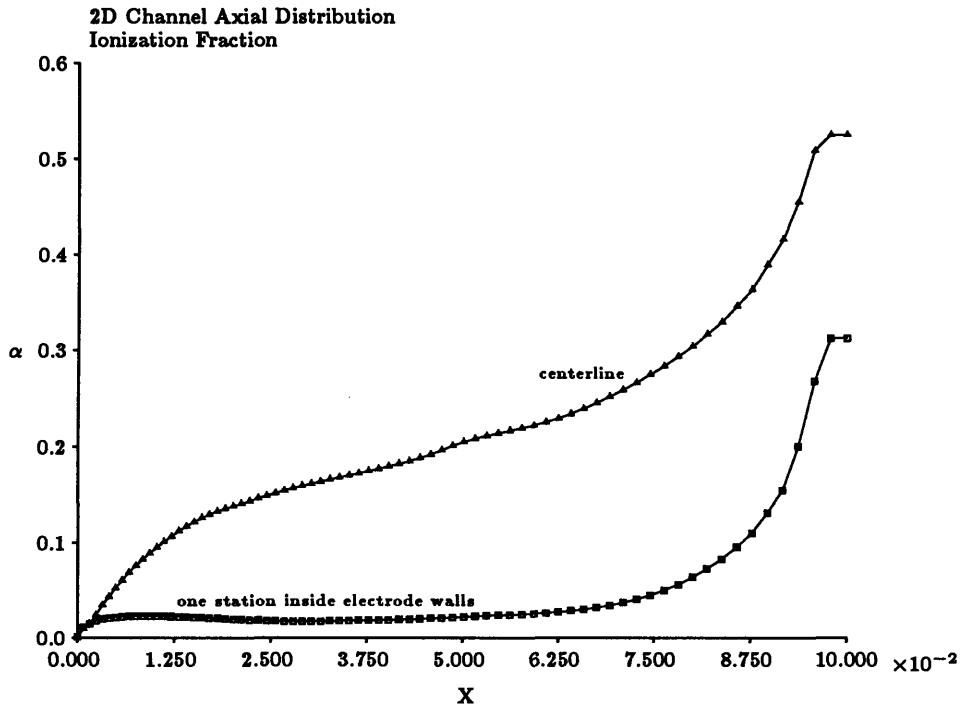

Figure 4.20: Ionization Fraction: Baseline Case

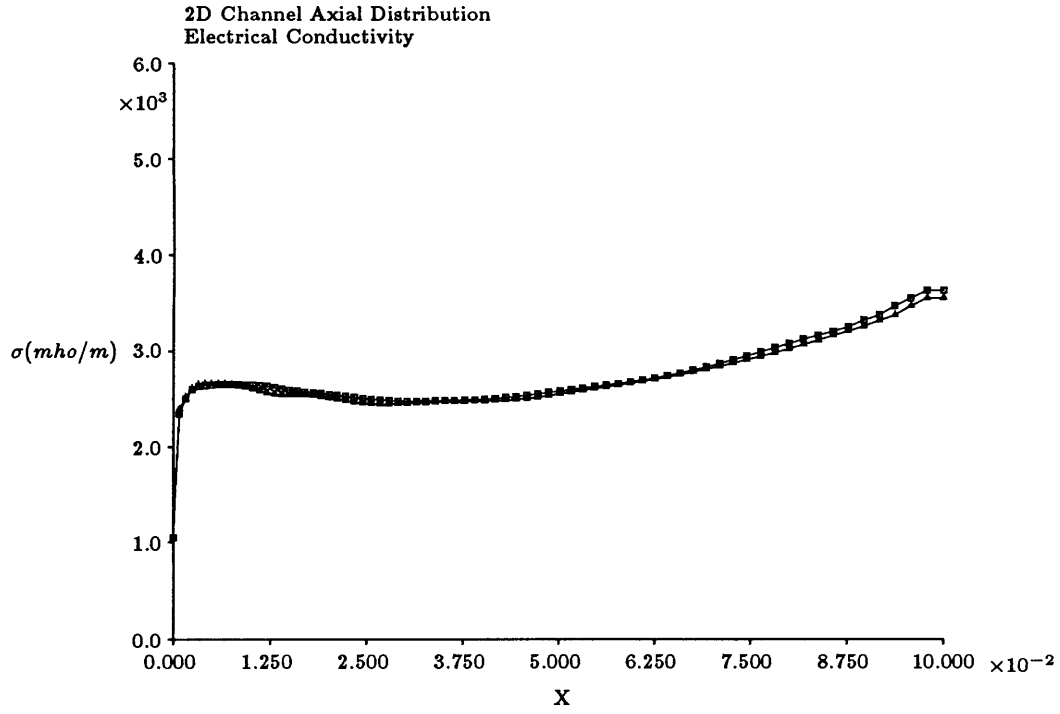

Figure 4.21: Electrical Conductivity: Baseline Case

4.1.2 Transport Properties

The graph of electrical conductivity in Figure 4.21 illustrates an interesting physical aspect of low magnetic Reynolds number MPD flows. This is that the electron density and temperature distributions in the channel are maintained such that the Ohmic dissipation $(\frac{j^2}{\sigma})$ is approximately constant in the transverse direction. Figures 4.22 and 4.23 show the coefficient of viscosity in the channel. A maximum value of μ is achieved at approximately 70% of the channel length near the electrode walls. Upstream of the maximum the fluid viscosity is dominated by the neutral viscosity component, which is relatively large and increases with temperature. Downstream of the maximum, however, the level of ionization increases rapidly and the much lower ion viscosity becomes predominant. Once the viscosity begins to decrease, local minima are attained near the walls at the exit where the gas temperature and electron density are the highest. Comparison to the earlier graph of viscosity coefficient versus temperature (Figure 2.7) shows that the real flow is far from ionizational equilibrium. In the real flow excess ionization leads to a larger population of ions and hence a lower fluid viscosity than in the equilibrium case.

The electron and heavy species thermal conductivity coefficients are plotted in Figures

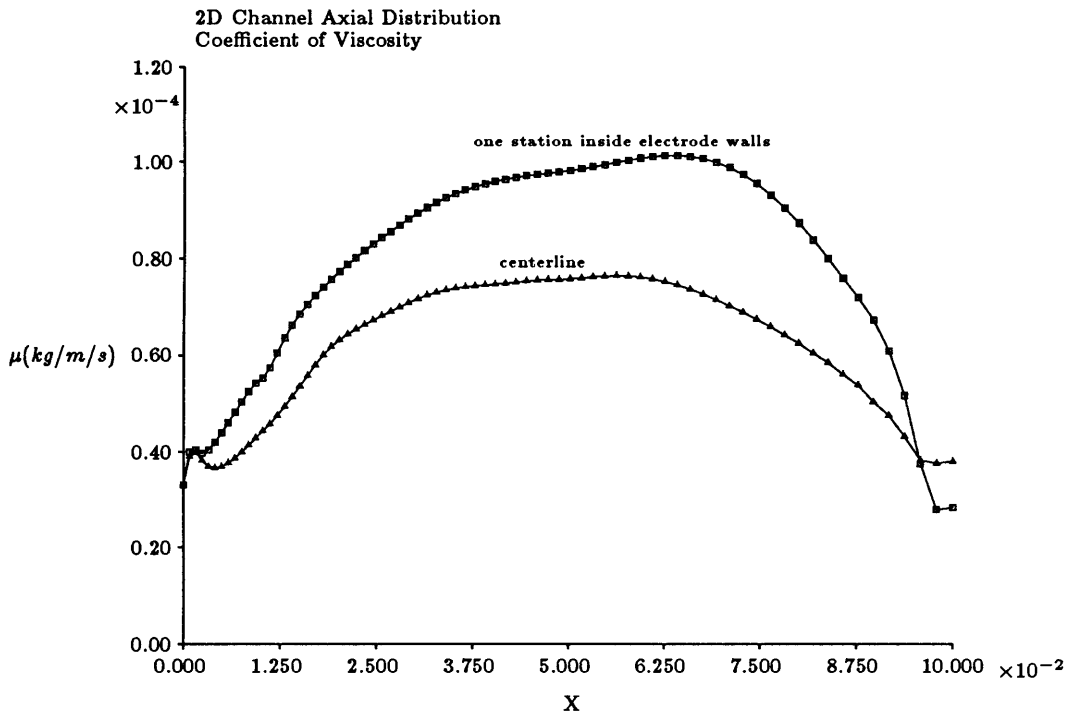

Figure 4.22: Coefficient of Viscosity: Baseline Case

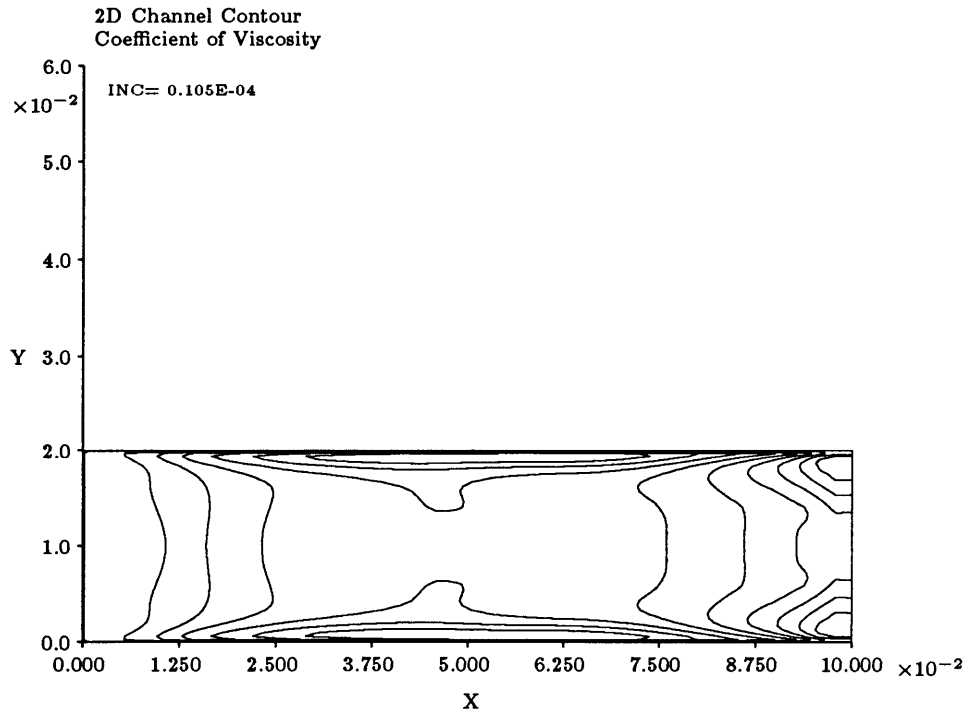

Figure 4.23: Viscosity Coefficient Channel Contours

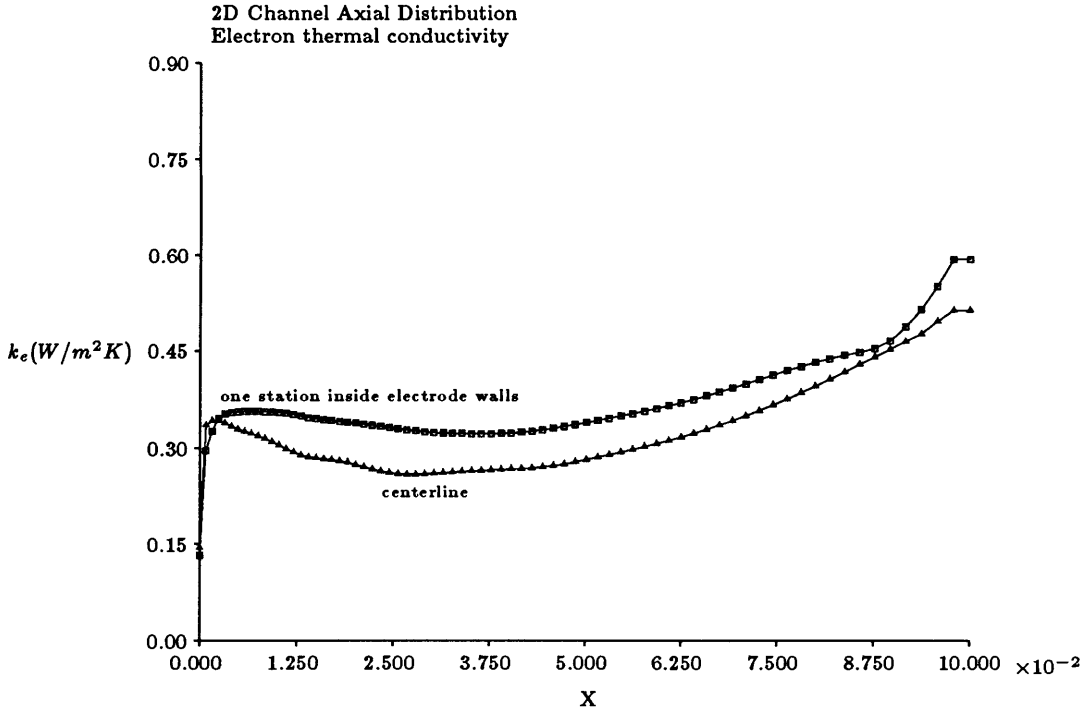

Figure 4.24: Electron Thermal Conductivity Coefficient: Baseline Case

4.24 and 4.25, respectively. The value of k_e is seen to be strongly dependent on electron temperature (refer to Figure 4.18). The value of k_g, like the coefficient of viscosity, decreases once the level of ionization has increased sufficiently, and is considerably lower than its value in Saha equilibrium due to excess ionization.

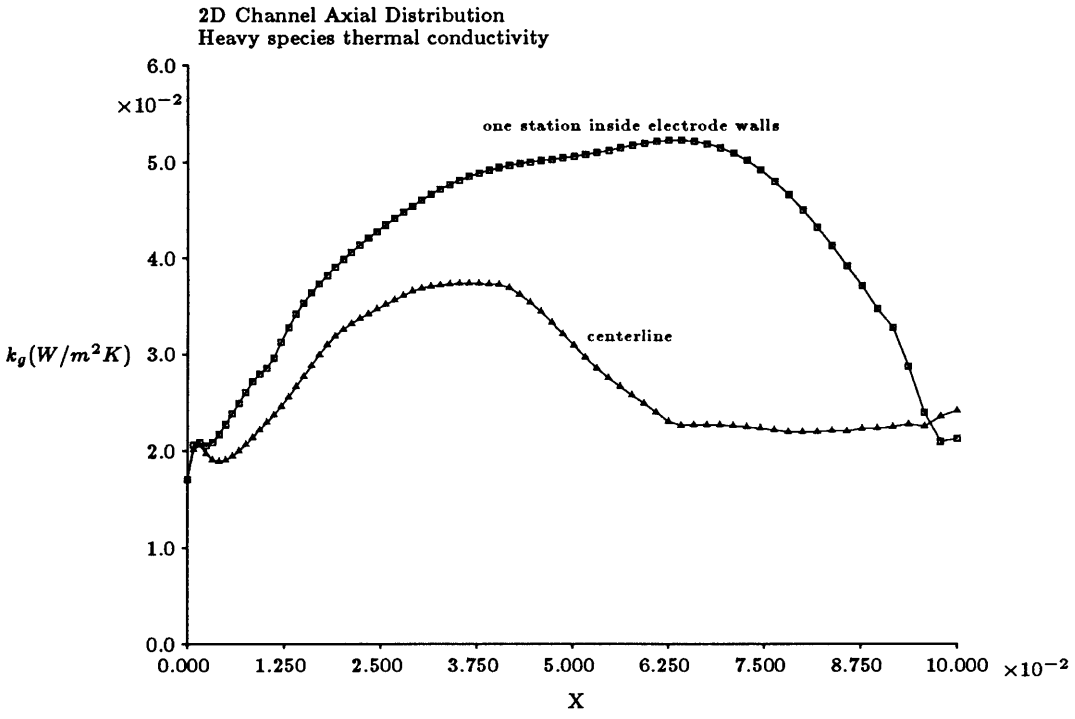

Figure 4.25: Heavy Species Thermal Conductivity Coefficient: Baseline Case

4.2 Relative Importance of Effects

In order to examine the relative importance of the factors involved in energy exchange in the flow, the magnitudes of some terms in the electron and heavy species energy equations are plotted transversely at three representative axial locations in the channel. These axial stations are (1) x=0.01m, chosen to show the energy balance near the inlet where magnetic effects are strongest but the flow is yet undeveloped, (2) x=0.05m, representative of the mid-channel region, and (3) x=0.09m, which is indicative of the outlet region of the channel where maxima in the level of ionization, gas temperature, and Ohmic dissipation occur. Figures 4.26 through 4.28 show the relative sizes of terms in the heavy species energy equation for these locations. Near the inlet the dominant effect is collisional energy transfer from the electrons, because the electron number density is relatively high and there is a large difference between the gas temperature and the electron temperature in this region. Viscous heating and transverse heat conduction are important only very near the electrode walls, since the velocity and thermal boundary layers are not fully developed. Axial heat conduction was found to be negligible in all parts of the channel. By the middle of the channel (Fig. 4.27) viscous dissipation has become dominant in a larger region near the walls, due to the increasing value of the viscosity coefficient and the spread of viscous forces toward the centerline. The lower collisional energy transfer rate results from a somewhat lower electron density in the middle of the channel and an increasing gas temperature, which is $5910^{o}K$ at the centerline, compared to $11,040^{o}K$ for the electrons. Energy is increasingly conducted toward the electrodes, as the increasing gas temperature in the core of the flow produces a steeper temperature gradient near the wall boundaries. Near the exit of the channel collisional energy transfer again becomes the dominant process except in interior regions a short distance from the walls. Very near the walls collisional transfer is high because of high electron density and the difference between T_e and T_g, as is the case to a lesser degree in the central core. At the gas temperature maxima located approximately 0.2cm inside each wall, however, viscous dissipation has heated the heavy species temperature to a value greater than the electron temperature, so that energy is actually transferred from the heavy species to the electrons. Viscous heating is still dominant near the maxima in gas temperature, although it is decreasing as the exit is approached because of the decreasing value of the viscosity coefficient. The transverse heat conduction plot illustrates that heat is also being conducted away from the gas temperature maxima.

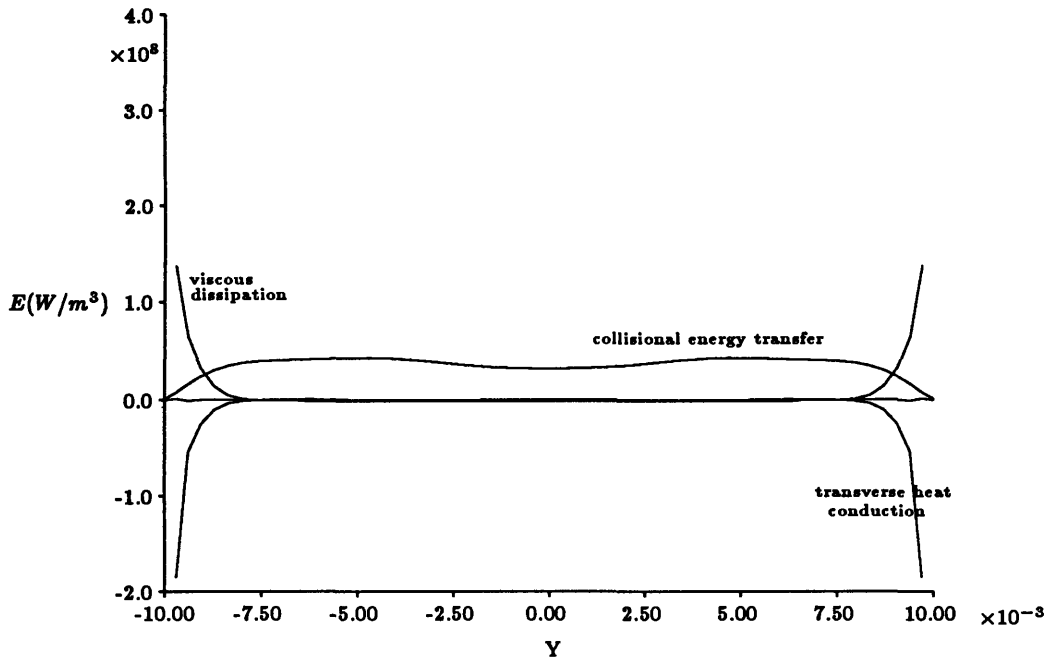

Figure 4.26: Size of Terms in Heavy Species Energy Equation, x=0.01

Graphs of some terms in the electron energy equation are shown in Figures 4.29 through 4.31. Ohmic dissipation is the primary source of energy in all three representative regions, and is naturally higher near the channel inlet and exit. As previously noted, the dissipation is nearly constant over the channel cross-section. Axial heat conduction, as observed with the heavy species, is negligible in the overall energy balance. Transverse heat conduction is important only near the electrode walls, where energy is generally conducted toward the centerline due to the shape of the electron temperature profile. Collisional energy transfer, described in the preceding paragraph, is a relatively important energy loss mechanism depending on the location in the channel. The primary source of energy loss, however, is ionization. This effect is greatest near the wall boundaries, where the ionization rate must be higher in order to replace electrons which are lost through ambipolar diffusion to the walls. The magnitude of terms in the electron energy equation are presented quantitatively in Table 4.3 for the centerline of the channel, at .01m axial intervals. Ionization and recombination rates from the Hinnov-Hirschberg model are similarly presented in Table 4.2. From the table it is apparent that three-body recombination is not important for this baseline case at the centerline of the channel.

Transverse heat conduction to the walls and the ambipolar loss of electrons through

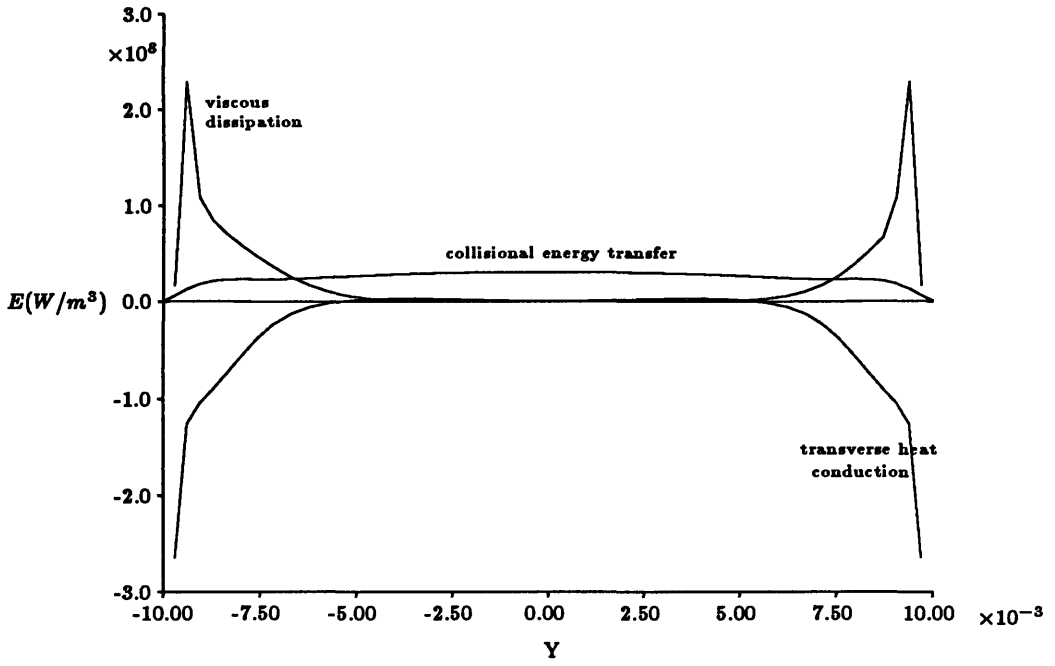

Figure 4.27: Size of Terms in Heavy Species Energy Equation, x=0.01

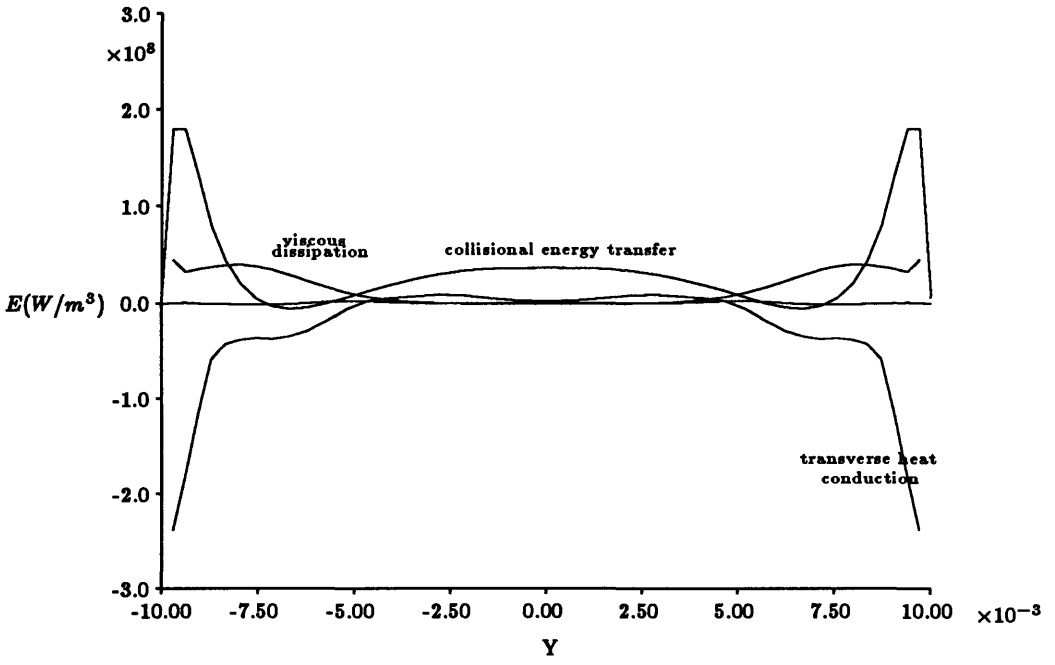

Figure 4.28: Size of Terms in Heavy Species Energy Equation, x=0.09

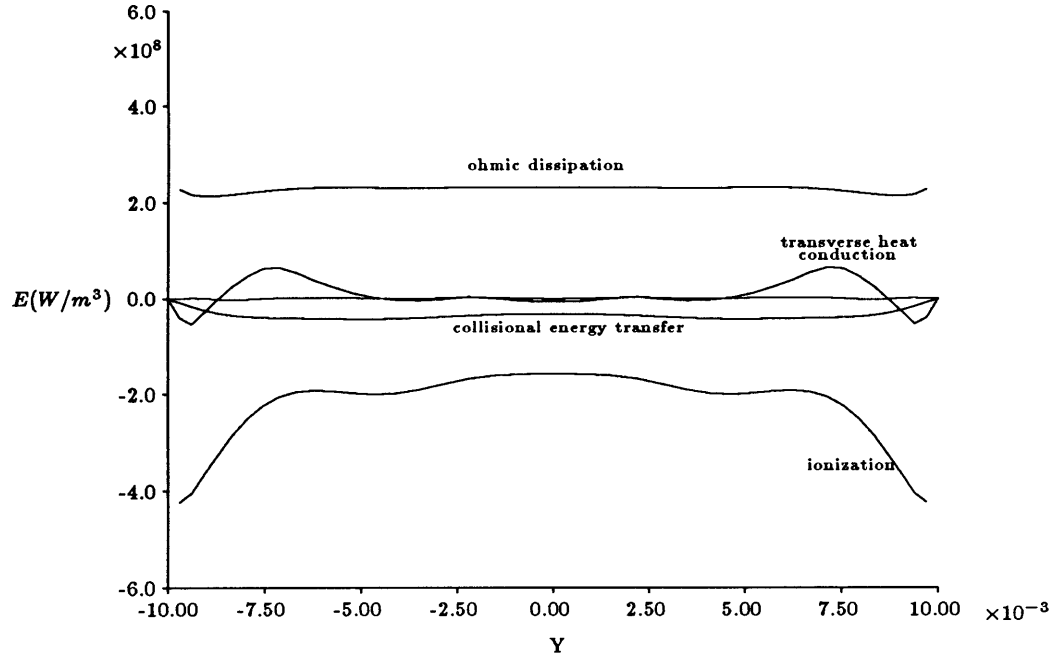

Figure 4.29: Size of Terms in Electron Energy Equation, x=0.01

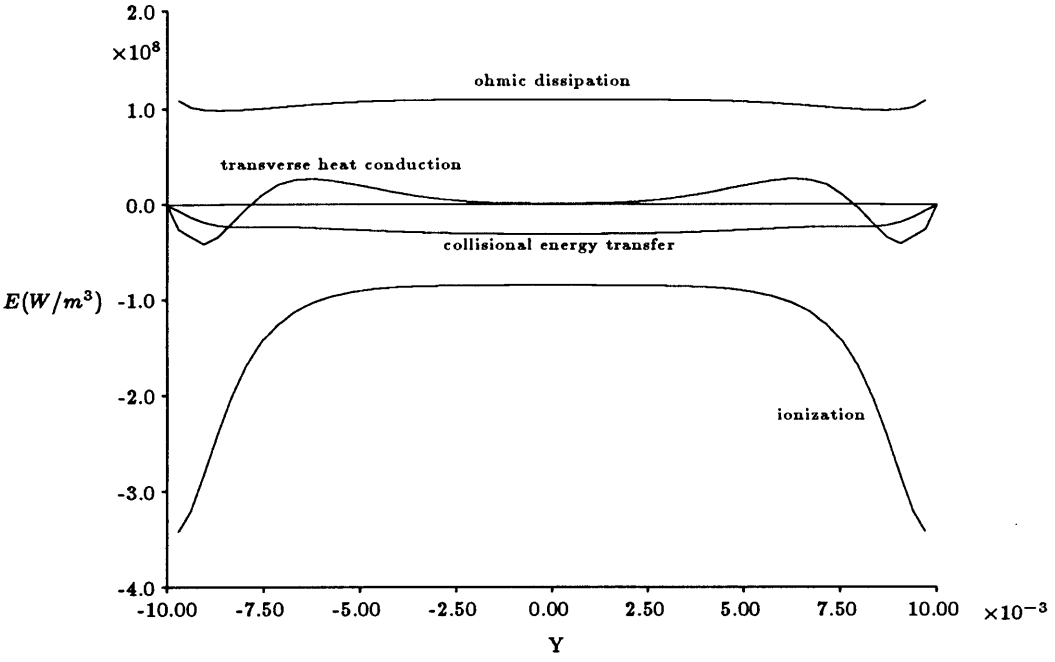

Figure 4.30: Size of Terms in Electron Energy Equation, x=0.05

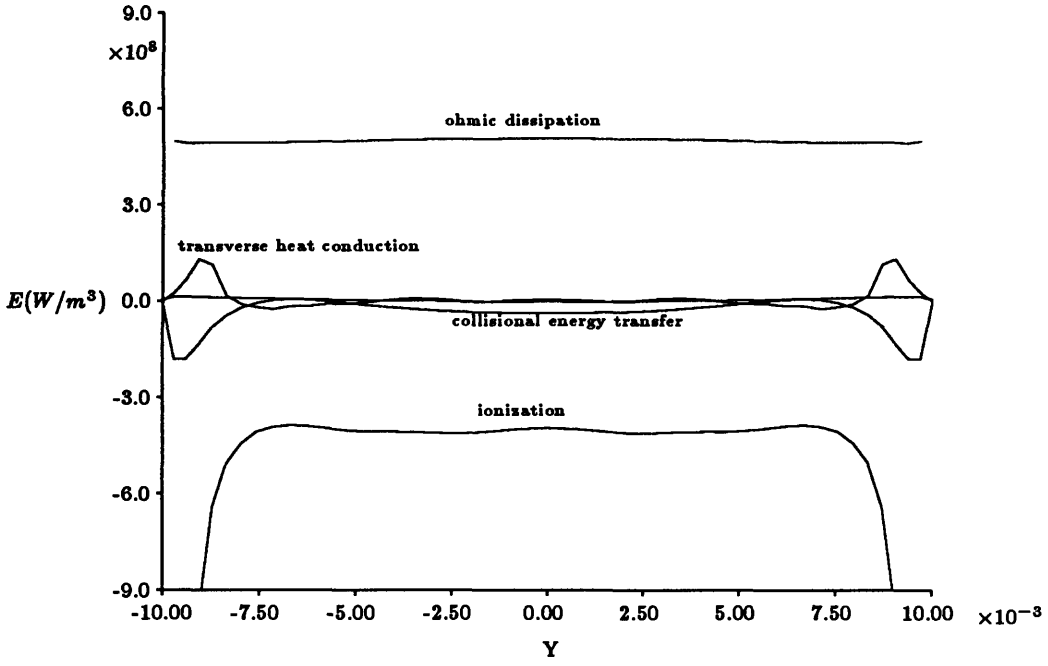

Figure 4.31: Size of Terms in Electron Energy Equation, x=0.09

x(m)	Ionization Rate $(10^{26}/m^3 s)$	Recombination Rate $(10^{26}/m^3 s)$	$\dot{n}_e$ $(10^{26}/m^3 s)$
0.00	1.724	0.000	1.724
0.01	0.616	0.009	0.607
0.02	0.421	0.026	0.395
0.03	0.277	0.026	0.251
0.04	0.247	0.022	0.225
0.05	0.305	0.027	0.278
0.06	0.407	0.027	0.380
0.07	0.565	0.026	0.539
0.08	0.898	0.030	0.868
0.09	1.512	0.052	1.460
0.10	3.697	0.271	3.426

Table 4.2: Ionization and Recombination Rates Along the Centerline: Baseline Case

Power Density ($10^8 W/m^3$)					
x(m)	Ohmic Dissipation	Collisional Transfer	Ionization	Transverse Heat Conduction	Axial Heat Conduction
0.00	5.19	-0.03	-4.36	0.014	-1.350
0.01	2.31	-0.32	-1.58	-0.057	-0.003
0.02	1.40	-0.47	-1.12	-0.037	-0.002
0.03	1.07	-0.38	-0.77	0.001	0.004
0.04	1.00	-0.30	-0.68	0.005	0.002
0.05	1.10	-0.30	-0.84	0.013	0.004
0.06	1.35	-0.28	-1.10	0.013	0.004
0.07	1.85	-0.28	-1.50	0.015	0.005
0.08	2.91	-0.30	-2.35	0.018	0.008
0.09	5.07	-0.36	-3.96	0.051	-0.016
0.10	9.37	-0.20	-10.04	0.161	-0.101

Table 4.3: Magnitude of Some Terms in the Electron Energy Equation: Centerline

the wall boundaries represent a loss of energy from the flow. Given the transverse distributions of gas temperature and electron density, these losses can be estimated. The flux of energy to the walls due to conduction is shown in Figure 4.32, and due to ambipolar diffusion in Figure 4.33. For the baseline case of this research the total power input was 298kW, not including power lost in the near-electrode drops and assuming a channel depth of 0.4m. The depth was chosen to approximate the thruster studied experimentally by Heimerdinger[10]. Based on the calculated energy fluxes, an ambipolar power loss of 8.5% was obtained, as well as a 4.8% power loss due to transverse heat conduction. This amounts to a 13.2% total power loss, although in the real flow the prescence of large voltage drops in the near-electrode regions would account for a much greater loss of power. It is unclear how the incorporation of these voltage drops into the model would change the flow behavior near the electrodes.

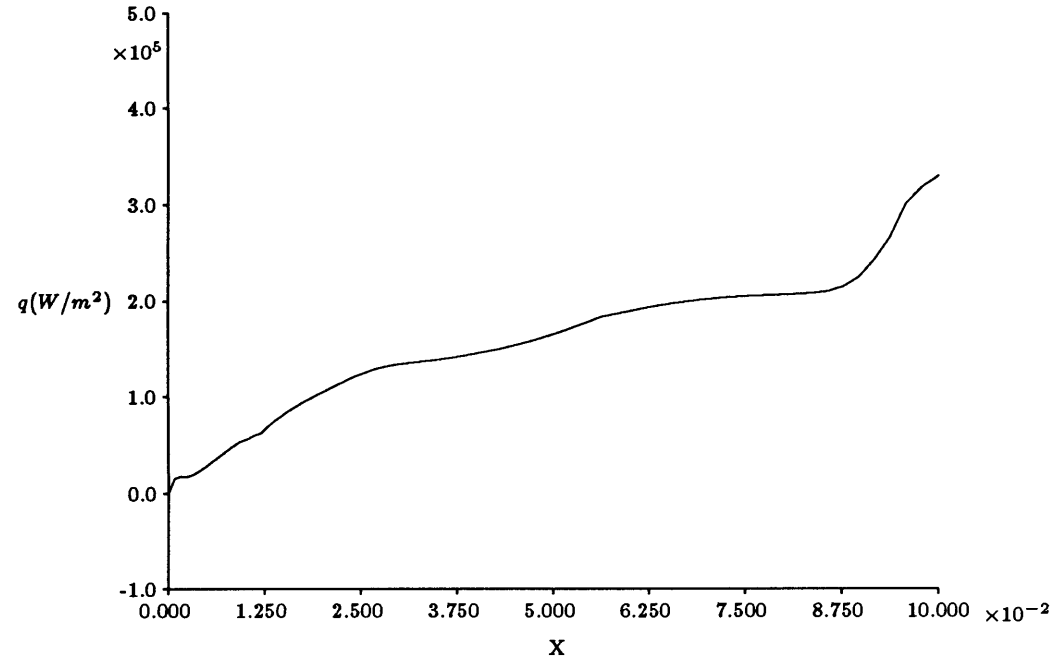

Figure 4.32: Energy Flux to One Electrode Surface Through Heat Conduction

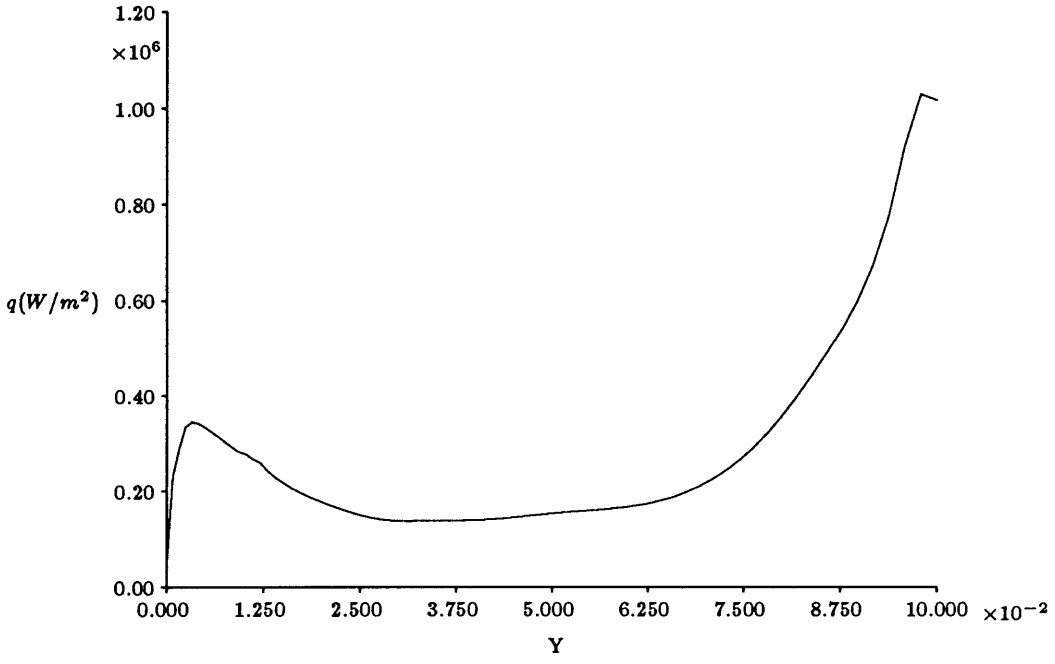

Figure 4.33: Energy Flux to One Electrode Surface Through Ambipolar Diffusion

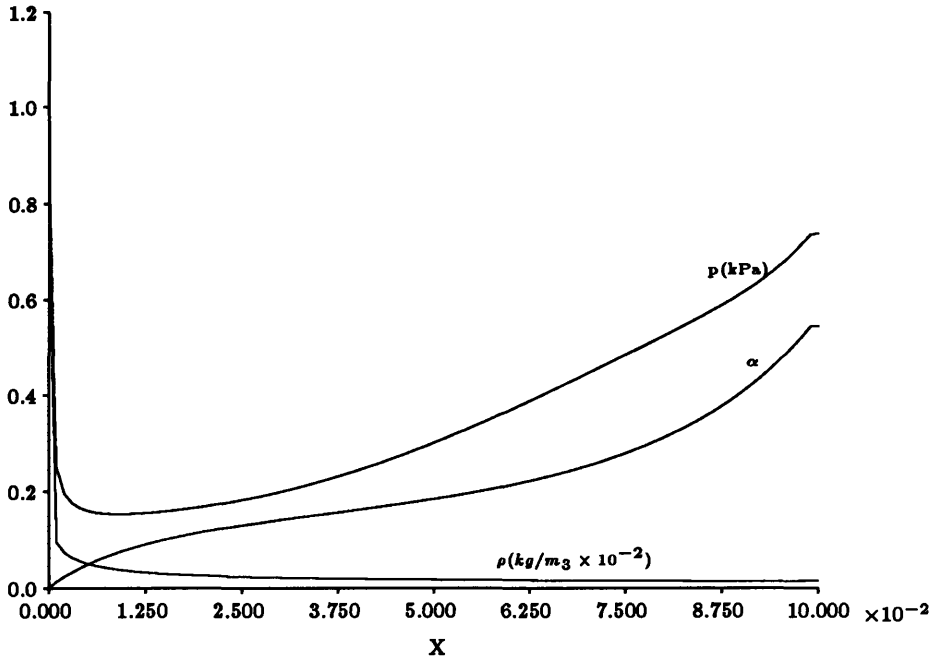

Figure 4.34: ρ, p, and α from Similar Quasi-1D Case

4.3 Comparison With Quasi-1D Results

The quasi one-dimensional code of Niewood[27] was used to calculate a solution for comparison to the two-dimensional baseline case of this research. Parameters for the quasi-1D run are identical to those utilized for the 2D case. The physical model used in the quasi-1D code is roughly the same as that used in this research, except that the only viscous and diffusive effects included are (1) $D_a \frac{\partial^2 n_a}{\partial y^2}$ ambipolar diffusion in the ion density and electron energy equations, (2) $\mu \frac{\partial^2 u}{\partial y^2}$ viscous shear in the axial overall momentum equation, and (3) $\mu \left(\frac{\partial u}{\partial y}\right)^2$ viscous dissipation in the heavy species energy equation. All three viscous and diffusive terms are calculated based on the assumption that the fluid velocity and electron density have parabolic distributions in the transverse direction. The density, pressure, and ionization fraction from the quasi-1D case are plotted in Figure 4.34, while the axial velocity, Mach number, heavy species temperature, and electron temperature are presented in Figure 4.35.

In general, the results from this two-dimensional model follow those of the quasi one-dimensional case fairly closely. Differences arise primarily from the non-parabolic

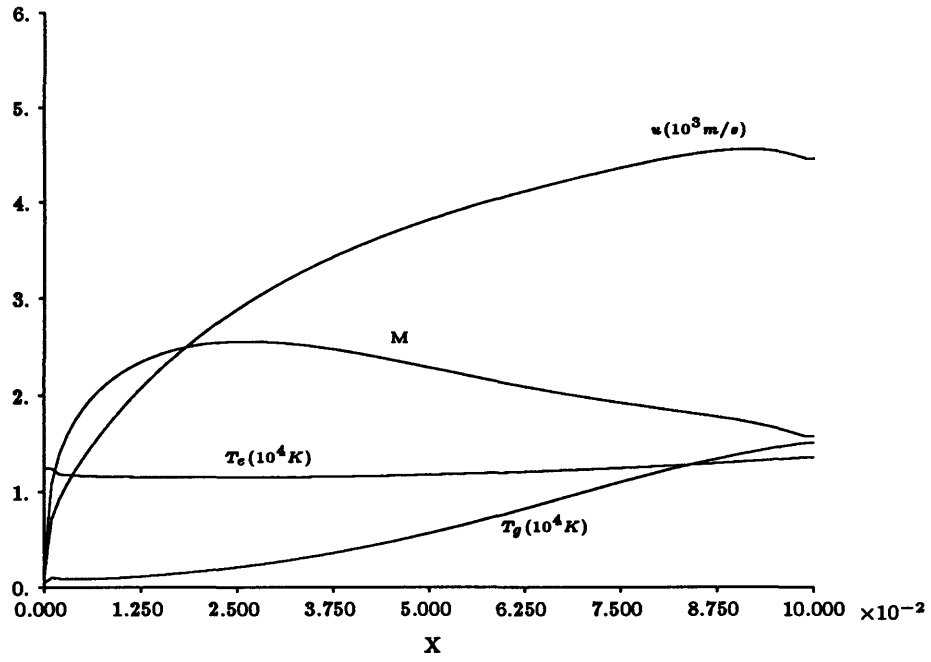

Figure 4.35: u, M, T_g, and T_e from Similar Quasi-1D Case

and non-constant transverse distributions of the flow variables found in this research, especially the velocity and density distributions, which directly impact the calculation of viscous and diffusive effects. It was shown by Niewood that the inclusion of viscosity and diffusion in the quasi-1D model substantially altered the flow solution for relatively narrow channels[27], so that any differences in the calculated magnitude of these effects could be expected to give very different results. A second cause of discrepancies between the models is the inaccuracy of the two-dimensional code near the entrance of the channel, due to problems with the inlet boundary conditions and numerical smoothing as discussed in section 4.1.1.

Figures 4.36 through 4.39 show four representative flow quantities averaged over the channel cross-section. Even with the difficulties of the 2D code at the inlet, the average ionization fraction (Fig. 4.36) is nearly the same as that of the quasi-1D case. The average electron temperatures calculated by each method are also similar, although the average gas temperatures differ considerably. This is most likely due to the non-parabolic transverse distributions and the low fixed wall temperature in the two-dimensional case, which prescribe different viscous dissipation and collisional heating rates from the simplified quasi one-dimensional case. The average flow velocity is plotted in Figure 4.39 for

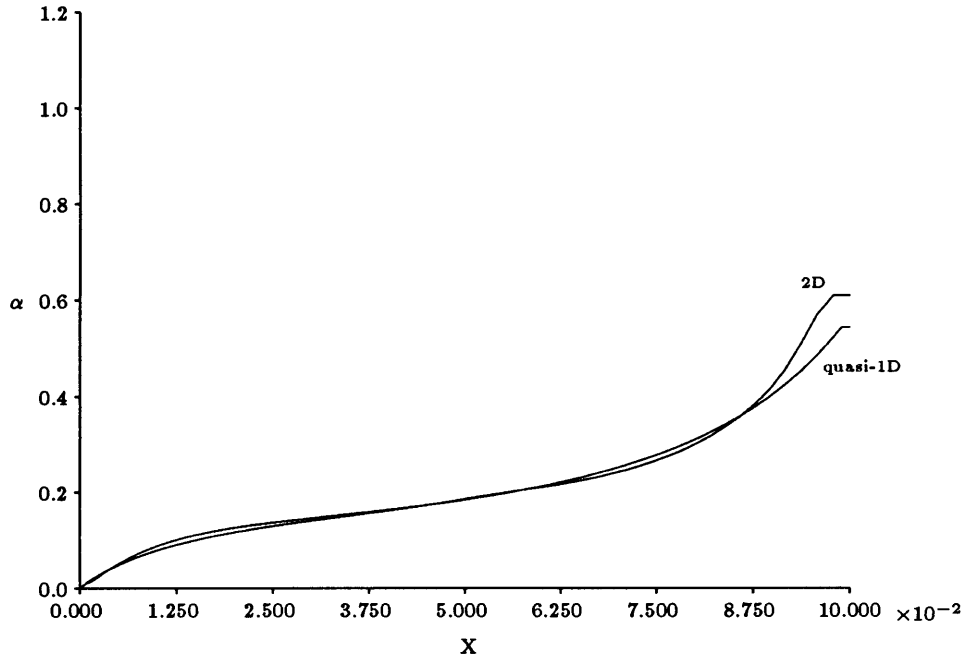

Figure 4.36: Comparison of Quasi-1D and 2D Results: Ionization Fraction

the two cases. Here it is observed that the 2D solution diverges rapidly from the quasi-1D solution, primarily due to the steeper adverse pressure gradient generated in the 2D case from differing transverse distributions and the influence of the wall density boundary conditions. Further refinement of the two-dimensional scheme is necessary, however, before conclusive comparisons with the quasi one-dimensional code can be made.

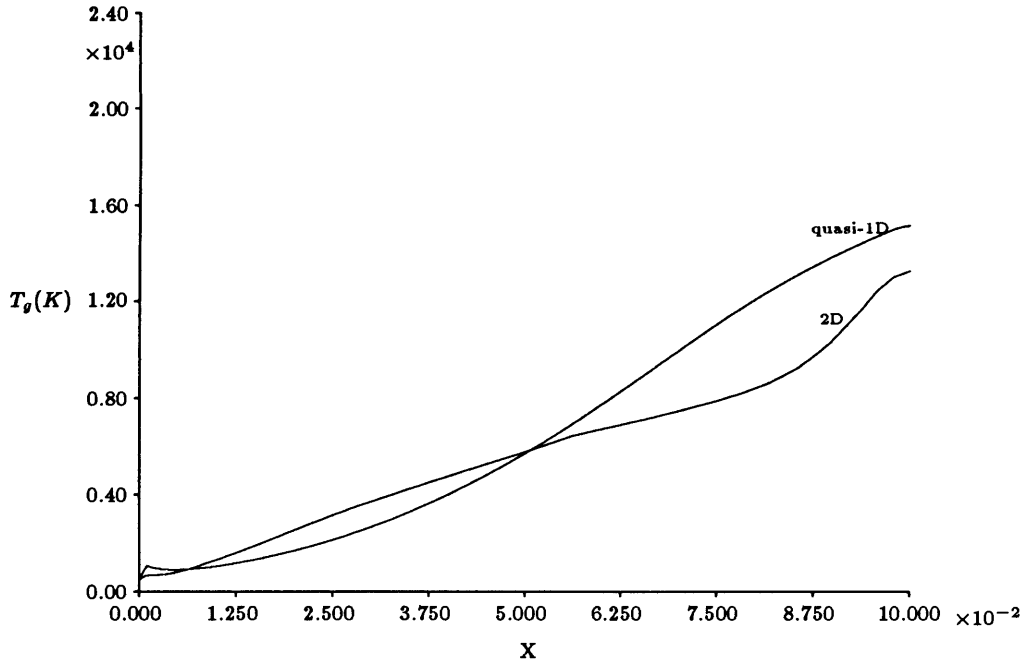

Figure 4.37: Comparison of Quasi-1D and 2D Results: Gas Temperature

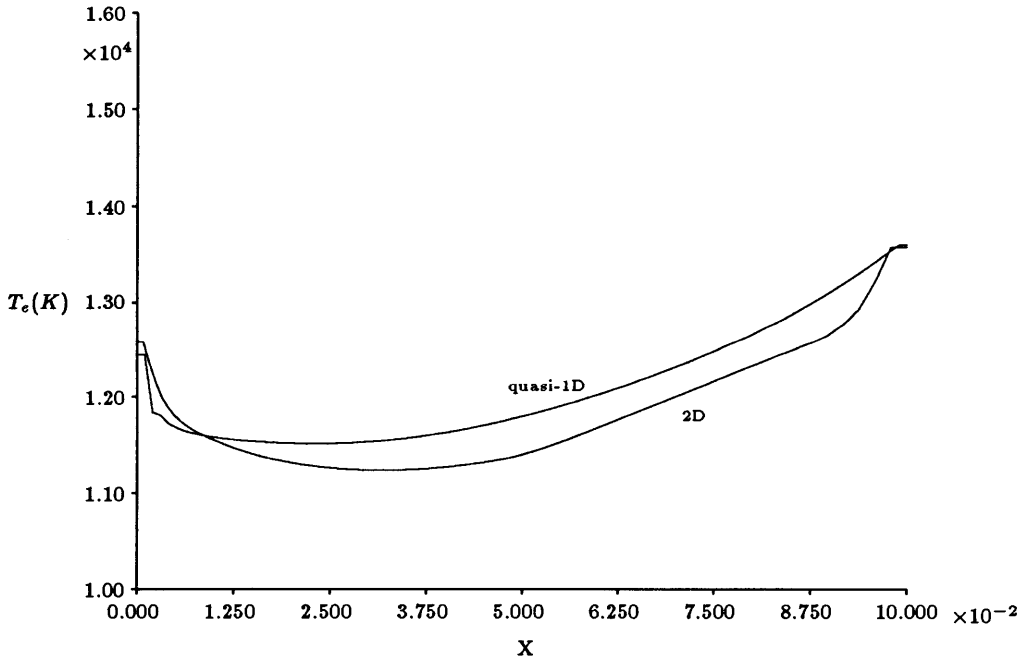

Figure 4.38: Comparison of Quasi-1D and 2D Results: Electron Temperature

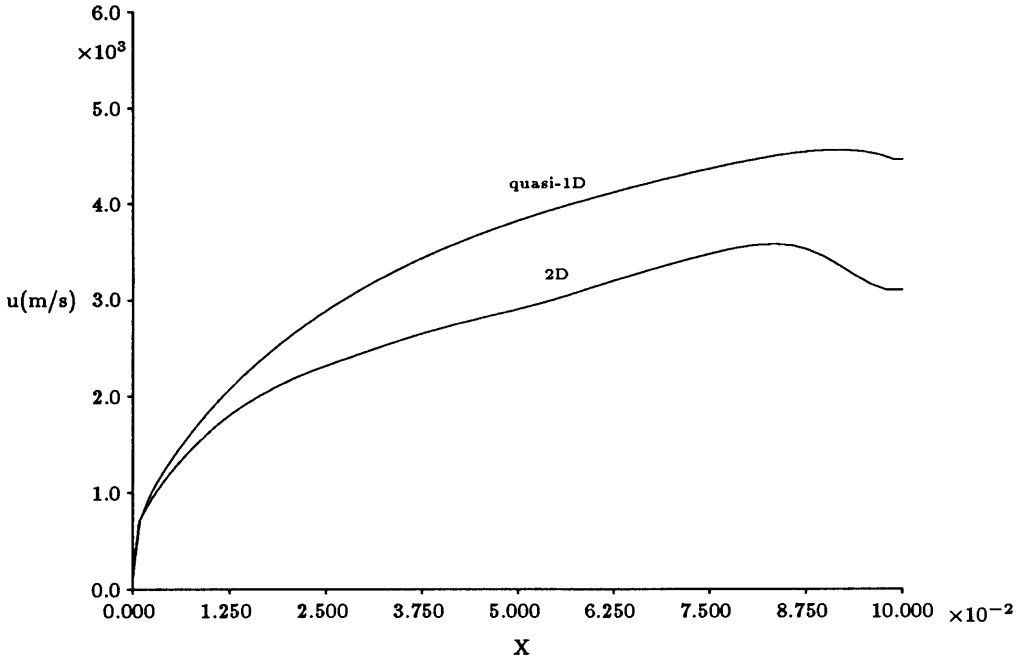

Figure 4.39: Comparison of Quasi-1D and 2D Results: Flow Velocity

Chapter 5
Conclusions

This research has developed a two-dimensional numerical model for the calculation of magnetoplasmadynamic flows in a constant area channel. The model distinguishes between electrons and heavy species, and employs MacCormack's Time-Split Method to integrate the governing equations. Viscous and diffusive processes are incorporated using essentially a Navier-Stokes formulation; these include ambipolar diffusion, viscous shear, viscous dissipation, and electron and heavy species heat conduction. Other effects such as nonequilibrium ionization, Lorentz acceleration, Ohmic heating, and collisional energy transfer are also included.

The flow calculated in the baseline case was similar to that seen in previous one-dimensional calculations. A rapid decrease in density and pressure at the inlet caused the gas to become supersonic in the first grid cell, after which the Mach number remained fairly constant. The velocity boundary layers originating at the inlet electrodes merged at the centerline by half the channel length, although the fully developed velocity profile was not parabolic. Viscous dissipation and collisional energy transfer from the electrons increased the gas temperature to a level greater than the electron temperature by the channel exit, a phenomenon which has been observed in experiments. Viscous heating created transverse maxima in the gas temperature, located at a distance approximately 10% of the channel width inside the electrode walls.

Other flow quantities also displayed two-dimensional structure. The formation of steep density gradients near the walls was caused by transverse gas temperature gradients and the ambipolar diffusion of electrons, as ions which were carried with the electrons could not pass through the wall boundaries and thus accumulated there. In addition, a much higher ionization rate was required near the walls to compensate for the loss of these electrons. The transverse distributions of electron number density and electron temperature were such that the Ohmic dissipation was nearly constant over the channel cross-section.

The transverse structure revealed in this research demonstrates the necessity of two-dimensional MPD thruster models to capture not only multidimensional electromagnetic effects such as the Hall Effect, but also transverse flow variations created by viscous and diffusive processes. These transverse distributions were seen to be fairly complex, and not easily modeled by such simple assumptions as parabolic flow in the case of velocity. Viscous and diffusive effects also produced an axial flow solution which was significantly different from those seen in previous one-dimensional, inviscid models. Examples of this include excessive heating of the heavy species through viscous dissipation, and a reduction in the axial velocity through viscous shear and the establishment of a strong adverse pressure gradient. Further work on this model is warranted, however, to quantify these effects and to determine the extent to which the interaction of a self-consistent magnetic field would influence the flow solution.

Chapter 6
Recommendations for Further Work

Further work on the model constructed in this research is warranted in order to better quantify the effect of viscous and diffusive processes, and to formulate a self-consistent magnetic field calculation so that fully two-dimensional flow can be predicted. In the near future the problematic inlet boundary conditions must be improved. This may involve developing a modified characteristic theory which includes the effects of the current and magnetic field. It may be sufficient to formulate a new numerical smoothing technique based on the overall pressure instead of that of the individual species. The next step would be to add a dynamic magnetic field calculation to obtain a self-consistent flow solution. This could be compared to the static magnetic field case to determine the effects of axial current and other nonuniformities. Calculating the magnetic field as a flow variable would also allow the $B = 0$ boundary condition at the exit to be relaxed, most likely by extending the computational domain beyond the end of the electrodes and allowing current to flow through that region.

Later work on this model could involve modification of the electrode wall boundary conditions to include a rigorous model of the plasma sheaths located there, and to account for the voltage drops at the anode and cathode. It may also be important to change the formulation of the equations to an axisymmetric coordinate system, since most experimental MPD thrusters are coaxial in geometry. Finally, a non-Cartesian grid would be required to examine the effects of channel contouring on thruster performance. In general a great deal of research needs to be performed both numerically and experimentally in order for magnetoplasmadynamic flows to be fully understood and applied.

Bibliography

[1] D.A. Anderson, J.C. Tannehill, and R.H. Pletcher, *Computational Fluid Mechanics and Heat Transfer*, Hemisphere Publishing Corp., New York, 1984

[2] M. Auweter-Kurtz, H.L. Kurtz, H.O. Schrade, and P.C. Sleziona, "Numerical Modeling of the Flow Discharge in MPD Thrusters", Journal of Propulsion and Power, Vol.5, No.1, Jan.-Feb. 1989

[3] D.R. Bates, A.E. Kingston, and R.W.P. McWhirter, "Recombination Processes Between Electrons and Atomic Ions", Proc. Royal Society A, Vol.267; Vol.270, 1962

[4] J.A. Bittencourt, *Fundamentals of Plasma Physics*, Pergamon Press, New York, 1986

[5] J.M.G. Chanty and M. Martinez-Sanchez, "Two-Dimensional Numerical Simulation of MPD Flows", AIAA-87-1090, AIAA/DGLR/JSASS 19th International Electric Propulsion Conference, Colorado Springs, May 1987

[6] M.S. DiCapua and R.G. Jahn, "Energy Deposition in Parallel Plate Plasma Accelerators", AIAA 71-197, AIAA 9th Aerospace Sciences Meeting, New York, January 1971

[7] J.H. Gilland, A.J. Kelly, and R.G. Jahn, "MPD Thruster Scaling", AIAA 87-0997, AIAA/DGLR/JSASS 19th International Electric Propulsion Conference, Colorado Springs, May 1987

[8] D.J. Heimerdinger, "An Approximate Two-Dimensional Analysis of an MPD Thruster", S.M. Thesis, Massachusetts Institute of Technology, June 1984

[9] D.J. Heimerdinger, "Fluid Mechanics in a Magnetoplasmadynamic Thruster", Doctoral Thesis, Massachusetts Institute of Technology, Jan. 1988

[10] D.J. Heimerdinger, D.B. Kilfoyle, and M. Martinez-Sanchez, "Experimental Characterization of Contoured Magnetoplasmadynamic Thrusters", AIAA 88-3205, AIAA/ASME/SAE/ASEE 24th Joint Propulsion Conference, Boston, July 1988

[11] E. Hinnov and J.G. Hirshberg, "Electron-Ion Recombination in Dense Plasmas", Physical Review, Vol.125, No.3

[12] M.Y. Jaffrin, "Shock Structure in a Partially Ionized Gas", The Physics of Fluids, Vol.8, No.4, April 1965

[13] D.B. Kilfoyle, M. Martinez-Sanchez, D.J. Heimerdinger, and E.J. Sheppard, "Spectroscopic Investigation of the Exit Plane of an MPD Thruster", DGLR/AIAA/JSASS 20th International Electric Propulsion Conference, Garmisch-Partenkirchen, W. Germany, October 1988

[14] D.Q. King and J.C. Sercel, "A Review of the Multimegawatt MPD Thruster and Current Mission Applications", AIAA 86-1437, AIAA/ASME/SAE/ASEE 22nd Joint Propulsion Conference, Huntsville, June 1986

[15] D.Q. King and J.R. Brophy, "Design and Operation of a 100 kW, Subscale MPD Engine", AIAA 87-1020, AIAA/DGLR/JSASS 19th International Electric Propulsion Conference, Colorado Springs, May 1987

[16] Y. Kunii and K. Kuriki, "Multipole MPD Arcjet", AIAA 85-2055, AIAA/DGLR/JSASS 18th International Electric Propulsion Conference, Alexandria, Oct. 1985

[17] K. Kuriki, K. Uematsu, and S. Morimoto, "MPD Arcjet Performance with Various Propellants", AIAA 82-1885, AIAA/JSASS/DGLR 16th International Electric Propulsion Conference, New Orleans, Nov. 1982

[18] J.L. Lawless and V.V. Subramanian, "A Theory of Onset in MPD Thrusters", AIAA 85-2039, AIAA/DGLR/JSASS 18th International Electric Propulsion Conference, Alexandria, Oct. 1985

[19] M.A. Lieberman and A.L. Velikovich, *Physics of Shock Waves in Gases and Plasmas*, Springer-Verlag, New York, 1986

[20] R.W. MacCormack, "The Effect of Viscosity in Hypervelocity Impact Cratering", AIAA 69-354, 1969

[21] R.W. MacCormack, "Numerical Solution of the Interaction of a Shock Wave with a Laminar Boundary Layer", *Lecture Notes in Physics*, Vol.8, Springer-Verlag, 1971

[22] R.W. MacCormack and B.S. Baldwin, "A Numerical Method for Solving the Navier-Stokes Equations with Application to Shock-Boundary Layer Interactions", AIAA 75-1, AIAA 13th Aerospace Sciences Meeting, Pasadena, Jan. 1975

[23] M. Martinez-Sanchez and D.J. Heimerdinger, "Two-Dimensional Analysis of an MPD Arcjet", AIAA 85-2050, AIAA/DGLR/JSASS 18th International Electric Propulsion Conference, Alexandria, Oct. 1985

[24] M. Martinez-Sanchez, "The Structure of Self-Field Accelerated Plasma Flows", AIAA 87-1065, AIAA/DGLR/JSASS 19th International Electric Propulsion Conference, Colorado Springs, May 1987

[25] M. Mitchner and C. Kruger, *Partially Ionized Gases*, John Wiley and Sons, New York, 1973

[26] R.M. Myers, N. Suzuki, A.J. Kelly, and R.G. Jahn, "Cathode Phenomena in a Low Power, Steady State MPD Thruster", AIAA 88-3206, AIAA/ASME/SAE/ASEE 24th Joint Propulsion Conference, Boston, July 1988

[27] E.H. Niewood, "Transient One Dimensional Numerical Simulation of Magnetoplasmadynamic Thrusters", S.M. Thesis, Massachusetts Institute of Technology, Feb. 1989

[28] L.E. Olson, P.R. McGowan, and R.W. MacCormack, "Numerical Solution of the Time-Dependent Compressible Navier-Stokes Equations in Inlet Regions", NASA TM X-62338, March 1974

[29] W. Park and D. Choi, "Two-Dimensional Model of the Plasma Thruster", Journal of Propulsion and Power, Vol.4, No.2, Mar.-Apr. 1988

[30] P.J. Roache, *Computational Fluid Dynamics*, Hermosa Publishers, Albuquerque, 1985

[31] L.K. Rudolph and K.M. Hamlyn, "A Comparison Between Advanced Chemical and MPD Propulsion for Geocentric Missions", AIAA 83-1391, AIAA/SAE/ASME 19th Joint Propulsion Conference, Seattle, June 1983

[32] L.K. Rudolph and D.Q. King, "Electromagnetic Thrusters for Spacecraft Prime Propulsion", AIAA 84-1446, AIAA/SAE/ASME 20th Joint Propulsion Conference, Cincinnati, June 1984

[33] H. Schlichting, *Boundary-Layer Theory*, 7th ed., McGraw-Hill, New York, 1979

[34] E.J. Sheppard and M. Martinez-Sanchez, "Ionization Nonequilibrium in Plasma Accelerators", AIAA 90-2608, AIAA/DGLR/JSASS 21st International Electric Propulsion Conference, Orlando, July 1990

[35] L. Spitzer and R. Härm, "Transport Phenomena in a Completely Ionized Gas", Physical Review, Vol. 89, 1953

[36] V.V. Subramanian and J.L. Lawless, "Onset in Magnetoplasmadynamic Thrusters with Finite-Rate Ionization", Journal of Propulsion and Power, Vol.4, No.6, Nov.-Dec. 1988

[37] K. Toki, "Quasisteady MPD Arcjet with Hollow Cathode", AIAA 85-2057, AIAA/DGLR/JSASS 18th International Electric Propulsion Conference, Alexandria, Oct. 1985

[38] W.G. Vincenti and C.H. Kruger, *Introduction to Physical Gas Dynamics*, Wiley, New York, 1965

[39] F.M. White, *Viscous Fluid Flow*, McGraw-Hill, New York, 1974

[40] T. Yoshikawa, Y. Kagaya, and K. Kuriki, "Thrust and Efficiency of the K-III MPD Thruster", Journal of Spacecraft and Rockets, Vol. 21, Sept.-Oct. 1984

Appendix A
Fundamental Constants

Electric charge of a proton	$e = 1.602 \times 10^{-19} C$
Permittivity of vacuum	$\epsilon_0 = 8.854 \times 10^{-12} \frac{F}{m}$
Permeability of vacuum	$\mu_0 = 4\pi \times 10^{-7} \frac{H}{m}$
Planck's constant	$h = 6.626 \times 10^{-34} J - s$
Boltzmann's constant	$k = 1.381 \times 10^{-23} \frac{J}{^oK}$
Electron rest mass	$m_e = 9.11 \times 10^{-31} kg$
Argon atomic mass	$m_a = 6.634 \times 10^{-26} kg$
1st ionization energy for Argon	$E_i = 2.53 \times 10^{-18} J$
Ratio of specific heats for Argon	$\gamma = 1.667$
Argon gas constant	$R_g = 208.13 \frac{J}{kg^oK}$
Electron gas constant	$R_e = 1.516 \times 10^7 \frac{J}{kg^oK}$